Spring 2021

Experimental Investigation of Single and Two-Phase Heat Transfer Performance in Microchannels with Surface Modifications and Multiple Inlet Restrictors

Saad Kadham Oudah

Experimental Investigation of Single and Two-Phase Heat Transfer Performance in Microchannels with Surface Modifications and Multiple Inlet Restrictors

By

Saad Kadham Oudah

Bachelor of Science
al Mustansiriya University, 2002

Master of Science
al Mustansiriya University, 2004

Master of Science
University of South Carolina, 2018

Submitted in Partial Fulfillment of the Requirements

For the Degree of Doctor of Philosophy in

Mechanical Engineering

College of Engineering and Computing

University of South Carolina

2021

Accepted by:

Jamil A. Khan, Major Professor

Chen Li, Committee Member

Tanvir I. Farouk, Committee Member

Guiren Wang, Committee Member

Jasim Imran, Committee Member

Tracey L. Weldon, Interim Vice Provost and Dean of the Graduate School

DEDICATION

This dissertation is dedicated to my mom, dad, brothers, and sisters for encouraging and supporting me with continuous guidance throughout many years of my education and training. Special dedication to my wife Basma and my daughter Janna, for inspiring me to achieve greatness and support during this journey.

ACKNOWLEDGMENTS

I wish to deeply express my sincere gratitude to my advisor, Dr. Jamil Khan, Professor and Chair of Mechanical Engineering at University of South Carolina, for allowing me to work with him on this research subject. I am grateful for his leadership, inspiration, encouragement, and for sharing his wisdom and guidance throughout all phases of my Master's and PhD studies. I am especially grateful to my dissertation committee members—Dr. Chen Li, Dr. Tanvir I. Farouk, Dr. Guiren Wang, and Dr. Jasim Imran—for their comments.

Special thanks to Dr. Chen Li for providing the sandblasting, allowing use of facilities, and to his group for their help. I also wish to give a special thanks to Dr. Karim Egab for his contributions and assistance with microchannel sandblasting.

My special appreciation goes to Dr. Ruixian Fang for his invaluable suggestions, comments, continual guidance, and constant support during this journey. Working with Dr. Fang was a pleasure.

I would like to express my deepest thankfulness to my family. Thank you to my parents, brothers, and sisters, who always encourage and support me with their love. I am especially grateful to my wife, Basma Abed, who has been extremely supportive throughout this entire process and made countless sacrifices to help me earn these two degrees. To my daughter Janna: you are an inspiration to achieve greatness. Additionally, I would like to thank my mother-in-law, brother, and sister for their support. I have special thanks to Naeem Alibrahimi for encouraging and supporting.

I would like to thank my colleagues in the Enhanced Heat Transfer Lab—Dr. Azzam Salman, Dr. Noble Anumbe, Dr. Nabeel M. Abdulrazzaq, Mr. Ahmed Musafi Abir, and Mrs. Sowmya Raghu—for their invaluable suggestions, help, support, and friendship. A special thanks to Mr. Amitav Tikadar for his contributions and help. Additionally, I wish to thank the many members of the Mechanical Engineering Department and staff who helped and supported me through this journey; many thanks to the program administrators (Renee Jenkins, Misty O'Donnell, and Lalitha Ravi) for their assistance and kindness and to all the great professors and colleagues for their help and cooperation. Special thanks go to Mr. Bill Bradley for giving me the opportunity and training to work on the CNC machine.

I would like to thank my friends, Dr. Ahmed Saaudi and Dr. Hayder Almukhtar, for their companionship and encouragement. Thank to Dr. Abbas Kadhim for his encouragement at the beginning of this journey. Thanks to all Iraqi students at the University of South Carolina for their help and encouragement as well. Thank you to my sponsor (Ministry of Higher Education and Scientific Research in Iraq, MOHESR) for continued support.

Finally, I want to send my heartfelt thanks to Mrs. Pat Cannon for her help and support. I cannot thank her enough for everything that she has done for my life, standing with me and taking care of my wife and daughter. I thank Mrs. Cannon for her support, encouragement, prayers, and invaluable mentoring.

ABSTRACT

Due to shrinking component sizes and faster switching speeds, the volumetric heat generation rates and surface heat flux in many advanced power electronic devices have increased exponentially, creating an urgent need for efficient cooling technologies. It has become particularly challenging to maintain an optimal temperature at the device level. Among advanced cooling techniques, single-phase and two-phase microchannel heat sinks show considerable promise in removing a significant amount of heat from a small surface area. Considered one of the most efficient heat dissipaters, the two-phase microchannel heat sink can handle very high heat flux at a small footprint and requires relatively low coolant flow rates. However, ever-increasing high-heat-flux cooling requirements have pushed the single-phase microchannels to their limit. Therefore, further enhancement of the Heat Transfer Coefficient (HTC) in microchannel is needed. Although two-phase microchannels provide higher heat transfer rates, they suffer from flow instability issues, which cause significant oscillations in the flow rate, temperature, and pressure, as well as deterioration of the HTC and an early occurrence of Critical Heat Flux (CHF).

The objectives of this research were to: (1) enhance the performance of the single-phase microchannel heat transfer, and (2) suppress the two-phase microchannel flow instabilities to increase CHF. The surface modification techniques knurling and sandblasting, two methods which are conventionally used in macro duct flow systems, were experimentally investigated for the first time to improve the single-phase microchannel heat transfer performance.

A micro-knurled surface technology was found to be an effective approach for improving the single-phase microchannel heat transfer performance, resulting in a maximum HTC enhancement of 255% compared to that of the smooth microchannel. In contrast, fully sandblasting the bottom surface of the microchannel only slightly improved the heat transfer performance; however, modifying the surface with a hybrid micro-sandblasting of elliptical patterns enhanced the heat transfer performance substantially.

Experimental studies were carried out to find the effects of various configurations of the Inlet Restrictors (IRs) on the thermal/hydraulic performance of flow boiling in a single rectangular microchannel with an aspect ratio of 13.12 and a hydraulic diameter of 708 μm. The following three designs were investigated at mass fluxes of 32.68, 81.29, and 144 kg/m^{2}s: one-slot opening (1IR), three-slot openings (3IR), and five-slot openings (5IR). All the test cases with IRs improved the CHF performance of the flow boiling microchannel heat sink, where the 5IR case performed best at low mass flux, and the 1IR case worked best at high mass flux. In addition, the IRs reduced the HTC at low mass flux but improved the HTC at high mass flux and heat flux. As expected, IRs always exhibited higher pressure drop penalties. A key finding of this study is the optimal design criteria for a microchannel with IRs, which depends on the operational parameters (e.g., mass flux and heat flux) of the two-phase microchannel heat sink. Furthermore, a parametric study of the effects of the area ratio of the IR with an opening of 4.2%, 6.58%, 8.57%, 9.32%, 12.86%, and 15.5% on two-phase microchannel heat transfer was also performed. The results suggest an optimal area ratio in the range between 8% -10% for all ranges of mass flux between mass flux G = 66 kg/m^{2}s to 221.65 kg/m^{2}s. The proposed range results from the uncertainties of the IR dimensions.

A knurled surface was also used to study its effects on the thermal performance in flow boiling microchannels. A diamond-patterned knurling was fabricated on the bottom surface of the microchannel, with two different knurling heights R-1 (0.25 mm) and R-2 (0.17 mm). The CHF for both the R-1 and R-2 cases were all improved, at mass flux G = 66.48 kg/m^{2}s and 172.87 kg/m^{2}s, respectively. Specifically, at mass flux G = 172.87 kg/m^{2}s, the improvements of the CHF for the roughened surfaces were around 30% higher than the CHF for the smooth surface under similar conditions tested. In addition, the results show that the knurling does not significantly influence the pressure drop. Moreover, the optimal design of the IRs was achieved when combined with knurling to further enhance the heat transfer performance of the two-phase microchannels. The hybrid design decreased the amplitudes of the pressure-drop oscillations up to 60%.

TABLE OF CONTENTS

LIST OF TABLES

LIST OF FIGURES

LIST OF SYMBOLS

A_{ch}	microchannel cross section area(m^2)
A	heating surface area (m^2)
CHF	critical heat flux (W/cm^2)
C_p	heat capacity (J/kg k)
D_h	hydraulic diameter (mm)
f	friction factor across microchannel
G	mass flux (kg/m^2 s)
HTC	heat transfer coefficient
h_{avg}	average heat transfer coefficient (W/m^2 k)
h_{sp}	heat transfer coefficient for the single-phase region (W/m^2 k)
h_{tp}	heat transfer coefficient for the two-phase region (W/m^2 k)
h_{fg}	latent heat (kJ/kg)
I	current (amp)
k	thermal conductivity (W/m k)
L	length of microchannel (mm)
L_{sub}	upstream single-phase region (mm)
L_{sub}	downstream saturated two-phase region (mm)
Nu	average Nusselt number
$\dot{m}$	mass flow rate (kg/s)
M	dimensionless parameter in Eq. (32)
P	pressure (Pa)
Δp_{exp}	measured pressure drop (Pa)

$\Delta p_{c1}, \Delta p_{c2}$ contraction pressure losses

$\Delta p_{e1}, \Delta p_{e2}$ expansion pressure losses

Δp pressure drop across the microchannel(pa)

$\Delta p_{mea.}$ measured pressure drop (Pa)

$\Delta p_{c1}, \Delta p_{c2}$ contraction pressure losses

$\Delta p_{e1}, \Delta p_{e2}$ expansion pressure losses

Q input power (Watt)

$q^{"}$ heat flux (W/cm^2)

q_r CHF ratio

R_e Reynolds number

T_s surface temperature (°C)

T_{in} inlet temperature (°C)

T_{sat} saturated temperature (°C)

V voltage (Volt)

W width of channel (m)

x_e two-phase quality

Greek Symbols

$\Delta x'$ distance between the first row of thermocouples and the top surface (mm)

Δx distance between two rows of thermocouples (mm)

Subscripts

CHF critical heat flux

Ch channel

Cu copper

eff effective

e exit

IR inlet restrictor

i	number
loss	heat loss
r	ratio
sat	saturation
sub	subcooled
sp	single-phase
tp	two-phase

CHAPTER 1

INTRODUCTION AND MOTIVATION

1.1 Motivation

Electronic device manufacturers strive to increase both the processor capacity and its speed efficiently. However, increasing the capacity and speed of a processor exponentially increases the amount of heat generated in that processor. In addition, compacting electronic devices reduces the heat transfer contact surface area, which increases the heat density. In order to increase the processor capacity, advanced cooling technologies are needed to prevent overheating and ultimately failure of the electronic components. Therefore, thermal management is essential in many electronic systems in order to maintain as low an isothermal surface temperature as possible. An abundance of cooling techniques, such as air cooling, have been introduced for thermal management to replace the traditional cooling systems. Each system maintained efficient working of the devices and kept them within the range of safe operating temperatures. Due to the high-power density, keeping systems cool at the device level is a very challenging problem. Therefore, several cooling techniques are used to solve this issue. Among them, single-phase and two-phase flow boiling in microchannels have shown considerable promise as a technique for removing a large amount of heat from a small area. Flow boiling is considered one of the most efficient and reliable heat dissipaters as it can decrease heat flux on a small footprint and needs much lower coolant flow rates compared to conventional heat sinks.

However, the thermal performance of flow boiling microchannel suffers from flow instability issues, which may potentially cause the heat sink to overheat and reach the critical heat flux (CHF) early. CHF is defined as the maximum heat that can be transferred by a flow boiling from a target surface.

In this work, the research objectives are to: (i) passively enhance the microchannel heat transfer performance in a single-phase regime; and (ii) use a passive solution to reduce and/or suppress flow instabilities and increase the CHF in two-phase microchannel flow boiling.

1.2 **Microchannel Heat Sink**

Microchannels undergo heat transfer due to the large surface area to volume ratio and small footprints, which can increase its heat transfer coefficient (HTCs). Furthermore, compared with other cooling techniques, microchannels are considered a high-performance cooling technique. Instead of using air as the working fluid, liquids such as water and refrigerants are employed in microchannels for much higher cooling performance. The heat created by the electronic device is transferred first to the substrate of the microchannel through conduction, and then to the cooling liquid that moves through the small-scale channels. Microchannel heat sinks are classified into either single-phase or two-phase applications depending on the cooling liquid maintaining liquid state or undergoing flow boiling. In single-phase microchannel heat sinks, the cooling fluid does not undergo a phase change and maintains liquid state, where heat is absorbed by the working fluid in the form of sensible heat. Meanwhile, for the two-phase heat sink, the cooling fluid will undergo a liquid-vapor phase change inside the microchannels.

1.2.1 Single-Phase Flow Microchannel Heat Transfer

Tuckerman and Pease first introduced the concept of microchannels in 1981. They conducted experiments in a rectangular microchannel heat sink comprised of a silicon wafer with dimensions of 1 x 1 cm^2. The channel dimensions were 0.05 mm in width and 0.3 mm in depth, and the channels were separated with 0.05 mm thick walls. Using water as a cooling fluid, they found that their microchannel heat sink could dissipate heat flux up to 790 W/cm^2, with a maximum substrate temperature rise of 71℃. However, this heat transfer performance was achieved with a very high pressure drop of 31 psi [1]. Since, microchannels have drawn significant attention as a promising research topic in thermal engineering.

The use of microchannels in the single-phase serves to increase the convective HTCs and maintain the surface temperature of the heat sink within practical limits. From the work of Tuckerman and Pease [1], it is clear that either reducing the hydraulic diameter or increasing the flow rate leads to a high pressure drop [2]. For convective heat transfer in channels with a hydraulic diameter of D_h, the HTC (h) is calculated as shown in Eq (1),

$$h = \frac{k_f \, \mathrm{Nu}}{D_h} \tag{1}$$

where k_f is the fluid thermal conductivity, and Nu is the Nusselt number for the appropriate flow condition.

1.2.2 Two-Phase Flow Microchannel Heat Transfer

As mentioned for single-phase microchannel flow, a decrease in the hydraulic diameter leads to an increased pressure drop, and thus an increase in the pumping power

of the cooling system. The pumping power (P_{power}) of a microchannel can be calculated using Eq (2).

$$P_{power} = n\, U_{avg}.A_{ch}.\Delta p \quad (2)$$

where U_{avg} is the average channel flow velocity, Δp is pressure drop across the channel, n is number of channels in a heat sink, and A_{ch} is the cross-sectional area of each channel [3].

The HTC in the two-phase flow regime is much larger than that in the single-phase regime. A two-phase flow occurs when the surface temperature of the channel is greater than the saturated fluid temperature. Consequently, at the same mass flow rate, the amount of heat that can be removed from the surface via two-phase flow boiling is ten times that compared to single-phase flow. This significant advantage that two-phase flow has compared to its single-phase counterpart is due to the advantage of latent heat of the working fluid and the more rigorous evaporative heat transfer [4]. Moreover, during the phase change, the wall temperature is uniform because the phase change always occurs at a nearly constant temperature. For both single- and two-phase microchannel heat sinks, the heat removal capability is directly proportional to the coolant flow rates. Consequently, with a decrease in hydraulic diameter and/or increase in flow rate, the pressure drop across the microchannels increases significantly.

Two-phase microchannel heat sinks can have lower coolant flow rates to dissipate high heat flux. However, the hydrodynamic instabilities during two-phase heat transfer in microchannels may have an adverse effect on the safety of electronic devices being cooled. Several comprehensive review articles provide more details on microchannel heat transfer and fluid flow characteristics [5][6][7][8][9][10]. While flow boiling in microchannels has

become a promising heat transfer mechanism for cooling the next generation of high heat flux computer chips, it also faces many challenges, which this research aims to investigate.

1.3 Problem Statement

Due to continual miniaturization of microelectronic devices and faster switching speeds, the volumetric heat generation rates, as well as the surface heat flux, have increased exponentially. This has created a big dilemma in many engineering applications. Nowadays, the thrust to miniaturization microelectronic device has created an urgent need for efficient cooling technologies. Therefore, advanced cooling solutions are required to dissipate the large amount of heat produced in these power electronics effectively.

Figure 1.1 shows a summary of the system-cooling problem of a modern processor and a list of advanced cooling technologies that might meet the cooling requirements. As shown in Figure 1.1, the performance of the processor (e.g., CPU) is continuously improved with technology breakthroughs in both the hardware and software, and is expected to be further improved long-term [11]. The Moore's law predicted that the number of transistors on a microelectronic device doubles approximately every 24 months [12]. When combined with higher clocking rates of transistors and parallel processing, the heat flux produced requires an urgent need for efficient cooling technologies.

Generally, liquid cooling schemes are divided into two categories: direct and indirect cooling schemes. In the direct cooling techniques, the working fluid makes direct contact with the target surface. Typical examples include spray cooling [13]–[16], jet impingement [17], and pool boiling [18]. Alternatively, in indirect cooling techniques, the working fluid does not come into contact with the target surface. Examples include heat pipes, phase change materials, and microchannels [19][20]. Selecting a suitable cooling

methodology has become a major challenge for thermal engineers, as each cooling scheme has potential benefits and application limitations. However, microchannels have shown considerable promise as they remove of a large amount of heat from a small area.

1.4 **Research Purpose**

The main purpose of this research is to investigate two approaches to enhance the performance of both single- and two-phase microchannel heat sinks. The objective of the first approach is to passively enhance the microchannel heat transfer performance in a single-phase with micro-scale surface modification technologies. Specifically, two techniques, namely, knurling and sandblasting, were applied on the bottom surface of the microchannel heat sink to investigate their effect on thermal/hydraulic performance in the single-phase flow regime. The objective of the second approach is to use passive solutions to suppress the flow boiling instabilities and increase the CHF of the two-phase flow in microchannels. Specifically, two techniques have been investigated to mitigate flow boiling instability in this study. The first technique utilizes inlet restrictors (IRs) at the inlet of microchannels to suppress the flow boiling instability and increase the CHF. While the second technique combines IRs with the knurling surface modification technique to improve the heat transfer performance in the two-phase microchannels.

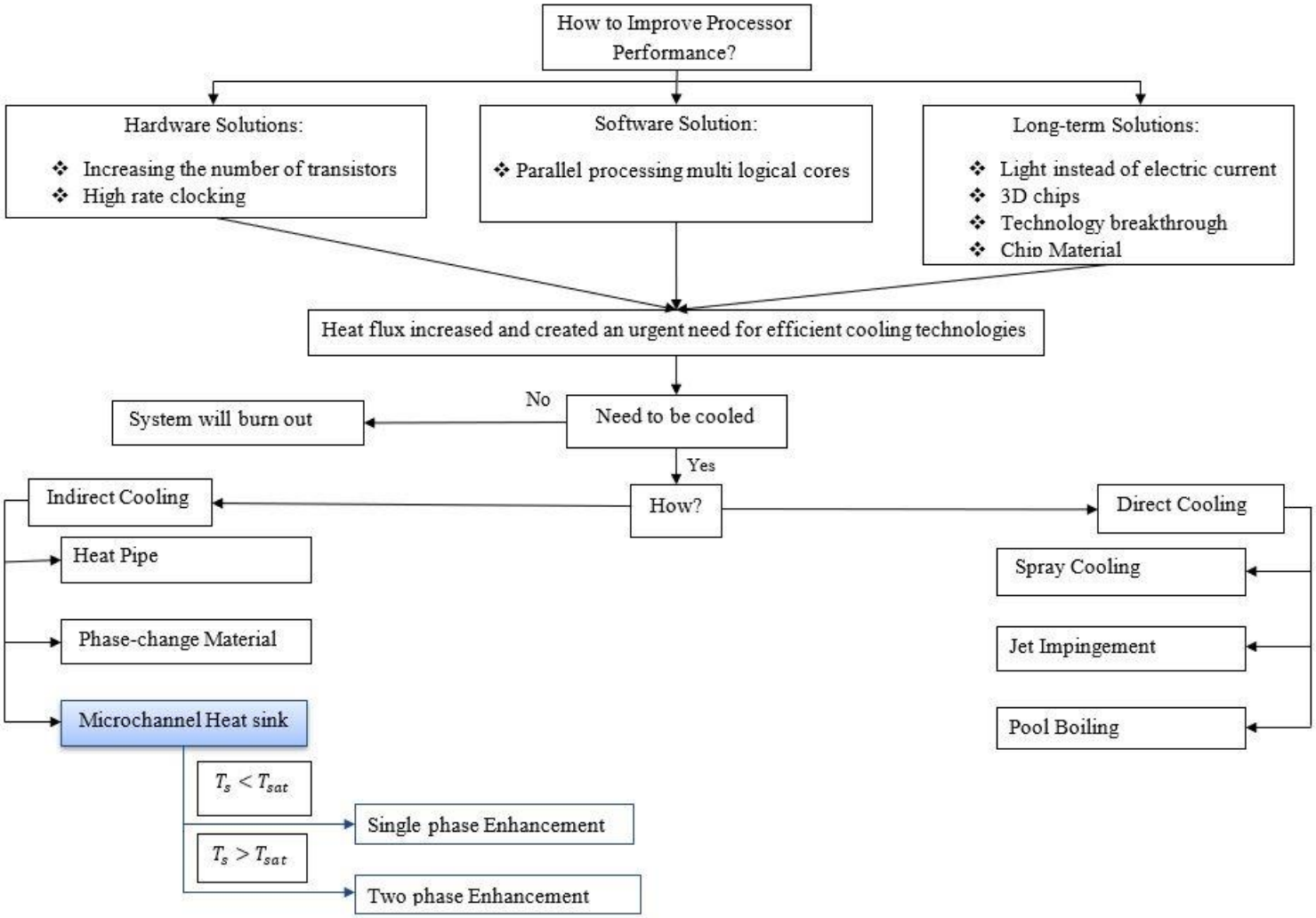

Figure 1.1 Overview of thermal issues in processors and cooling technologies.

1.5 **Research Objectives**

The specific objectives of this research are as follows:

(1) To perform an experimental study to test the effect of two surface modifications (knurling and sandblasting) towards enhancing heat transfer performance in single-phase flow regime. Specifically, investigating the effects of diamond-shaped knurling or sandblasting on the thermohydraulic performance of microchannels.

(2) To conduct an experimental study to explore the effects of diamond-shaped knurling on the heat transfer performance in flow boiling microchannels

(3) To experimentally explore the effect of multiple IRs on the suppression of flow boiling instabilities in microchannels.

(4) To study the effect of the IR (IR) area ratio on the CHF in two-phase microchannels and find the optimum design for a microchannel with IRs.

(5) To study the effect of a knurled surface on the thermal performance in flow boiling microchannels.

(6) To study the heat transfer performance of two-phase microchannels designed using the optimal combination of the IRs and knurling surface modification technique.

1.6 **Dissertation Layout**

In CHAPTER 2 literature reviews on heat transfer enhancement studies are presented for single-phase microchannel flow, flow boiling instabilities in two-phase microchannel flow and their stabilization techniques, and characteristics of IRs and their application on thermo fluidic control. CHAPTER 3 describes the experimental facility. CHAPTER 4 discusses the effect of diamond-shaped knurling and sandblasting on the heat transfer performance in single-phase microchannel heat sinks. CHAPTER 5 examines the

investigation of various configurations of IRs on the thermal/hydraulic performance of flow boiling in a rectangular microchannel, as well as the parametric study on the area ratio of the IR on two-phase microchannel heat transfer. CHAPTER 6, investigates the effects of diamond-shaped knurling surface on flow boiling in a microchannel heat sink. CHAPTER 7 presents the investigation of the heat transfer performance of the two-phase microchannels enhanced with a hybrid of the IRs and the knurling surface modification technique. Finally, the conclusion of this research is presented in CHAPTER 8, along with suggestions for future work.

CHAPTER 2

REVIEW OF PREVIOUS RESEARCH

This chapter reviews the fundamentals of microchannel heat sinks and heat transfer enhancement approaches in single-phase and two-phase flow regimes. In the single-phase regime, the continuous growth of the thermal and hydraulic boundary layers generates a high resistance inside the microchannel, and ultimately decreases the heat transfer performance and increases the pressure difference across the channel. This is one of the main constraints of using microchannels. Figure 2.1 depicts a schematic of the thermal boundary layer in a conventional microchannel.

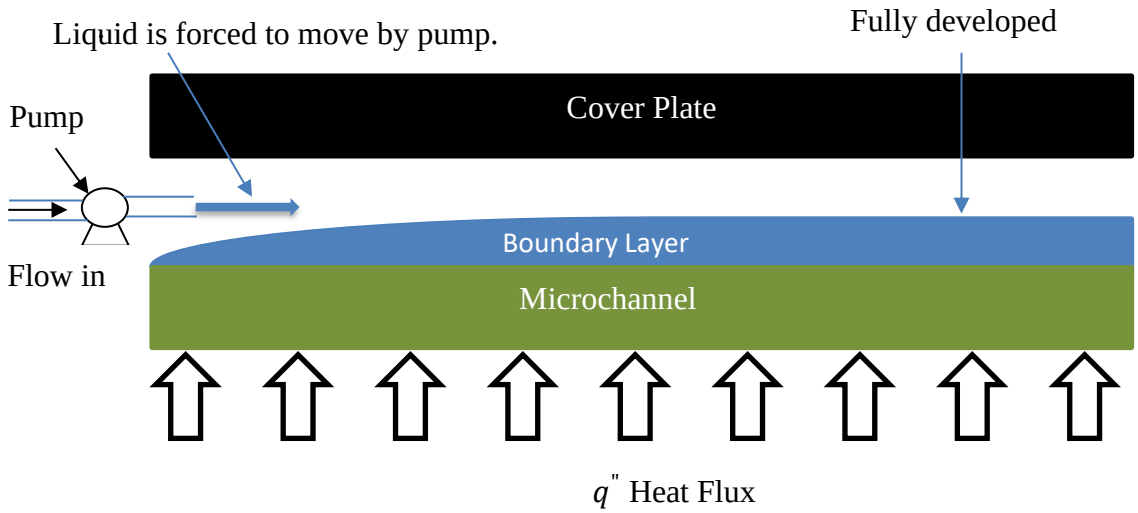

Figure 2.1 Fluid flow in the microchannel during single-phase flow.

Although the cooling performance of microchannel heat sinks is superior to that of conventional macro-channel heat sinks, it is still insufficient to meet the inherently growing cooling demand from high-heat-flux electronic devices. Further enhancement of thermal performance in microchannel heat sinks can be achieved by using both active and passive cooling approaches. In order to disrupt or break the thermal and hydraulic boundary layers in single-phase microchannels, researchers have investigated active cooling techniques and demonstrated high heat transfer performance. However, these techniques require additional power and thus increase the cost and the complexity of the system. Examples of active cooling technique approaches are reviewed below. Fang et al. [21][22] experimentally investigated the effect of micro-synthetic jets on the thermal performance of a microchannel heat sink. They tested a 550 μm wide, 500 μm deep, and 26 mm long microchannel integrated with a micro-synthetic jet actuator with a 100 μm diameter orifice and reported 42% enhancement in heat transfer with a negligible pressure drop. Fang and Khan [23] also studied the thermal effect of multiple synthetic jets on single-phase cross-flow microchannels and two-phase microchannels [24]. In contrast, passive cooling techniques have been used widely to improve the heat transfer performance of a microchannel heat sink in the single-phase flow regime, by interrupting the thermal and hydraulic boundary layers by changing the surface roughness. Passive cooling techniques are practically superior to active cooling techniques and are used to avoid increased system complexity in many applications.

The literature review of this dissertation is divided into two sections: the first section focuses on enhancing the performance of single-phase heat transfer in a

microchannel using passive cooling techniques, while the second section focuses on suppressing the flow instabilities and increasing the CHF of a two-phase microchannel.

2.1 Passive Heat Transfer Enhancement Techniques in Single-Phase Flow Microchannels

Energy efficiency and lower financial costs are important factors to take into consideration for any heat transfer enhancement technique. The use of passive cooling techniques in designing microchannels is advantageous as they do not require additional power to enhance heat transfer, making it more cost-effective compared to active cooling techniques, which rely on external energy requirements and are thus more expensive. In order to enhance the heat transfer performance of a microchannel passively, various techniques have been employed, such as modification of the surface roughness [25][26][27], modification of the geometry [28][29], the use of nano-fluids [30], flow disruption, secondary flows [31][32], channel curvature [33], re-entrant obstructions [34], and out-of-plane mixing [35].

Dehghan et al. [36] studied the effects of conjugate heat transfer and constrained fluid flow on a converging microchannel heat sink and determined that converging walls enhanced the performance of the microchannel. Ghale et al. [37] investigated the effects of rectangular surface roughness in a straight microchannel and found an optimum design of rectangular roughness. Mohammed et al. [38] numerically evaluated the thermal performance of a wavy microchannel heat sink and investigated the effects of wave amplitudes, and determined that heat transfer performance in wavy microchannels was better than straight microchannels with the same cross-section. Effects of using two different nanofluids (copper and diamond in water) on a microchannel heat sink were

investigated numerically by Jang and Choi [39] and they discovered that the use of diamond-in-water nanofluid as a coolant for a microchannel heat sink improved heat transfer performance by about 10% compared to using pure water. Morshed et al. [40] experimentally investigated the effects of hydrophilic surface modification by using copper nanowires (CuNWs) coatings on a microchannel heat sink. They determined that the CuNWs enhanced thermal performance by up to ~25% in the single-phase flow region, and ~56% in the two-phase flow region with a ~20% pressure drop increase in the single-phase flow region, and a negligible pressure drop increment in the two-phase flow region. The study also reported that the effectiveness of CuNWs coatings was not dependent on mass velocities, but instead highly dependent on coolant inlet temperatures. Ali et al. [41] also incorporated CuNWs onto the bottom surface of a microchannel and reported a 24% heat transfer increment in single-phase flow. The effects of using carbon nanotubes (CNTs) in a silicon microchannel heat sink were experimentally investigated by Dietz and Joshi [42]. Due to the hydrophobic nature of the CNTs, the poor thermal performance was observed in the silicon microchannel compared with a conventional microchannel heat sink.

Moreover, Xu et al. [43] conducted experiments to study the effect of obstruction on a silicon microchannel heat sink, which can prevent continuous growth of the thermal boundary layer in microchannels. The main flow was separated into several independent zones. The results showed that heat transfer performance was enhanced by 26.4%, with a significant reduction in pressure drop compared with the conventional microchannel heat sink. Wei et al. [44] numerically simulated the effectiveness of adding a dimpled bottom surface to a rectangular microchannel. Figure 2.2 indicates the schematic of the computation domain. The microchannel used in the study was 50 μm deep and 200 μm

wide. The dimples were placed on a single row along the bottom wall with a pitch of 150 µm, at a depth of 20 µm with a dimple footprint diameter of 98 µm and were located in the middle of the microchannel. The results showed enhancement of the heat transfer coefficient with a little increase in pressure drop, with the lowest heat transfer enhancement seen on the bottom-dimpled surface, proving that dimples can be used to enhance heat transfer inside microchannels.

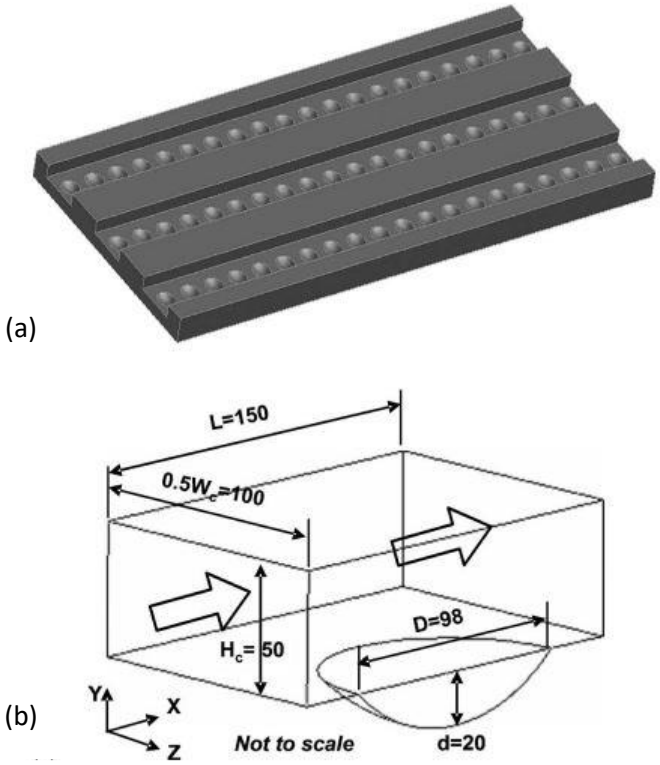

Figure 2.2 (a) Overall bottom-dimpled microchannel, and (b) Schematic of the computation domain [44].

Amitav et al. [15][32] numerically investigated the effect of an inter-connector between parallel mini-channel heat sinks, as shown in Figure 2.3. The results showed that the inter-connectors had a significant effect on counter-flowing parallel channels compared to conventional parallel-flowing channels. Specifically, the overall Nusselt number

increased by 36% for the counter-flowing channels, along with a reduction in pressure drop. Tikadar et al. [45] also numerically and experimentally investigated the utilization of secondary flow for breaking and re-developing the boundary layer, to enhance the thermal-hydraulic performance of counter flow mini-channel heat sinks. The results showed excellent agreement between the numerical simulation and experimental validation, and that the friction factors were reduced significantly at a low flow rate.

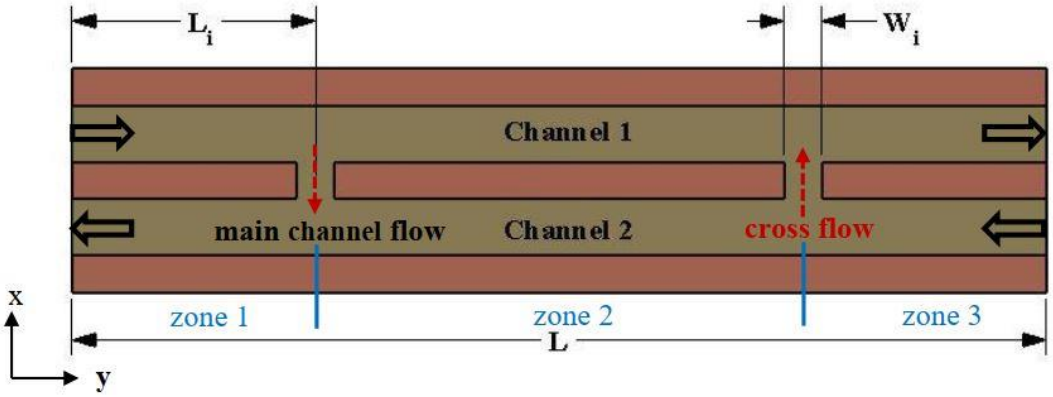

Figure 2.3 Top view of the inter-connected counter flow mini-channels [15][31].

Based on the literature above, various studies have demonstrated heat transfer augmentation in single-phase microchannels using passive cooling techniques. It is evident that the effective utilization of advanced microfabrication technologies, together with other techniques, could further improve single-phase microchannel heat transfer performances.

2.2 **Two-Phase Flow Microchannels**

Over the past few decades, there has been tremendous growth in the number of studies published regarding heat transfer in two-phase flow microchannels, given their widespread use in several applications. Two-phase flow is increasingly gaining importance to effectively dissipate the large amount of heat generated from advanced power electronics,

whose surface temperature must be kept safe and reliable, to prevent damage to the devices [46].

Flow boiling in microchannel heat sinks is one of the most effective convective heat transfer processes for cooling high-heat-flux applications, such as computer chips, lasers, and defense equipment. Due to the large surface area to volume ratio and small footprints, flow boiling microchannel heat sinks can achieve very high heat flux from high power density devices compared to conventional heat sinks [5]. However, it is still a controversial issue in microchannels because, in practical applications, flow boiling within a microchannel suffers from various instabilities, which can lead to a large pressure drop, premature CHF [47][48], and a lower and unreliable HTC. Flow boiling instability is one of the inherent and greatest challenges in microchannel deployment for many engineering applications.

Flow boiling instability in microchannels is characterized by rapid bubble expansion in both upstream and downstream directions [49], as shown in Figure 2.4 , causing irregular flow reversal and significant oscillations in flow rate, temperature, and pressure. Several studies [6-15] have been conducted in the area of flow boiling microchannels to mitigate instability in order to prevent or delay the early occurrence of CHF, and thus increase the CHF to its maximum. Flow boiling instability can be suppressed by using either passive or active techniques, the latter of which requires external power. In a review article, Wu and Sundén [25] evaluated flow boiling instability mitigation techniques in microchannels, which include inlet restriction[50], reentrant cavity [51], expanding channels [52], vapor venting [53], and surface modification [54][55], among others. They concluded that flow boiling instability in microchannels remains a

serious issue that needs to be further addressed. Khan and Morshed [56] employed a passive technique utilizing a CuNW coating on microchannel surfaces, which changed the bubble ebullition sites to enhance the CHF and delayed the onset of unstable boiling. Meanwhile, Fang and Khan [57] experimentally investigated an active technique, which introduced micro synthetic jets into flow boiling microchannels. Their study illustrated that controllable synthetic jets can effectively suppress flow boiling instabilities by introducing jet moments into the bubble dynamics to break and then to condensing the bubbles, thus increasing both the HTC and CHF. Prajapati et al. [58] investigated three different configurations of microchannels: uniform cross-section, diverging cross-section, and segmented finned microchannels. They found that in segmented channels, the bubbles had enough space to grow and extend in the lateral direction, leading to a reduction in flow instability in the segmented channel compared to the diverging and uniform channels. Zhang et al. [59] conducted an experimental study to determine flow boiling performance in an interconnected microchannel net and rectangular microchannels. Their results showed that the interconnected microchannel net mitigated the flow boiling instability at the highest mass flux.

Compared to other instability mitigation techniques, the use of an IR was determined to be the easiest and most promising passive technique to effectively suppress flow boiling instability in microchannels. In the pioneering works of Bergles et al. [60] and Bergles and Kandlikar [61], the concept of IRs was introduced in flow boiling microchannel heat sinks. However, it is not surprising that the gain of instability mitigation using this technique is at the expense of a significant increase in pressure drop across the microchannel heat sink, which eventually increases the pumping power of the cooling

system. For example, Kosar et al. [62] experimentally employed the IRs to suppress flow boiling oscillations in parallel microchannels. In their study, the IRs were placed at the entrance of each channel. The tests were conducted for mass fluxes ranging from 115 to 389 kg/m^{2}s. The results showed that at a mass flux of 265 kg/m^{2}s, the heat flux at the onset of unstable boiling was delayed by approximately 4.9 times as compared to the case without IRs, but the pressure drop increased by approximately 20 times. Qu and Mudawar [63] investigated flow boiling of water in a heat sink containing 21 copper parallel microchannels. Two types of two-phase instability were encountered in this study: pressure drop oscillation and parallel channel instability. Pressure drop oscillation produced periodic, large-amplitude flow oscillations, resulting from the interaction between vapor generation in channels and compressible volume in the flow loop upstream of the heat sink. Parallel channel instability, on the other hand, produced only mild flow fluctuations, caused by density wave oscillation within each channel and feedback interaction between channels. The study showed that severe pressure drop oscillation can be eliminated simply by throttling the flow upstream of the heat sink. This technique also resulted in a large pressure drop increase for the cooling system. However, the inlet throttling valve was unable to eliminate the parallel channel instability. Several other researchers who used IRs in microchannels to suppress the flow boiling instability also experienced similar issues of large pressure drops [62][64].

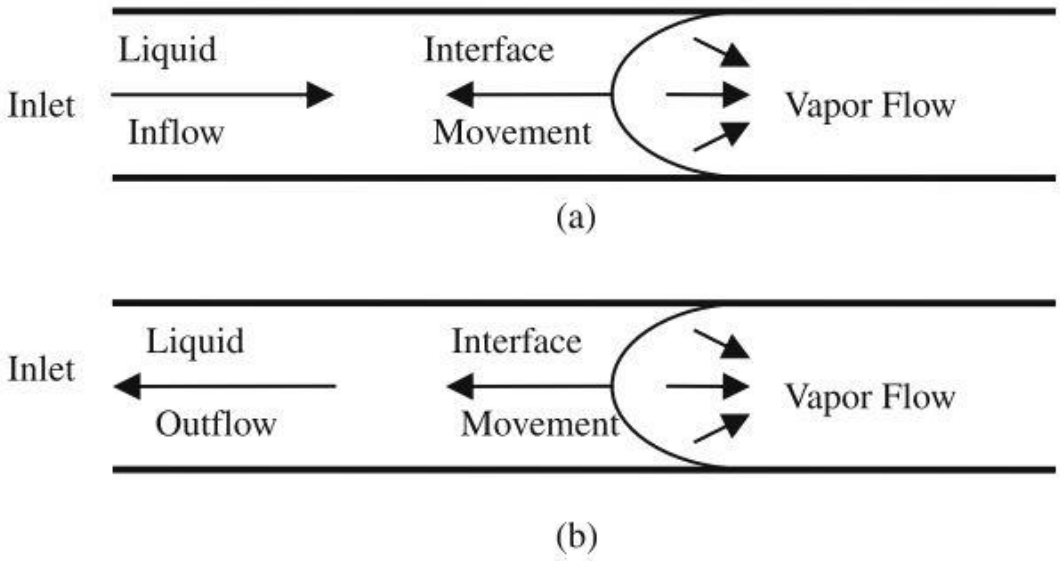

Figure 2.4 Schematic illustration of liquid flow near the inlet of microchannel with growing vapor bubble [49].

Prajapati and Bhandari [65] comprehensively reviewed recent literature covering flow boiling instabilities in microchannels and their promising solutions, as well as the major challenges during two-phase flow boiling in microchannels and its suppression techniques. The authors concluded that geometrical modification had been prominently considered to overcome the instability phenomena. The geometrical modifications mentioned in their review included the use of a V-shaped [66] or rectangular-shaped [67] IR in parallel channels, as well as the use of Ω-shaped reentrant configurations [62] to the parallel channels that have been discussed above.

Yan and Thorpe [68] experimentally and theoretically studied the flow regime transition from single-phase to two-phase bubbly flow in a pipe with a diameter of 3.78 cm, and with an inlet orifice which has an area ratio (i.e., the ratio of the orifice diameter to the pipe diameter) varying between 16.16% and 62.98%. They found that the cavitation number at inception is strongly dependent on the size of the geometry, but independent of

liquid velocity. Mishra and Peles [69] experimentally investigated hydrodynamic cavitation of de-ionized (DI) water flow through a single microchannel (100.2 μm wide x 101.3 μm deep cross-section) with a micro-orifice (area ratio = 11.47%) installed at the channel entrance. They observed that incipient cavitation is a function of the geometry of the inlet orifice. Furthermore, Mishra and Peles [70] studied flow cavitation with a different fixed size of inlet micro-orifice, but varied the microchannel width to have area ratios of 10.69%, 19.69%, and 21.45%, respectively. They found that cavitating flows in microscales were different from that in macroscales, and elucidated that choking cavitation and the cavitating numbers were affected by the size of the inlet micro-orifice. Mishra and Peles [71] also studied flow patterns in a single microchannel (202.6 μm wide x 20,000 μm long) with an IR (area ratio = 19.96%), and detected multifarious cavitating flow patterns, including incipient, choking and super cavitation. They also observed that incipient and choking cavitation numbers increased with the area ratio between the micro-orifice and the microchannel while the orifice discharge coefficient plummeted once cavitation activity erupted. In addition, for a fixed microchannel width, the incipient, and the choking cavitation numbers rose with the ratio between the hydraulic diameters of the micro-orifice and the microchannel. The authors also indicated that the flow patterns encountered at choking and supercavitation were significantly influenced by the micro-orifice and microchannel size. Furthermore, they concluded that flow and cavitation hysteresis was observed but effects were more pronounced for the smallest micro-orifice.

The area ratio of the inlet restriction to the microchannel is a key parameter for the IRs to function effectively to suppress boiling instability in a microchannel. Kandlikar et al. [72] experimentally evaluated the effects of an IR in front of each channel, and

fabricated nucleation sites on the bottom surface of each channel to stabilize flow boiling instability and to avoid the backflow between parallel channels. The authors tested two area ratios of 51% and 4% and found that the IRs with both area ratios helped in suppressing the instability. The experiment with the 4% area ratio eliminated the pressure fluctuation but significantly increased the pressure drops. They recommended that further research was required to study the effect of pressure drop elements and different sizes of nucleating cavities. Schneider et al. [73] conducted an experiment to investigate heat transfer in the presence of hydrodynamic cavitation by using 20 μm wide inlet micro-orifices entrenched inside 227 μm hydraulic diameter microchannels (area ratio of 10%). They reported a significant enhancement of heat transfer during super cavitating flow conditions compared to non-cavitating flows, with a minimal pressure drop. However, no explanation was provided as to their choice in using this specific percentage of area ratio in their design. Kosar et al. [74] conducted an experiment for flow boiling using DI-water as the coolant in microchannels to investigate the effects of the length of IRs, which was installed at the entrance of each channel. In their study, they used an area ratio of 10% in order to suppress flow instability. They found that the longest length of the IR helped to increase the CHF but led to higher pressure drops. Wang et al. [66] studied the effect of inlet/outlet configuration on flow boiling instability in trapezoidal-shaped parallel microchannels. Figure 2.5 indicates the IRs were fabricated in front of the channels, where an area ratio of 20% was used. They found that nearly steady flow boiling existed in the parallel microchannels with the IR shown in Figure 2.5 , demonstrating that IRs can have a large effect on flow boiling instability in microchannels. Lu and Pan [75][76] experimentally investigated flow boiling instability in ten parallel microchannels with a

diverging cross-section design, with an area ratio of 17.85%. The diverging design was used to restrict the backflow in order to suppress the instability. They demonstrated that the diverging microchannel significantly prevents the reversal flow and was more stable than the converging channel. Dai et al. [77] experimentally investigated a flow separation technique for a microgap (5.5 mm x 0.35 mm) to demonstrate that the pressure drop and heat transfer could be significantly improved. Figure 2.6 illustrates the schematic of the design used in their experiment, in which a portion of the incoming flow was routed to the middle of the microgap through a passive microjet. To realize the flow distribution, an IR with an area ratio of 14% was placed at the entrance of the microgap, as shown in the figure. This technique improves the CHF by injecting subcooled liquid flow into the middle of the boiling microgap flow, which leads to condensation of the bubbles.

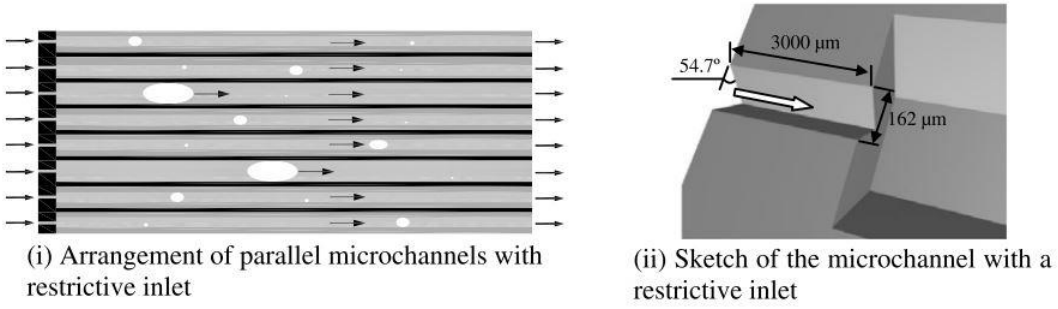

(i) Arrangement of parallel microchannels with restrictive inlet

(ii) Sketch of the microchannel with a restrictive inlet

Figure 2.5 Schematic representation of IR used in a trapezoidal-shaped parallel microchannel [66].

Li et al. [78] experimentally investigated the effects of triangular cavities, which were carved into the sidewalls of the microchannels, on the flow boiling performance. In their design, IRs with area ratios of 25% were fabricated at the entrance of each microchannel. Their experiment results indicated that the microchannels with triangular cavities presented significant enhancement of heat transfer, obvious reduction of pressure

drop, as well as more stable and uniform wall temperatures compared to the microchannels without triangular cavities.

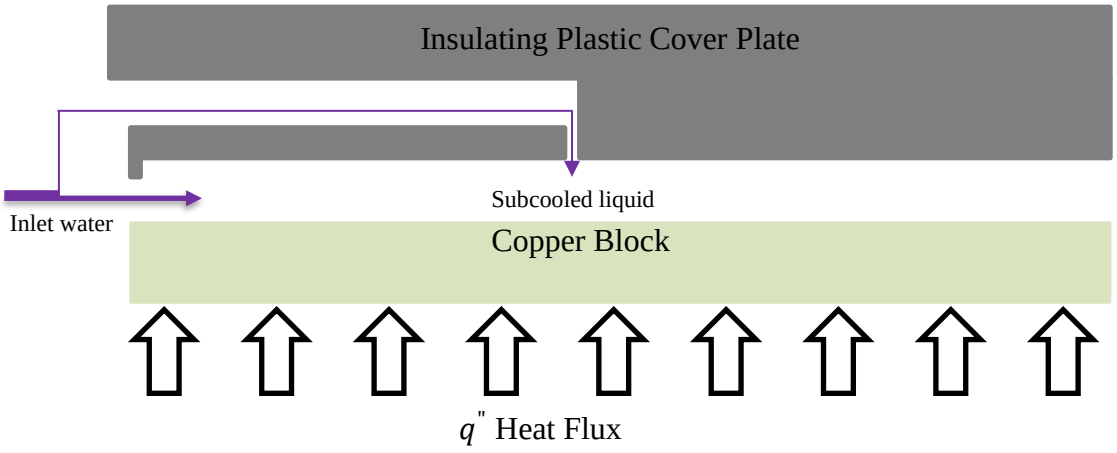

Figure 2.6 Schematic of flow separation setup using a microgap [77]

In addition to suppressing flow instability in microchannels, some researchers employed IRs to enhance the CHF of the flow boiling microchannels [74][79][80]. Mukherjee and Kandlikar [81] numerically investigated bubble growth in a microchannel by using an IR with two area ratios of 4% and 51%. The results demonstrated that increasing the inlet flow velocity could eliminate backflow.

In summary, the above studies using IRs, orifices and throttle valves to suppress flow boiling instabilities in microchannels were mostly limited to employing fixed-size IRs or orifices to suppress the flow instabilities as much as possible. This inevitably induced significant pressure drop penalties. Not enough attention has been given to the configurations and design parameters of the IRs, which may lead to optimum designs of IRs that can fit best for some operational range of the microchannel heat sink, with much smaller pressure drop penalties. Therefore, in the present study, the multi-IRs concept [82]

will be introduced, which has not been studied in both the single-phase and two-phase flow regimes in microchannels. To experimentally investigate the various designs of the IRs, a single microgap with a large aspect ratio of 13.12 was chosen as the basis for this study. Microgap cooling has many industrial and military applications. Although the approach of fabricating parallel microchannels directly into the chip/substrate may not be applicable in emerging three-dimensional integrated circuitry thermal management due to space limitations, utilizing the microgap between chips in three-dimensional stacks as a cooling channel is a promising "embedded" cooling strategy [83]. These gaps typically have 1 cm wide dimensions, with a channel height in the range of 100 to 500 μm [83]. However, two-phase flow boiling instabilities in microgap cooling remains to be a critical issue due to the early presentation of CHF. To counter this issue, this research will utilize multiple restrictors in a microgap configuration.

CHAPTER 3

EXPERIMENTAL FACILITY

To accomplish the aforementioned research objectives, an experimental system was designed and built in the Mechanical Engineering Department at the University of South Carolina. This system was designed to conduct experimental studies of the enhancement of heat transfer for both single-phase and two-phase flow in microchannels.

This chapter is organized as follows. Section 3.1 describes the experimental setup and procedures. Section 3.2 presents the test module. Section 3.3 presents uncertainty analysis. Section 3.4 presents calibration of instruments. Section 3.5 presents data aquistion system. Section 3.6 presents experimental procedure. Section 3.7 presents experimental data reduction for single-phase flow. Section 3.9 presents experimental data reduction for two-phase flow.

3.1 Experimental Setup and Procedures

3.1.1 Flow Loop

Figure 3.1 shows the schematic setup of the experiment facility. The water flow loop was designed to supply a constant flow rate of de-ionized water to the test section at the desired temperature and pressure. A digital gear pump (drive: Cole Parmer EW-75211-70; pump head: Micropump EW-74004-21) was used to provide a constant flow rate of water from a reservoir tank. A 40 μm inline filter followed the gear pump to remove solid particles that may cause blockage of the microchannels. A degasifier (MiniModule^{TM} Membrane G543) was used to remove dissolved gases from the de-ionized water before it

entered the test section, and a thermal bath (NESLab RTE7) was used to maintain the designated water inlet temperature for all experiments conducted in this study. Finally, the water that was drained out from the test section was ducted into a container placed on a high precision balance, which was employed to calibrate the mean flow rate further. Figure 3.2 shows a photograph of the assembled experimental system.

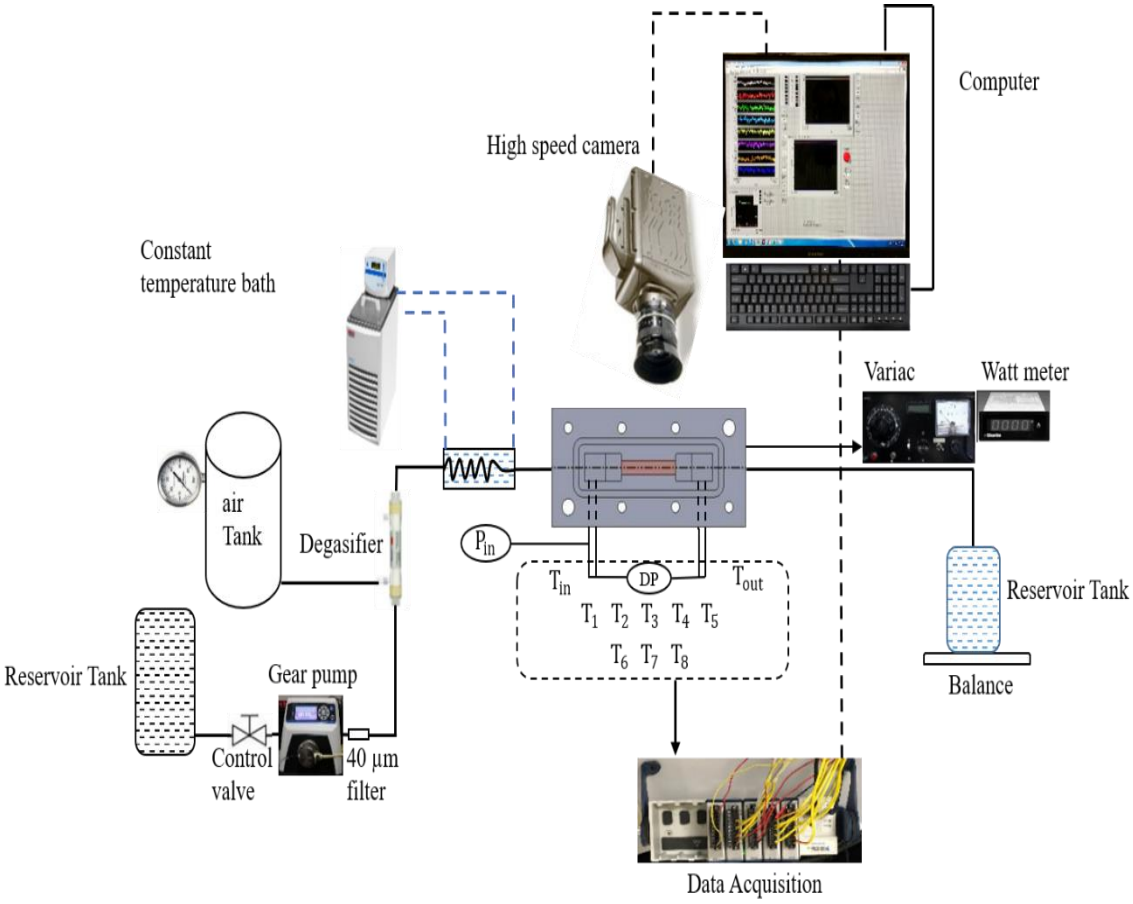

Figure 3.1 Schematic of the experiment system

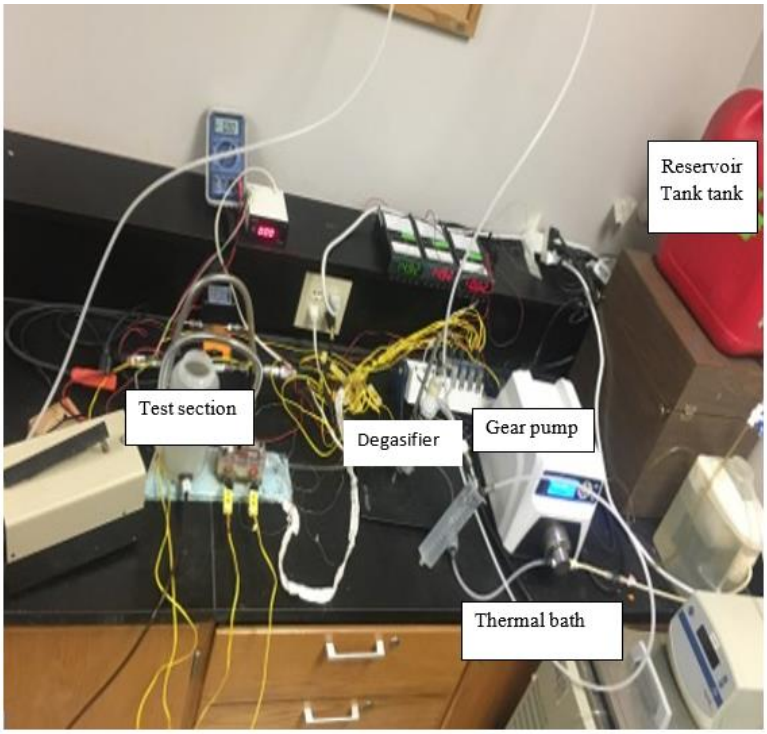

Figure 3.2 Photograph of the experimental facility.

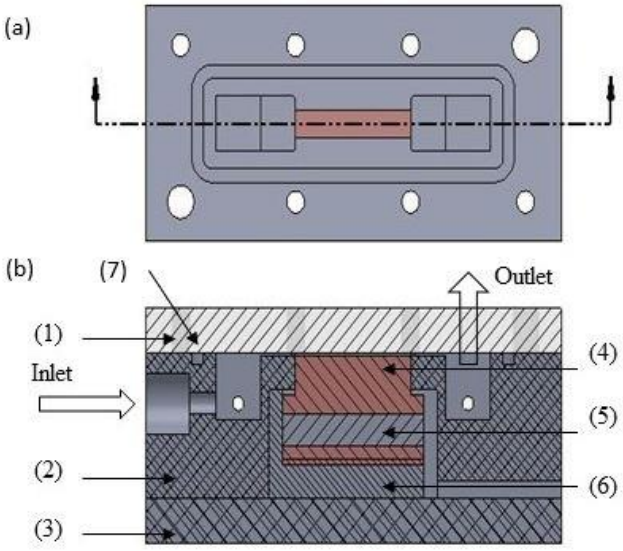

Figure 3.3 (a) The top view, (b) Cross-sectional view of the housing componenet.

3.2 **Test Modules**

The test section, as shown in Figure 3.3, consists of seven parts: (1) a cover plate (polycarbonate plastic); (2) a housing block (G-7 fiberglass); (3) a bottom plate (polycarbonate plastic); (4) the copper test section; (5) a cartridge heater; (6) an insulation block; and (7) a rubber O-Ring located at the interface between the cover plate and the top surface of the housing to prevent leakage.

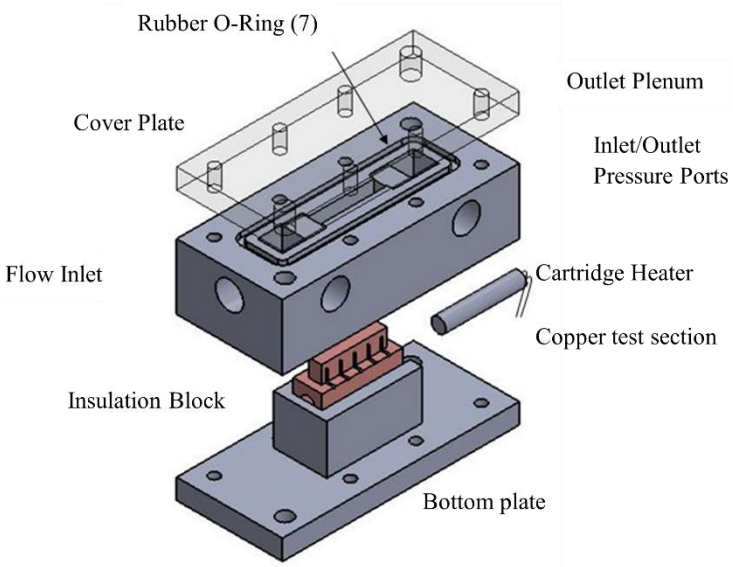

Figure 3.4 Assembled and exploded view of the test section

Figure 3.4 depicts the assembled and exploded view of the test section while, Figure 3.5 shows the schematic of microchannel heat sink. Meanwhile, Figure 3.8 provides a cross-sectional view of the test section. As shown in these figures, after assembly, the bottom surface of the top cover plate is tightly pressed against the top surface of the housing component by eight bolts, to ensure that rubber O-ring is pressed entirely into the O-ring slot.

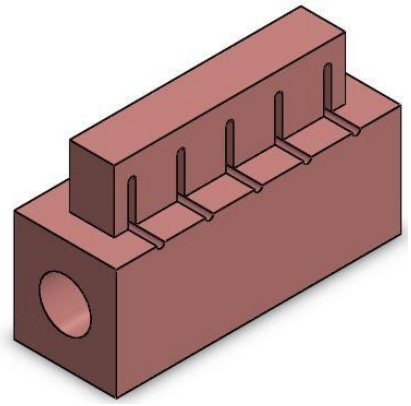

Figure 3.5 The schematic of the microchannel heat sink.

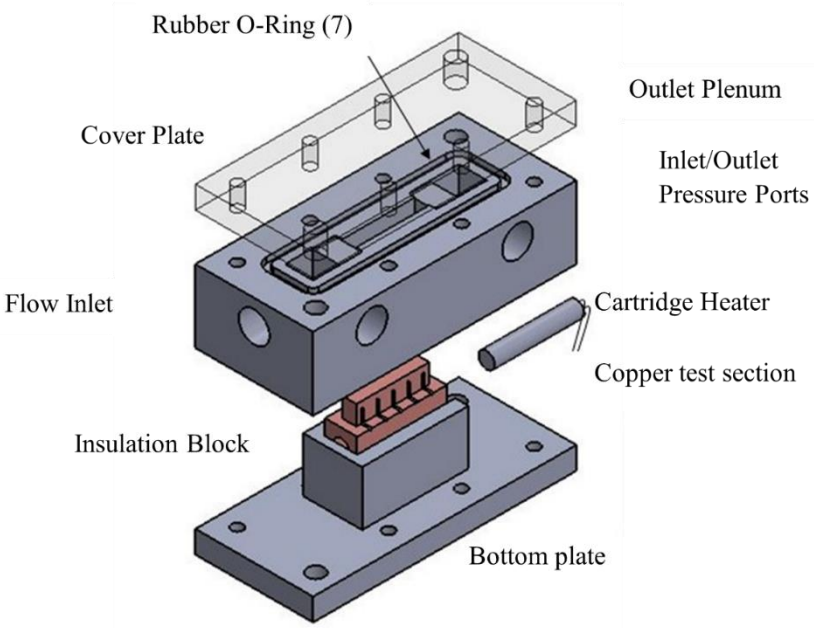

Figure 3.6 Assembled and exploded view of the test section.

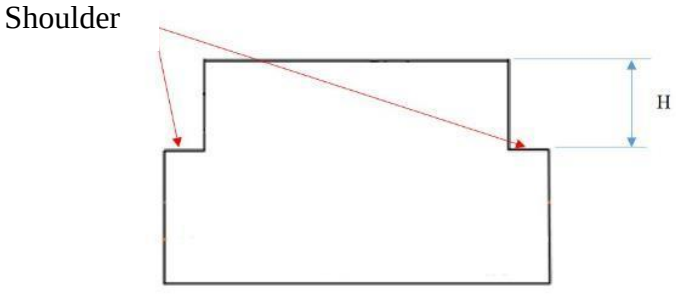

Figure 3.7 Dimension control of the heat sink.

The exact height of the channel is controlled by the precise dimension “H”, as depicted in Figure 3.7 below. During assembly, as shown in Figure 3.7, the shoulder (the protruding portion around the periphery) of the heat sink is flushed with the inner wall of the housing component, to ensure the exact height of the channel was maintained after assembly.

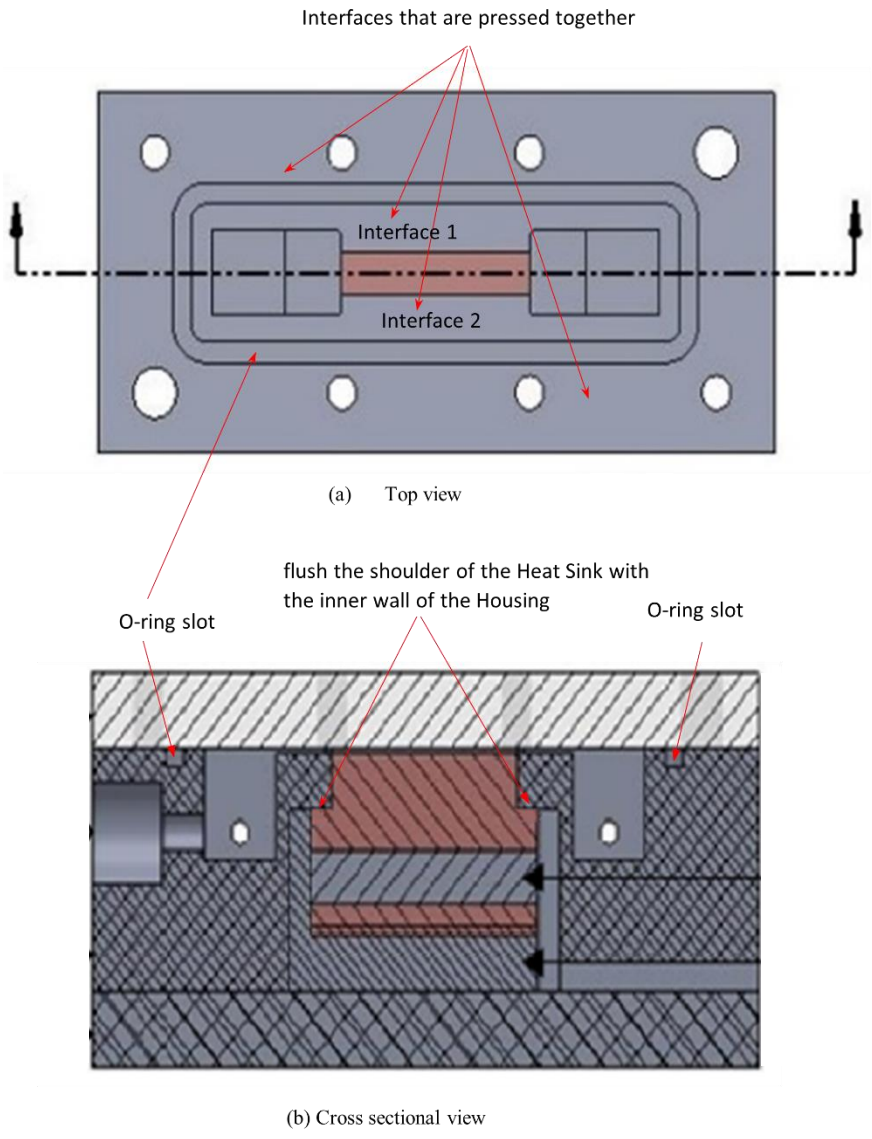

Figure 3.8 Cross-sectional view of the test section.

3.2.1 Microchannel

Figure 3.9 depicts the copper heat sink, which was made from a single block (oxygen-free copper 101). The thermal conductivity of the copper block was 391 W/m·K. The dimension of the microchannel was measured as 26 mm (L) x 5 mm (W) x 0.5 mm (H), which gave a hydraulic diameter of 909 μm. A single rectangular microchannel was formed during assembly by the gap between the top surface of the copper block and the bottom surface of the cover plate. Five holes each with a diameter of 0.85 mm and a depth of 2.5 mm were drilled into the sidewall of the copper block, at 2.1 mm below its top surface. Five Type K thermocouples were inserted into the holes to measure the wall temperature. The locations of the thermocouples were 2 mm, 7.5 mm, 13 mm, 18.5 mm, and 24 mm from the inlet of the microchannel, corresponding to T1, T2, T3, T4 and T5 respectively. The following two-step procedure was adopted while preparing the microchannel heat sinks used in this study as shown in Figure 3.10. In Step 1, the top surface of the heat sink was first mechanically polished by using sandpaper with grades of 400, 600, 800, and 1500. In Step 2, the heat sink was rinsed with acetone, ethanol, and de-ionized water sequentially, followed by a drying process with a nitrogen stream [84].

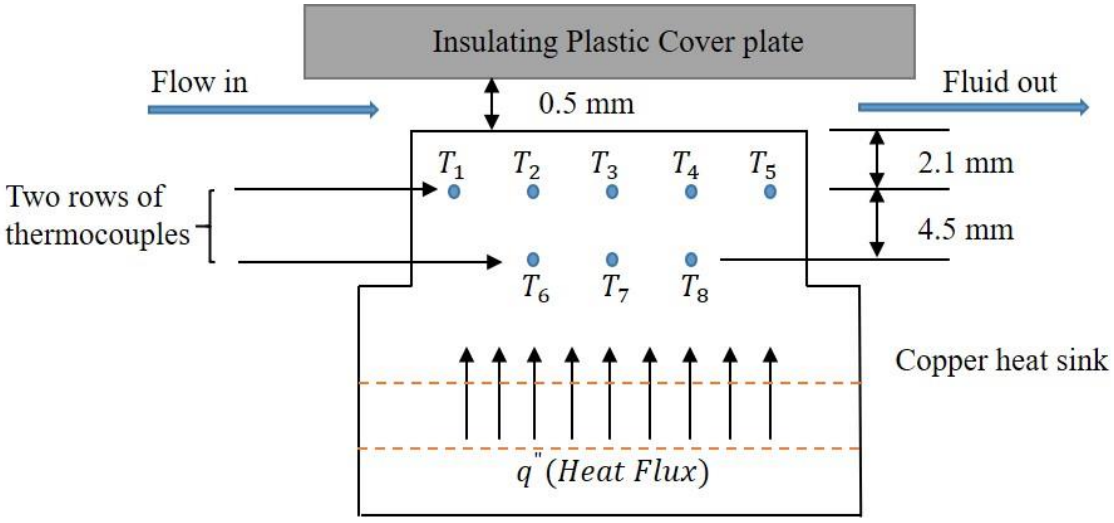

Figure 3.9 Microchannel heat sink diagram.

Figure 3.10 Fabrication procedure.

3.3 **Uncertainty Analysis**

Uncertainties for measured quantities using thermocouples, differential pressure transducers, as well as voltage and current measurements were obtained from the instrument's specifications, which are $\pm$0.25 K, $\pm$0.25%, ±0.15% and ±0.5% respectively. Uncertainties for the derived quantities were calculated using the Kline and McClintock method of experimental uncertainty [85] in the following Eq. (3). The computed results showed that the uncertainties in the effective heat flux and heat sink surface temperatures were ±4-15% (depending on the mass flux) and ±1.5 °C respectively. The computed results for the uncertainties in the heat transfer coefficient, and the pressure drops were ±6-18% (depending on the mass flux), and ±4%, respectively. Selected experiments were repeated, some more than twice, and the average deviation between the two tests for mass fluxes G = 32.68 kg/m^{2}s was less than 2.6%.

$$P = f(x_1, x_2, \ldots . x_n) \rightarrow U_P = \sqrt{\sum_{i=1}^{n} \left\{ \frac{\partial P}{\partial x_i} U_{(x_i)} \right\}^2} \quad (3)$$

3.4 **Calibration of Instruments**

Before running the setup, all the thermocouples and pressure transducers were tested and calibrated. Type K thermocouples (model 5TC-TT-K-36-36), manufactured by Omega Engineering, were extensively used in all the experiments. All eight thermocouples were calibrated using a high precision thermal bath (ThermoNESLAB model RTE7), which had an accuracy of ±0.1 K. The results of the calibration are plotted in Figure 3.11, which show that the average deviation between the thermocouple readings and the setting temperatures of the thermal bath varied from 0.025% to 0.07%. The pressure transducers

(model PX319-050GI) were calibrated by the manufacturing company Omega Engineering, with an accuracy of ±0.25%.

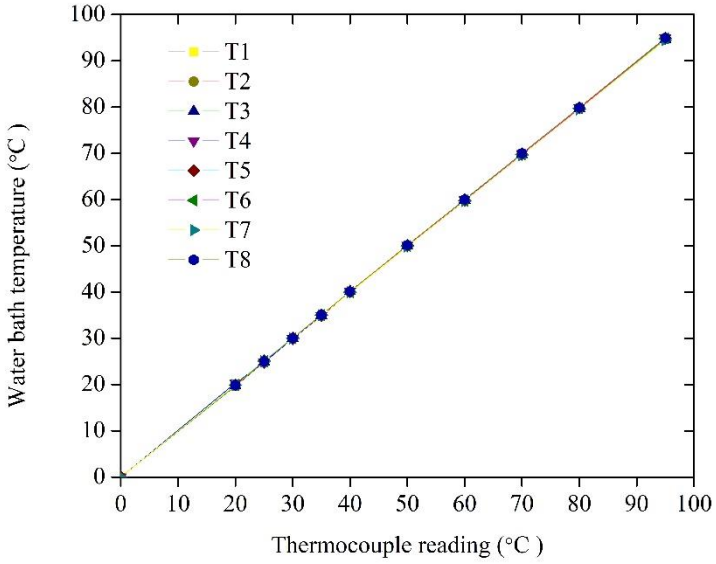

Figure 3.11 Thermocouple calibration.

3.5 **Data Acquisition System**

A NI Compact DAQ-9172 data acquisition system, developed by National Instruments, with LabVIEW software was used to record the eight Type K thermocouples, two absolute pressure transducers, and one differential pressure transducer. NI 9211 and NI 9203 acquisition cards were used to convert the signals to temperature and pressure readings, respectively. The NI 9211 is a 24-Bit, ±80 mV analog input module with four channels and 14 S/s sampling rate. The NI 9203 is a 16-bit analog current input module with eight channels, 4-20 mA current input, and up to 200 kS/s sampling rate. The system communicated with a computer via a USB interface. A program written in LabVIEW software was used for all data acquisition, as illustrated in Figure 3.12.

3.6 **Experimental Procedure**

The following experimental procedure was applied for each test. Once the test section was prepared, the whole section apart from the water supply tubes was placed in a foam box to reduce convection and radiation heat losses. The desired flow rate for each test run was maintained constant using the gear pump. The heater power supply was turned on and kept at the appropriate level by adjusting the voltage meter manually. Furthermore, during the test, the resistive cartridge heater was powered by an AC power supply; where the AC power was first supplied to a Voltage Stabilizer so that stable power was provided to the variac (variable transformer), where the variac was used to control the power level supplied to the test module. During the test, the heating power was adjusted with a small incremental via the variac, and data were recorded for each of the power levels after reaching their respective steady state. A steady state was usually reached in 90-150 minutes after the flow rate became stable. The temperature and pressure from the thermocouples and pressure transducers were monitored using LabVIEW software, which was connected to the data acquisition system. Once the average temperature of 100 readings of the thermocouples remained constant over a 15-minute time interval, a steady-state condition was considered to be reached.

.

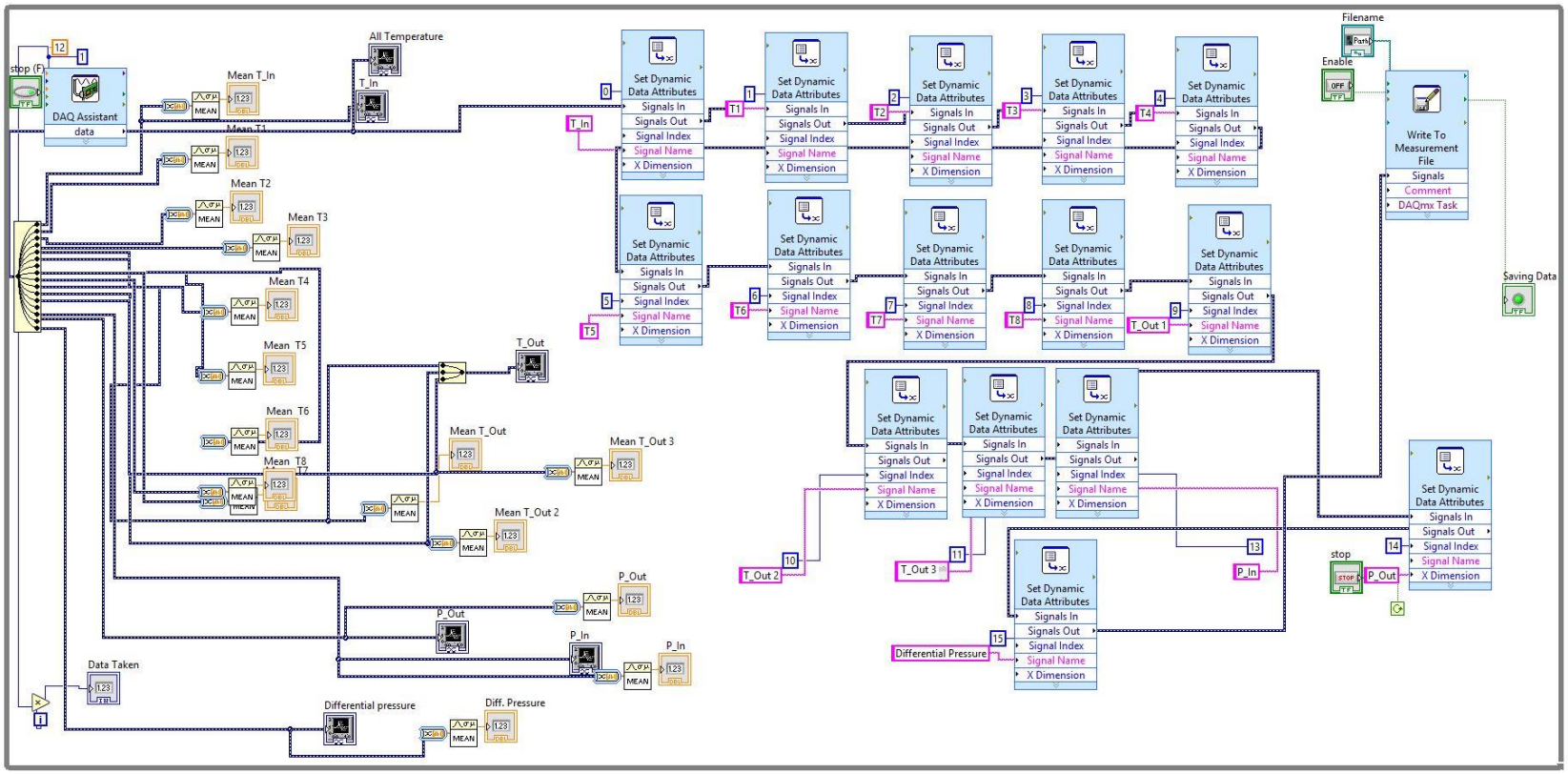

Figure 3.12 Block diagram of the LabView program.

After the system had reached the steady state, the thermocouple readings, pressure transducer readings, water flow rate, and heating power were recorded for 500 data points each. The recordings were repeated thrice for each test within 5-minute intervals. For two-phase flow experiments, when the flow boiling was near the CHF (estimated based on the temperature of the heat sink monitoring in the LAVBIEW data acquisition system), the power was increased with smaller increments until the steady state was reached, and increased to the next power level, until the CHF was reached. At CHF, an abrupt and steep temperature rise was indicated in LAVBIEW, with a very small increment in the amount of power. At that point, the power supply was immediately turned off to avoid burnout of the test section. The entire procedure was repeated until the CHF was reached again, to ensure that the "true" CHF was achieved.

3.7 **Experimental Data Reduction For Single-Phase Flow**

The sensible heat, q , can be calculated from the energy balance in single-phase flow,

$$q = \rho CpQ(T_o - T_i) \tag{4}$$

where Q is the water volumetric flow rate, ρ is water density, Cp is water specific heat, T_i and T_o are the average inlet and outlet temperature of the water, respectively. The density and specific heat were calculated based on mean bulk water temperature (T_b),

$$T_b = \frac{T_i + T_o}{2} \tag{5}$$

The heat loss can be obtained by the following equation,

$$Q_{loss} = Q_{input} - \rho CpQ(T_o - T_i) \tag{6}$$

where Q_{input} =V.I is the total electric power input. Voltage (V) and current (I) were measured using a voltameter and wattmeter. The maximum heat loss during the experiment was recorded at around 20%, corresponding to the lowest Reynolds number.

The average HTC along the microchannel heat sink was determined by Eq. (7),

$$\bar{h} = q/[A_{ht} \cdot \Delta T_{LMTD}] \tag{7}$$

where q is the effective heating power, A_{ht} is the microchannel wall surface area (26 mm x 5 mm), and ΔT_{LMTD} is the log mean temperature difference given by the Eq. (8),

$$\Delta T_{LMTD} = \frac{(T_{w,1} - T_i) - (T_{w,5} - T_o)}{\ln\left({(T_{w,1} - T_i)}/{(T_{w,5} - T_o)}\right)} \tag{8}$$

where $T_{w,1}$ and $T_{w,5}$ are the local bottom wall temperature near the inlet and outlet of the microchannel respectively, which were calculated by assuming one-dimensional heat diffusion through the copper substrate by using Eq. (9),

$$T_{w,j} = T_j - H \cdot q"/k_{cu} \tag{9}$$

where $T_{w,j}$ is the local wall surface temperature corresponding to the embedded thermocouples; T_j is each thermocouple reading; H is the distance from the thermocouples to the microchannel bottom wall surface, which is 2.1 mm in this case; and k_{cu} is the copper thermal conductivity. Finally, the corresponding average Nusselt number (Nu) was calculated using Eq. (10),

$$Nu = \frac{h_{avg} D_h}{k_f} \tag{10}$$

where D_h denotes the hydraulic diameter of the microchannel, and k_f is the thermal conductivity of water, evaluated at the mean temperature averaged between the inlet and outlet water temperatures of the channel.

The Reynolds number (Re) was calculated based on the inlet properties of the water, as given in Eq. (11),

$$Re = QD_h\rho/\mu A_{ch} \tag{11}$$

where μ is the viscosity of water, which is calculated based on the inlet temperature and A_{ch} is the channels cross-sectional area (5 mm x 0.5 mm).

The friction factor for the single-phase microchannel flow was calculated using the following equation,

$$f = \frac{2\left(\Delta p/_L\right)D_h}{\rho u_m^2} \tag{12}$$

where u_m denotes the mean fluid velocity in the microchannel, which is computed using the expression of $u_m = \dot{m}/(\rho A_{ch})$; and where, Δp is the pressure difference between inlet and outlet of the channel, determined by Eq. (13).

$$\Delta p = p_{in} - p_{out} \tag{13}$$

3.8 **Experimental Setup Validation**

The experimental setup was designed and constructed as a new system at the Mechanical Engineering Department of the University of South Carolina. To ensure that the instrumentations and data reductions of the experimental setup were correctly implemented, single-phase heat transfer performance and pressure drop for the base case, i.e., microchannel heat sink without surface modification was validated with well-established correlations. Figure 3.13 shows the comparison between the experimental average Nu obtained from the experiment using Eq. (10) and the Nu calculated from the correlation of Shah and Bhatti [86] as reproduced in Eq. (14) and Eq. (15) and Saad [87]. The comparison illustrates that the experimental work is in excellent agreement with the

established correlation. The maximum deviation of Nu was around 3.75% at the highest Re, and 3.29% at the lowest Re. This benchmark gave us confidence for the following experimental work. Figure 3.14 shows the comparison of the friction factor calculated from the experiment using Eq. (12) and the result calculated from the correlation of Shah and London [88], Amitav [15], and Saad [89]. For easy reference, these two correlations were reproduced in Eq. (16) and Eq. (17), respectively. The maximum deviation was around 10.22% and 12.33% at the lowest and highest Re, respectively. The comparisons illustrate that the experimental results are in well agreement with established correlations. This validation serves as the basis for the following experimental work.

$$\mathrm{Nu} = 1.953(RePrD_h/L)^{1/3} \; ; \; \left(\frac{RePrD_h}{L}\right) \geq 33.3 \tag{14}$$

$$\mathrm{Nu} = 1.953(RePrD_h/L)^{1/3} \; ; \; \left(\frac{RePrD_h}{L}\right) \geq 33.3 \tag{15}$$

$$f_{app}(L)Re_{ave,o\text{-}L} = \sqrt{\left[\frac{3.2}{(L/D_h\,Re)^{0.57}}\right]^2 + (fRe)_{fd}^2} \tag{16}$$

where

$$(fRe)_{fd} = 96(1 - 1.3553\alpha + 1.9467\alpha^2 - 1.7012\alpha^3 + 0.9564\alpha^4 - 0.2537\alpha^5) \tag{17}$$

Eq. (16) and Eq. (17), are valid for fully developed laminar flow.

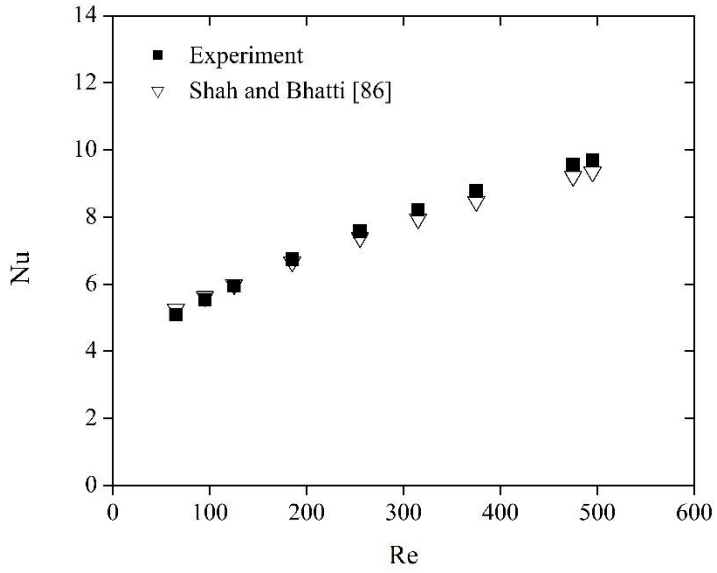

Figure 3.13 Experimental validation of Nusselt number for the base case as a function for single-phase [86][87].

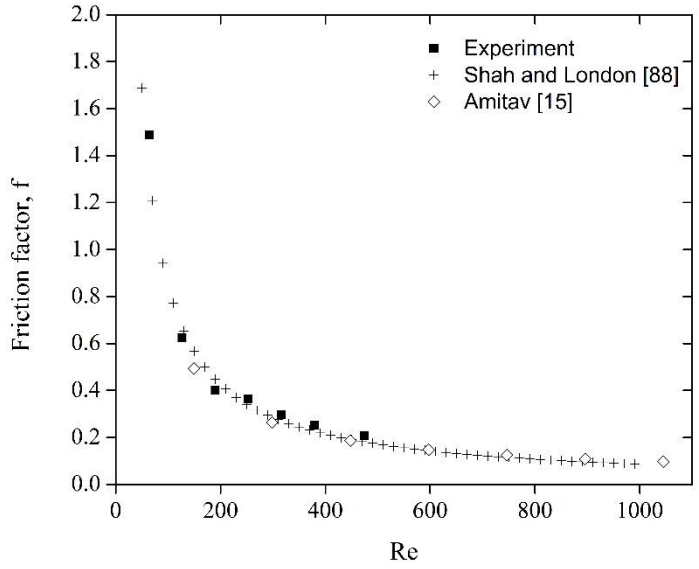

Figure 3.14 Experimental validation of friction factor for the base case as a function of Re [15][88][89].

3.9 **Experimental Data Reduction for Two-Phase Flow**

For two-phase flow, the effective input heat fluxes $q^{"}$ were calculated using data measured from the two rows of thermocouples as shown in Figure 3.9, with the following expression,

$$q^{"} = k\frac{\Delta T}{\Delta x} \tag{18}$$

where k is the thermal conductivity of copper and Δx (= 4.5 mm) is the distance between two rows of thermocouples, and

$$\Delta T = \frac{T_2 + T_3 + T_4}{3} - \frac{T_6 + T_7 + T_8}{3} \tag{19}$$

The average surface temperature, T_w, is given by:

$$T_w = \frac{1}{5}\sum_{i=1}^{5} T_{i,w} \tag{20}$$

and

$$T_{i,\mathrm{w}} = T_i - q^{"}\frac{\Delta x'}{k}\ ,(i = 1,\ldots,5) \tag{21}$$

where, $T_{i,w}$ denotes the local surface temperature along the flow direction, T_i is the corresponding thermocouple reading, and $\Delta x'$ (= 2.1 mm) is the distance between the first row of thermocouples and the top surface of the heat sink, as shown in Figure 3.9.

Figure 3.15 below shows the measured temperatures for T_2, T_3 and T_4, at locations shown in Figure 3.9 under the test condition of G = 144 kg/m^{2}s and q" = 22.61 W/cm^2, 37.42 W/cm^2, 74.80 W/cm^2 and 92.08 W/cm^2, respectively. It is noteworthy to mention that for q" = 22.61 W/cm^2, the heat transfer is in a single-phase regime as the wall temperatures are around 86 ^{o}C. The heat transfer is in the two-phase regime when q" = 37.42 W/cm^2, 74.80 W/cm^2, and 92.08 W/cm^2, respectively. The wall temperatures are nearly uniform for the single-phase and/or the two-phase conditions. Therefore, the

treatment of wall temperature using T_w computed using Eq. (19) is reasonable. A similar approach was adopted by several other researchers [77].

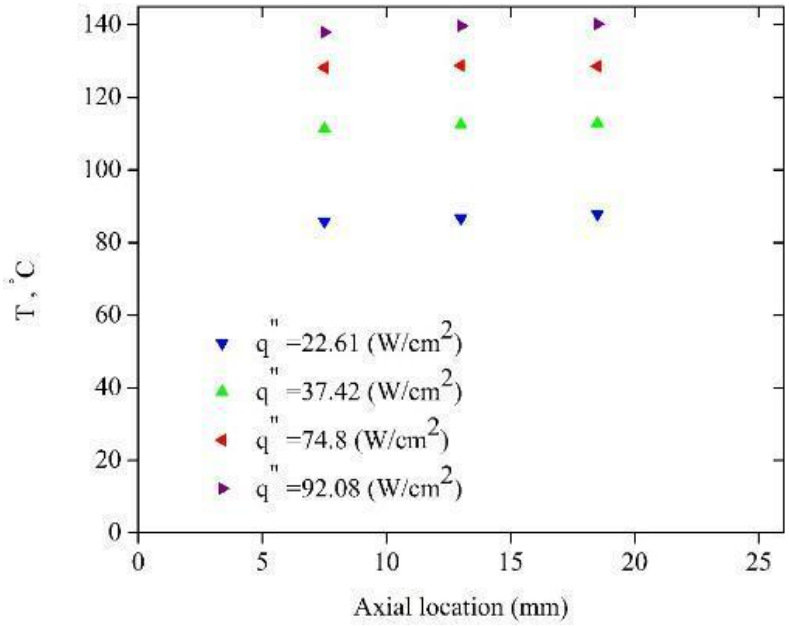

Figure 3.15 Wall temperatures measured at axial locations 7.5 mm, 13 mm and 18.5 mm (corresponding to T_2, T_3 and T_4, respectively), under the test condition of G = 144 kg/m^{2}s and q" = 22.61 W/cm^2, 37.42 W/cm^2, 74.80 W/cm^2, and 92.0 W/cm^2, respectively.

During saturated flow boiling, the flow in microchannel can be divided into two regions [90]: an upstream single-phase region with a length of L_{sub} and a downstream saturated two-phase region with a length of L_{sat}. The position between the two regions is located at zero thermodynamically equilibrium quality (i.e., $x_e = 0$). Figure 3.16 illustrates a diagram of these two flow regions.

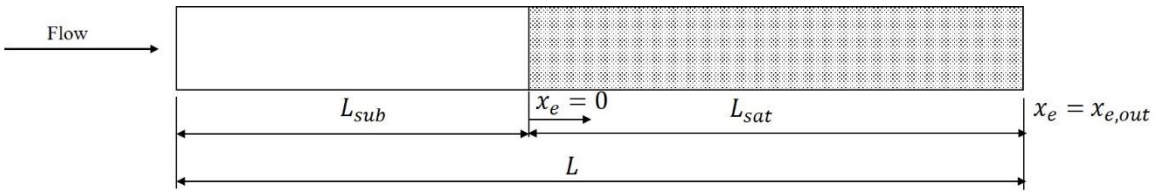

Figure 3.16 Schematic of flow regions during saturated flow boiling [90].

The lengths of the two regions were evaluated by using the following two equations [90],

$$L_{sub} = \frac{\dot{m}\, c_{p,f}(T_{sat} - T_{in})}{q^{"}W} \tag{22}$$

and

$$L_{sat} = L - L_{sub} \tag{23}$$

where T_{sat} is the saturation temperature. The vapor quality was calculated from [91],

$$x_e = \frac{q^{"}WL - \dot{m}\, c_{p,f}(T_{sat} - T_{in})}{\dot{m}\, h_{fg}} \tag{24}$$

The following two equations (25) and (26) were used to compute the HTCs [57],

$$h_{sp} = q^{"} / \left(T_w - \frac{T_{in} + T_{sat}}{2}\right) \tag{25}$$

$$h_{tp} = \frac{q^{"}}{(T_w - T_{sat})} \tag{26}$$

where h_{sp} is the average heat transfer coefficient for the single-phase region, and h_{tp} is the average heat transfer coefficient for the two-phase region. The overall average heat transfer coefficient of the heat sink for saturation boiling was obtained using the weighted average method [57] as shown below.

$$h_{avg} = \frac{h_{sp}L_{sp} + h_{tp}L_{tp}}{L} \tag{27}$$

The CHF ratio, q_r, which serves as a measure of the CHF enhancement, is defined as:

$$q_r = \frac{q^{"}_{mIR,\,CHF}}{q^{"}_{0IR,CHF}}, m = 1,3,5 \tag{28}$$

where $q''_{mIR,\,CHF}$ denotes the CHF for cases with IRs, and $q''_{0IR,CHF}$ denotes the CHF for the corresponding base case. The pressure drop through the IRs and the microchannel was calculated using the following equation,

$$\Delta p_{mIR+ch} \equiv \Delta p_{IR} + \Delta p_{ch} = \Delta p_{exp} - \Delta p_{losses},\ \ \mathrm{m} = 1,3,5 \tag{29}$$

where, Δp_{IR} and Δp_{ch} denote the pressure drop through the IRs and the microchannel, respectively; Δp_{exp} is the pressure drop measured directly from the differential pressure transducer, and Δp_{losses} defined as follows [92],

$$\Delta p_{losses} = \Delta p_{c1} + \Delta p_{c2} + \ \Delta p_{e1} + \Delta p_{e2} \tag{30}$$

where, Δp_{c1} and Δp_{c2} represent the pressure drops due to the abrupt contractions from the deep plenum to the shallow plenum, and from the shallow plenum to the entrance of IR, respectively; and Δp_{e1} and Δp_{e2} represent the pressure drop due to the abrupt expansion from the exit of the microchannel to the shallow plenum, and from the shallow plenum to the deep plenum, respectively [92]. For the 0IR case, Δp_{c2} represents the pressure drop due to the abrupt contractions from the shallow plenum to the entrance of microchannel.

The opening ratio is an important indicator to quantify the effectiveness of the IRs, which is defined as the cross-section area of the slot openings to the cross-section area of the microchannel, as shown in Eq (31).

$$AR = \frac{[AR_{mIR}]}{[AR_{ch}]}, m\ from\ 4.2\%\ to\ 100\% \tag{31}$$

CHAPTER 4

SINGLE-PHASE MICROCHANNEL HEAT TRANSFER ENHANCEMENT

The first objective of this research is to use diamond-patterned and knurling sandblasting techniques to modify the surface roughness of the microchannels to improve the heat transfer performance in single-phase applications. This chapter presents all the testing results for the single-phase microchannels engineered with diamond knurling and sandblasting surfaces, respectively. For diamond knurling surfaces, two test sections with different surface roughness values were fabricated: one has a higher surface roughness (R-1), and the other has a lower surface roughness (R-2). Both cases were tested under the same flow and heating conditions. And for sandblasting surfaces, two cases were investigated: a hybrid sandblasting of elliptical-patterned surface (HSEP), and fully sandblasting the surface (FS). For all the experiments, the Reynolds numbers were in the range of 65 to 650.

4.1 Characterizing Micro-Channel Knurling

The knurled microstructures for heat transfer enhancement are mainly considered for the applications where spaces are so compact that straight fin or pin-fin microchannels are hard to be fabricated onto those devices, such as the plates in compact plate heat exchangers, the inner wall of small diameter tubes used for condensation devices, etc. Because of its simplicity and easy manufacturing to form smaller-sized patterns, the cost

effectiveness of knurled microstructures outperforms that for the straight fins and pin-fin designs, especially on those curved surfaces or annulus. Also, compared to those structured surfaces produced by formed-low-fin surfaces and particle-coated surfaces, the reliability of a knurled surface is better because machining is relatively more reliable than forming or coating.

4.1.1 Sample Design

In the present study, a new design of the three-dimensional diamond-knurls type of surface roughness was studied. The heat transfer performance and pressure drop of single-phase flow through a microchannel heat sink with the bottom surface of the heat sink modified with micro-diamond knurls have been experimentally investigated. Two knurling heights (0.25 mm and 0.17 mm) were investigated and compared with the bare surface (BS) microchannel heat sink. The details of the experimental investigation and the analysis of the results are reported in detail as follows.

The purpose of this study is to improve the heat transfer performance of a microchannel heat sink in the single-phase flow regime by introducing continuous diamond-shaped knurling on the bottom surface of the microchannel heat sink. Figure 4.1 (a) and (b) show the schematic of the smooth and knurled microchannel along with their substrate. In order to analyze the effect of the knurling height on the flow field and heat transfer, two different knurling heights (a higher height denoted as R-1 and a lower height denoted as R-2) were designed, fabricated, tested, and compared with the BS microchannel heat sinks.

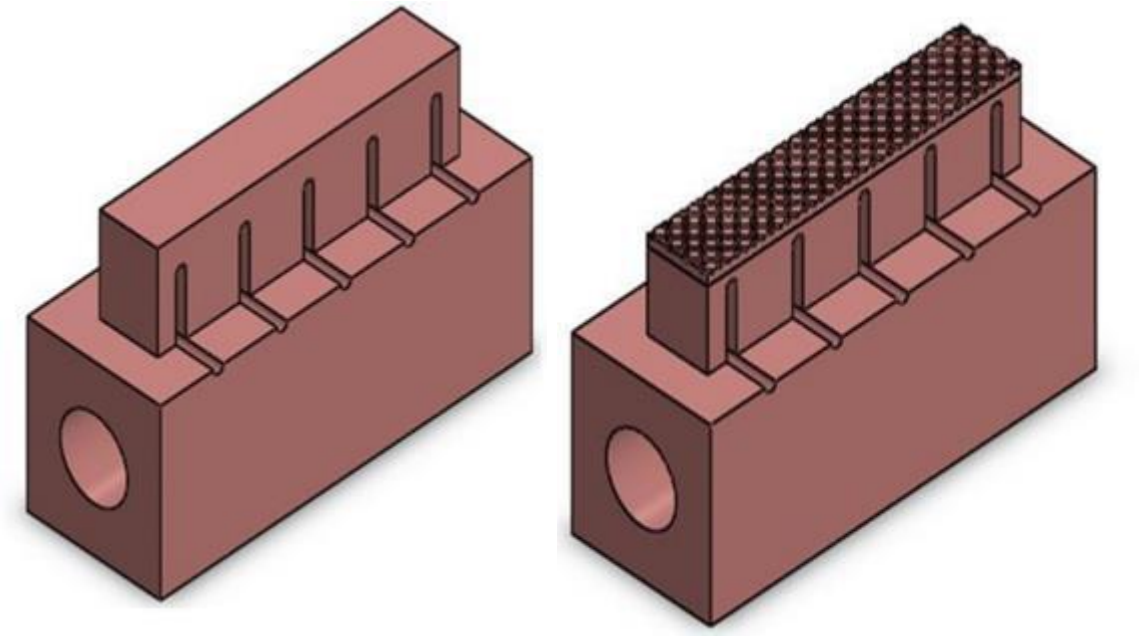

(a) (b)

Figure 4.1 (a) Smooth microchannel heat sink with the substrate; (b) Knurled microchannel heat sink with the substrate.

The bottom surface of the channel was first mechanically polished by using sandpapers with grades of 400, 600, 800, and 1500, respectively. Then, the channel was rinsed with acetone, ethanol, and de-ionized water sequentially followed by a drying process with a nitrogen stream [84][93]. To prepare the knurled patterns on the BS of the microchannel, a coarse knurling tool was used in a modified lathe machine. The heights of the diamond-shaped knurlings were 0.25 mm (R-1) and 0.17 mm (R-2) respectively. The pitch of the knurling for both surfaces was 1 mm and the angle of corrugation for each diamond was kept at 45 degrees. Then, the knurled substrates were assembled into the test section, respectively, for the experiments.

4.1.2 Analysis of the Single Micro-Channel Test Module with Knurling

4.1.2.1Thermal Performance Results

Figure 4.2 shows the average Nu as a function of Re for the knurled microchannel heat sinks and the comparison with the bare surface. The results show significantly enhanced heat transfer performance in terms of Nu for all Re for both of the diamond knurled roughened surfaces (R-1 and R-2), especially for the high roughness (R-1) case. For both cases, i.e., R-1 and R-2, the average Nu increases with the increasing Reynolds number. As shown in the figure, the improvement of the heat transfer for the high roughness (R-1) case is much larger than that for the low roughness (R-2) case, due to the breakup and regeneration of the boundary layer as well as the enhanced mixing of hot and cold water near the rough surface. The largest enhancement for the high roughness case (R-1) is around 255% at Re =500 compared to the smooth microchannel. For the small roughness case (R-2), the largest improvement of Nu is around 68 % at Re = 500 compared to the smooth microchannel case (BS). In addition, the 2.55 times heat transfer enhancement (at Re = 500) for knurled microchannel R-1 is comparable, in most cases, to that of the straight fin microchannels tested or simulated in literature [92][94].

Figure 4.3 compares the local temperatures at the bottom surface of the microchannel heat sinks for the three cases, namely R-1, R-2, and BS, under the same heating power input of 18.86 W and Re = 126.76. As shown in the figure, the high knurl roughness (R-1) case significantly reduces the heat sink temperature by around 16 °C compared to the smooth channel case (BS), due to its largely improved thermal performance. For the low knurl roughness (R-2) case, around 6 °C of reduction in the heat sink surface temperature is achieved compared to the smooth channel case (BS). For both

R-1 and R-2 cases, it clearly shows the heat transfer enhancement effect of the diamond-knurled surface modification.

4.1.2.2Pressure Drop Results

Figure 4.4 compares the pressure drop across the microchannel heat sink for the three cases, respectively, at different Reynolds numbers. Clearly, the pressure drops increase for both the R-1 and R-2 cases compared to the BS case. This is expected since the introduced surface roughness by the diamond knurling changes the friction factors of the channel flow, where the rougher the surface, the higher the pressure drop. At Reynold number of 500, the observed largest pressure drop increases are around 360% and 100% for the high roughness case (R-1) and the low roughness case (R-2), respectively, compared to the smooth channel case (BS). The pressure drop penalties of the knurled microchannel are also comparable to that of the straight fin microchannels tested [92].

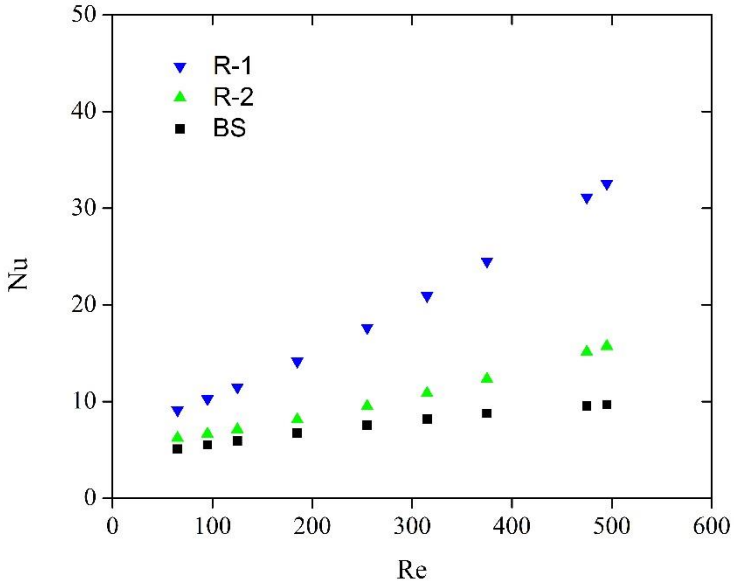

Figure 4.2 Experimental result of Nu as a function of Re for BS, R-1, and R-2.

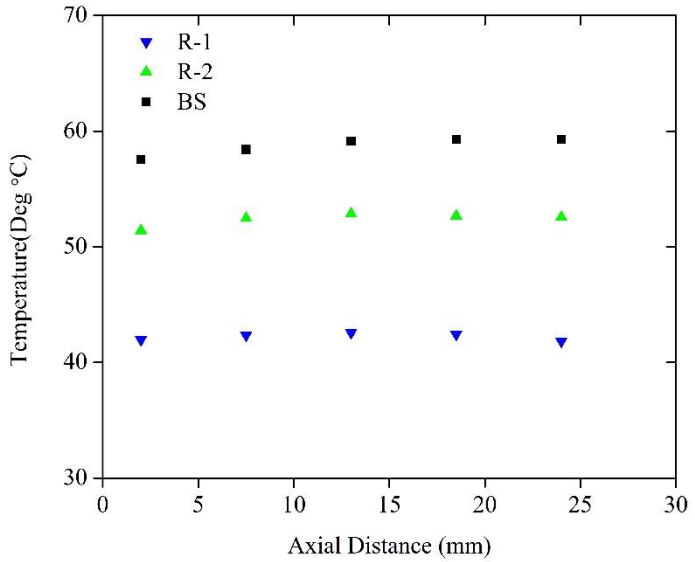

Figure 4.3 Temperature distribution along the channel length for BS, R-1, and R-2 at an input power of 18.86 W and Re= 126.76.

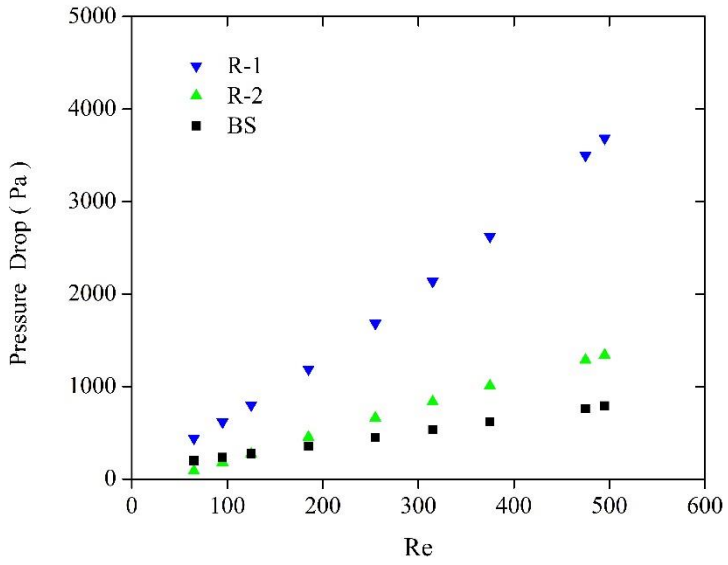

Figure 4.4 Pressure drop vs. Re for the three different surfaces R-1, R-2, and BS.

4.2 **Characterizing Micro-Channel Sandblasting**

Heat transfer performance and pressure drop of single-phase flow through sandblasting modified copper microchannel heat sinks were experimentally investigated and reported in this section. Different kinds of micro-sandblasting patterns were designed to modify the bottom surface of the microchannel heat sink, aiming to enhance the hydrophilic characteristics of the surface. The effects of micro-sandblasting patterns on the thermohydraulic performance of the microchannel heat sinks were evaluated at various Reynolds numbers.

4.2.1 Sample Design

The purpose of this study is to improve the heat transfer performance of a microchannel heat sink in a single-phase flow regime by interrupting the thermal and hydraulic boundary layer by changing the surface roughness by introducing the sandblasting on the bottom surface of the microchannel heat sink. Figure 4.5shows the schematic of the substrate with the top surface sandblasted with elliptical patterns. Each ellipse has an aspect ratio of 2.0. Inside each ellipse, the surface becomes roughened due to some material is removed by sandblasting. Therefore, the rough elliptical regions were surrounded by smooth regions. The total area of the roughened region is 37 % of the top surface area of the heat sink substrate. This sandblasting pattern is a hybrid with smooth and roughened regions, and therefore is denoted as HSEP.

In this study, microchannel heat sinks with HSEPs were designed, fabricated, tested, and compared with FS and BS, respectively. The FS surface means the entire top surface of the substrate is sandblasted, thus there will be no smooth regions in contrast to the HSEP design. Table 4.1 shows the key parameters for three surfaces, namely, HSEP, FS, and BS.

During the fabrication process for the HSEP design, the top surface of the substrate was first mechanically polished using sandpapers with grades of 400, 600, 800, and 1500, respectively. Then, the channel was rinsed with acetone, ethanol, and de-ionized water sequentially followed by a drying process using a nitrogen stream. To prepare the patterns for the two regions (elliptical roughness on the smooth surface), the design was carried out using CREO 3.0 software and transferred to the green film using ultraviolet light to expose the patterned mask (IKONICS Imaging - Rapid Mask High Tack). Next, the film was stacked on the channel substrate and subjected to the sandblasting procedure with a 50 μm particle size of Silicon Carbide (SiC). Due to the presence of the ultraviolet light-treated mask, the micro-blast targeted only the designated ellipse regions. Following this procedure, the mask was removed, and the substrate was rinsed and dried with compressed air. Thereby, the substrate with smooth and rough regions was prepared for the experiment. The fabrication of the FS substrate followed the same procedure as that of the HSEP design, except that the patterned mask was not used during the process.

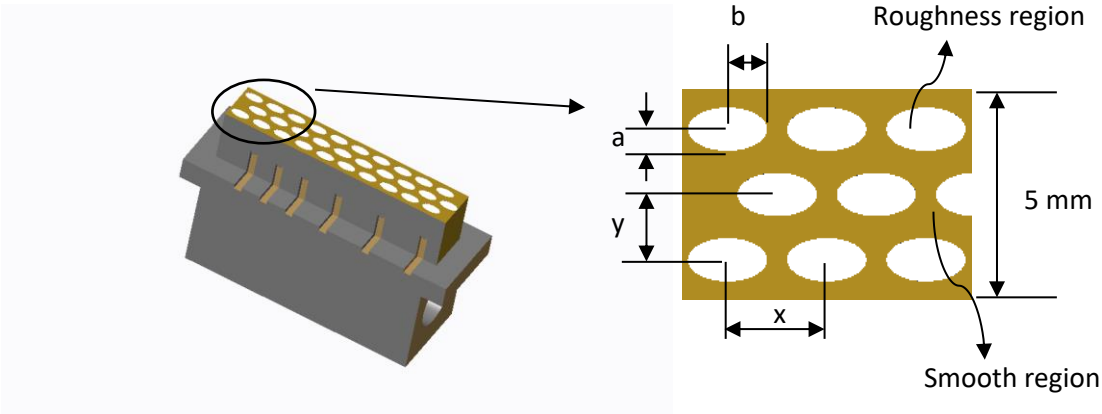

Figure 4.5 Surface design with two regions: smooth and rough

Table 4.1 Parameters of the surfaces

Sample	Aspect ratio (b/a)	Area ratio between the sandblasted area and the top surface of the substrate (%)	Horizontal Pitches(x)	Vertical Pitches(y)
HSEP	2.0	37.0	2.5 mm	1.5 mm
FS	-	100.0	-	-
BS	-	Smooth	-	-

4.2.2 Analysis for the Single Micro-Channel Test Module for Sandblasting

4.2.2.1The effects of hybrid sandblasting of elliptical patterns surface

The effects of hybrid sandblasting of HSEP and FS surfaces on the average Nu as a function of Re are compared with the BS case, as presented in Figure 4.6. As shown in the figure, the HSEP microchannel shows significantly higher Nu than that for the FS and BS micro-channels for the same Re. The increase of average Nu for the HSEP microchannel is around 11.1% -14.4% when Re increases from 85 to 650. The fully sandblasted (FS) microchannel also exhibits higher Nu than that for the BS microchannel, but the enhancement is smaller in comparison to that of the HSEP microchannel. In the case of HSEP, the irregular boundary layer disturbance enhances the local turbulence and thus increases the thermal performance of the microchannel. For FS surface, the average Nu value is increased by 9.55% at Re = 85; whereas at Re = 650, the average Nu is increased by only 2.5%.

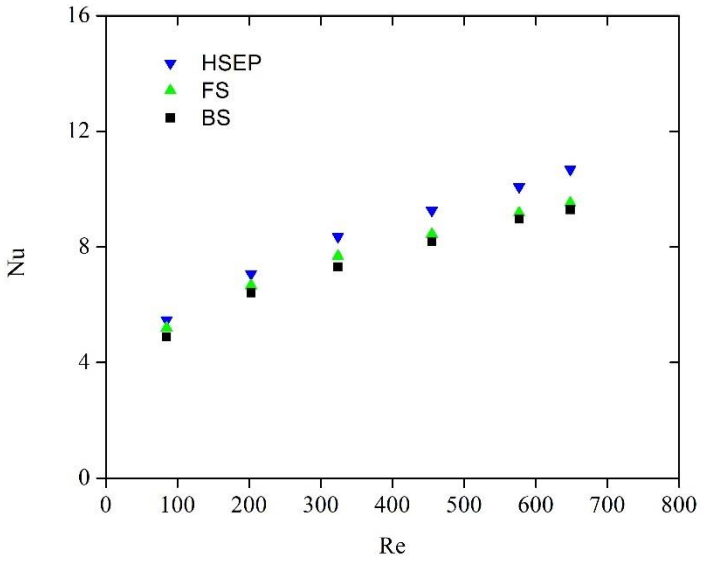

Figure 4.6 Experimental comparison of Nu among BS, HSEP, and FS at different Re values.

Figure 4.7 shows the comparison of the average HTC of HSEP, FS, and BS at differing values of Re. From this figure, it is evident that when Re increases, the average HTC also increases almost linearly for all of cases. Again, it is illustrated that the HSEP microchannel heat sink gives better thermal performance than that of the FS and BS microchannels.

The temperature distribution for HSEP and BS along the channel length is shown in Figure 4.8. It illustrates that the local surface temperatures for HSEP are reduced by 1.57 ℃ at the inlet and by 1.17 ℃ at the outlet, respectively, compared to the BS case. In the case of HSEP, the hybrid surface sandblasting introduces some disruption in the thermal and hydraulic boundary layers, which increases the heat transfer performance and consequently reduces the surface temperature.

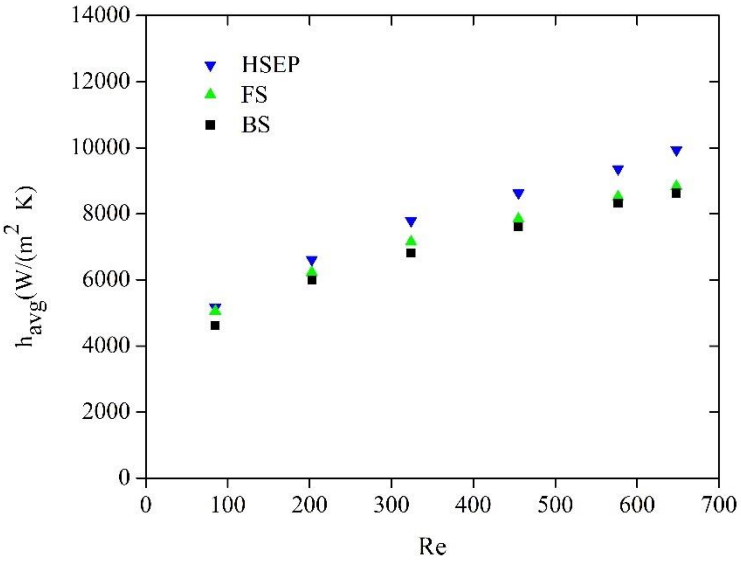

Figure 4.7 Experimental result of convection HTC for BS, HSEP, and FS.

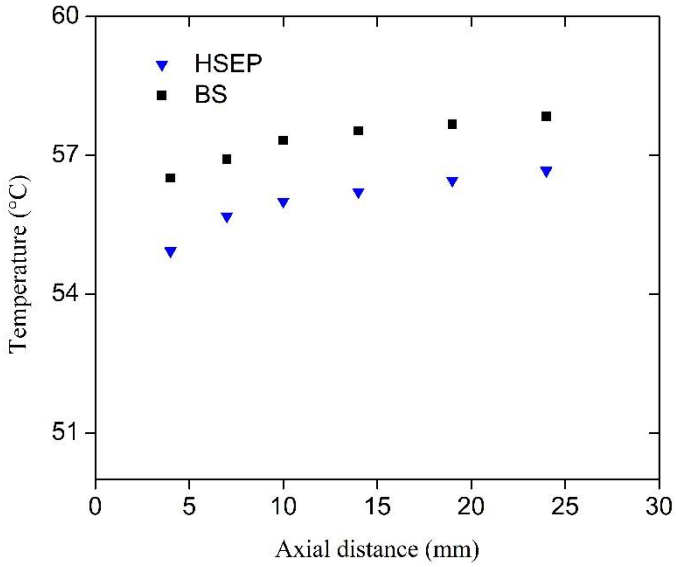

Figure 4.8 Temperature distributions along the channel length for BS and HSEP.

4.2.2.2Pressure Drop Results

Figure 4.9 shows the results of pressure drop for the three surfaces: BS, FS, and HSEP at different Reynolds numbers. Compared to BS, the maximum pressure drop increment for HSEP are around 16% at Re = 85, and around 8.75% at Re = 650, respectively. The pressure drop increase for HSEP is mainly due to the introduced surface roughness of the hybrid sandblasting patterns. For the FS surface, the pressure drop decreases compared to the BS when Re < 450. The reason is that, during the sandblasting process, some material was removed from the BS of the microchannel. As a result, the height of the channel increases, which leads to pressure drop decreases. But meanwhile, the fully sandblasting increases the surface roughness, which in turn increases the pressure drop at a higher Reynolds number.

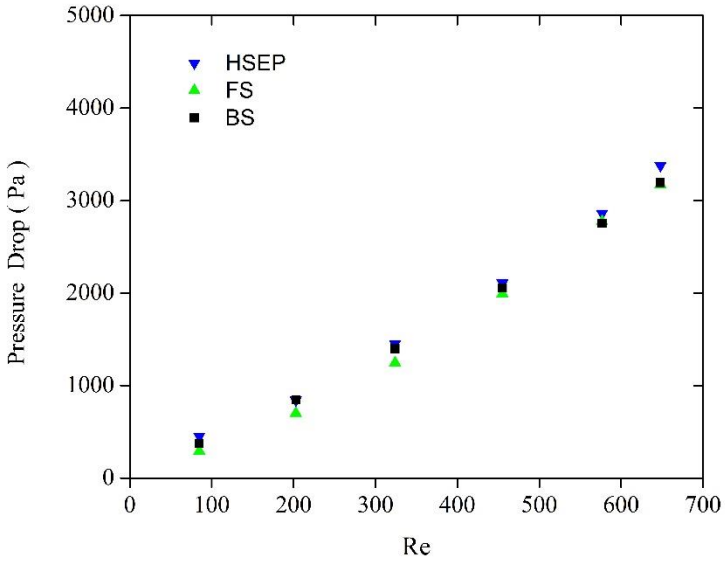

Figure 4.9 Pressure drop Vs. Re for three different surfaces.

4.3 **Summary**

The aim of the above two studies is to experimentally investigate the heat transfer performance of a microchannel heat sink in a single-phase flow regime by changing the surface roughness via two kinds of surface modification techniques.

Diamond diamond-shaped knurling on the bottom surface of the microchannel heat sink is used as the first technique. The thermal performance of the diamond knurling with high roughness (R-1) and low roughness (R-2) is compared with that of a smooth microchannel in terms of average Nu and pressure drops. It can be concluded that both the R-1 and R-2 microchannel heat sinks give better thermal performance than the BS microchannel heat sink. For the test range, the largest enhancement of thermal performance in terms of average Nu for the R-1 and R-2 cases are found to be around 255% and 68% respectively for Reynold number at 500, compared with the BS case. It can be seen that both the R-1 and R-2 microchannel heat sinks show better heat transfer performance at any Re because of the disruption of the hydraulic and thermal boundary layer of the microchannel flow. The thermal performance of R-1 has a much better thermal performance comparing with BS. However, this thermal improvement is accompanied by a higher pressure drop penalty. The highest pressure drop for the R-1 case is around 360% (and 99% for the R-2 case) compared with the BS case for Reynolds number at 500. Nevertheless, this study shows that knurled surfaces are very effective approaches in single-phase microchannel heat transfer, and the height of the knurled surface roughness is an important parameter of the enhancement. The effects of other parameters such as the diamond knurling pitch and angle need to be further investigated in future work The second technique is to introduce surface roughness on the bottom surface of the microchannel heat

sink through sandblasting. The thermal performances, in terms of average Nu and pressure drops, of the FS microchannel and HSEP microchannel have been quantified and compared with that of a smooth microchannel (BS). It can be concluded that the HSEP microchannel heat sink gives better thermal performance than the FS microchannel heat sink. For the test range, the enhancement in terms of average Nu is around 11% ~ 14% for Reynold number from 85 to 650. Moreover, compared to the BS microchannel heat sink, HSEP and FS microchannel heat sinks show better heat transfer performance at any Re because of disruption of the hydraulic and thermal boundary layers. Furthermore, the FS microchannel heat sink enhances the heat transfer rate by 9.55% at Re = 85; but at higher Re, the enhancement is reduced to 2.5%. The HSEP microchannel heat sink increases the pressure drop by around 10.87% for Re in the range from 85 to 650, whereas the FS microchannel heat sink increases the pressure drop by around 9% for Re between 450 and 650.

CHAPTER 5

THE EFFECTS OF MULTIPLE IRS ON FLOW BOILING INSTABILITIES AND CHF FOR TWO-PHASE MICROCHANNEL FLOW

This study experimentally investigated the effects of various configurations of IRs (IRs) on the thermal/hydraulic performance of flow boiling in a rectangular microchannel with an aspect ratio of 13.12, and a hydraulic diameter of 708 μm. The experiments were carried out using a microchannel with three designs of IRs: one-slot opening (1IR), three-slot openings (3IR) and five-slot openings (5IR), and with three different mass fluxes of 32.68, 81.29 and 144 kg/m2s, respectively. As expected, microchannels with IRs exhibit higher pressure drop penalties. Importantly, this study revealed the optimal design for a microchannel with IRs, which is dependent on the operational parameters (e.g., mass flux and heat flux) of the two-phase microchannel heat sink. Furthermore, a parametric study on the area ratio of the IR with opening of 4.2 %, 6.58%, 8.57%, 9.32%, 12.86 %, 15.5 % on two-phase microchannel heat transfer was also performed. The results illustrated an area ratio of 8.57% is the optimal design for all ranges of mass fluxes being tested.

5.1 Using Large Aspect Ratio Microchannel to Cool Electronic Devices

In this work, a single, high aspect ratio microchannel, namely, a microgap, is used to study the effect of multi-IRs. Microgap cooling has many industrial and military applications. For example, it is used for emerging 3-D integrated circuitry thermal

management. This approach utilizes the microgap between chips in three-dimensional stacks as the cooling channel, which is a promising "embedded" cooling strategy [83]. Those gaps typically have the dimensions of 1 cm wide, with channel height in the range of 100 to 500 μm [83]. However, two-phase flow boiling instabilities in the microgap remains a critical issue due to the early presentation of CHF. This is one of the main reasons that this work utilizes a microgap configuration.

5.2 Test Section Fabrication and Experimental Procedure

The test section is presented in Figure 5.1 and consists of seven parts: (1) a transparent cover plate (polycarbonate plastic); (2) a housing block (G-7 fiberglass); (3) the copper test section; (4) a cartridge heater (100 W); (5) an insulation block (G-7 fiberglass); (6) a bottom plate (polycarbonate plastic); and (7) a rubber O-Ring, which is located at the interface between the cover plate and the top surface of the housing and is used to avoid leakage; and (8) an IR.

The cover plate was made from transparent LEXAN 9034, which has a heat deflection temperature of 138 ℃ at 455 kPa. The housing was made from high temperature G-7 fiberglass. The central part of the housing was cut so that the heat sink could be inserted. A cross-sectional view of the assembled test module is shown in Figure 5.1. The protruding portion of the heat sink ensured the designed height of the microchannel. RTV silicon rubber was applied along the interface between the housing and the heat sink to prevent leakage. After the heat sink was in place, the IR was inserted into the shallow portion of inlet plenum of the housing, right before the inlet of the heat sink. Then the top cover plate, housing, and the bottom support plate were bolted together to finish the assembly. A single rectangular microchannel was formed during assembly from the gap between the top

surface of the copper heat sink and the bottom surface of the cover plate. The dimension of the microchannel was measured as 26 mm (L) x 5 mm (W) x 0.381 mm (H), which gave a hydraulic diameter of 708 μm. Two absolute pressure transducers (Omega PX 319) were connected to the deep portion of the inlet and outlet plenums via pressure ports and we used to measure the inlet and outlet pressures, respectively. Moreover, a differential pressure transducer (PX2300-5BDI) was used to directly measure the pressure drop between the inlet and outlet plenums. Two type-K thermocouples were placed in the deep portion of the plenums in the housing to measure the channel inlet and outlet water temperatures. The design of the heat sink and the IR is described in detail in the following sections, 5.3 and 5.4, respectively.

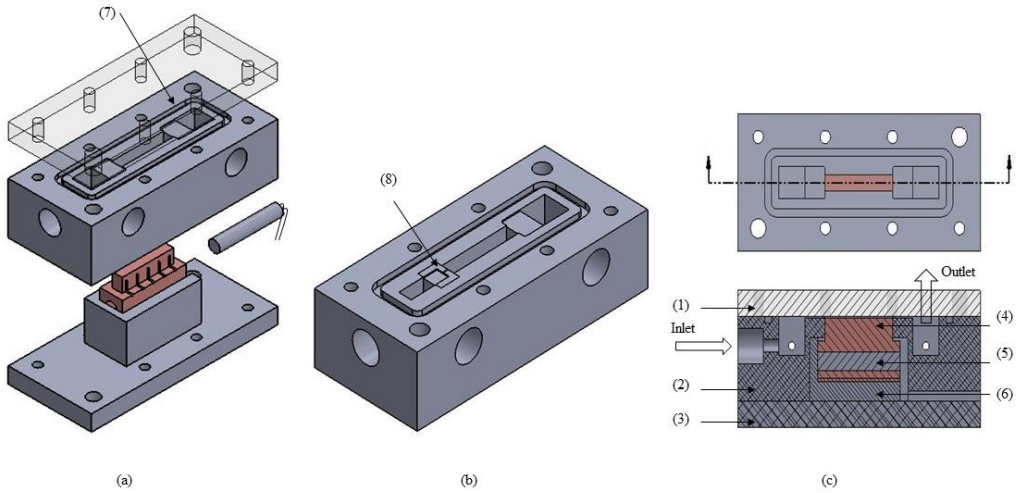

Figure 5.1 (a) Assembled and exploded view, (b) Assembled, and (c) Cross-sectional view of the test section. 1, a transparent cover plate (polycarbonate plastic, model number). 2, a housing block (G-7 fiberglass). 3, a bottom plate (polycarbonate plastic). 4, the copper test section. 5, a cartridge heater. 6, an insulation block (G-7 fiberglass). (7) a rubber O-Ring. (8) an IR.

5.3 **Heat Sink Fabrication and Thermocouple Arrangement**

The heat sink was machined from an oxygen-free (Cu 101) copper block using a CNC Machine. The thermal conductivity of the copper is 391 W/mK. The top surface of the heat sink is a flat surface with a dimension of 26 mm (L) x 5 mm (W). A single microchannel is formed during assembly between the top surface of the heat sink and the bottom surface of the cover plate Figure 5.2. Eight holes, with a diameter of 0.85 mm and a depth of 2.5 mm each, were drilled into the sidewall of the copper block at 2.1 mm below the top surface, to accommodate the thermocouples Figure 5.2. K-type thermocouples were employed to measure the wall temperatures. The eight thermocouples were arranged into two rows: the first row comprises five thermocouples, denoted as T_1 through T_5; and the second row comprises three thermocouples, denoted as T_6, T_7 and T_8, respectively. The vertical location of the first row is at 2.1 mm below the top surface of the cooper block, and the second row is at 4.5 mm below the first row. As shown in Figure 5.2, the horizontal location from the inlet of the microchannel for the thermocouples T_1 through T_5, are at 2 mm, 7.5 mm, 13 mm, 18.5 mm, and 24 mm, respectively; and the horizontal location of the thermocouples T_6, T_7 and T_8 in the second row are at 7.5 mm, 13 mm and 18.5 mm.

Below the thermocouple holes, a small protruding platform was machined around the periphery of the heat sink to both facilitate accurate positioning of the heat sink in the housing and ensure an adequate area for sealing. Below the platform, a 6.35 mm diameter through hole was drilled along the length of the copper block to accommodate the cartridge heater. The resistive cartridge heater was powered by an AC power supply and provided a constant heat flux to the copper block. The power supplied to the cartridge heater was calculated using the voltage and current readings.

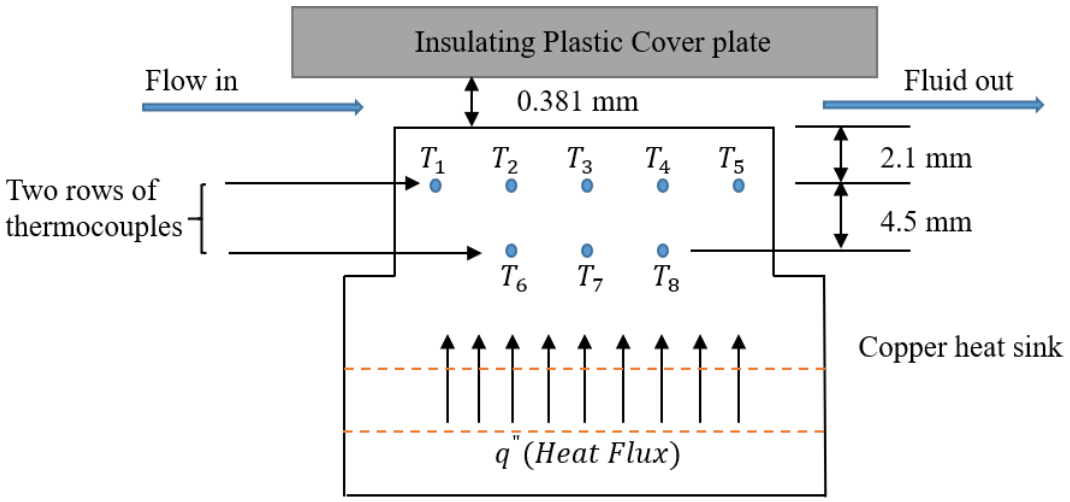

Figure 5.2 Test section and arrangement of thermocouples [82].

5.4 **Configuration of IRs**

A schematic of the configuration of microchannel with IRs is shown in Figure 5.3. The dimensions of the microchannel and the IRs are listed in Table 5.1. The IR is a rectangular block with slot openings to allow for water flow through. It is installed at the entrance of the microchannel during assembly. The restrictor block was made of polycarbonate plastic with a size of 2 mm (L_{IR}) x 5 mm (W) x 0.381 mm (H). Each of the slot openings is 0.25 mm wide (W_{IR}) and 0.35 mm deep (H_{IR}). In this work, the following three configurations of the IR are investigated: (i) with only one slot opening located at the middle of the IR, denoted as "1IR"; (ii) with three slot openings on the IR, denoted as "3IR"; and (iii) with five slot openings evenly distributed on the IR, denoted as "5IR" (Figure 5.3). Also, for comparison, a special case denoted as "0IR" is also included in Table 5.1 and Figure 5.3 which correspond to a configuration with the microchannel only, i.e., without any IR.

The opening ratio is an important indicator used to quantify the effectiveness of an IRs, which is defined as the ratio of the cross-section area of the slot openings to the cross-section area of the microchannel. The values of opening ratios corresponding to the three configurations of 1IR, 3IR and 5IR are 4.59%, 13.77% and 22.95%, respectively, as listed in Table 5.1.

Table 5.1 Dimensions of the microcahnnel with IRs

Device	Number of slot openings	L (mm)	W (mm)	H (μm)	L_{IR} (mm)	W_{IR} (mm)	H_{IR} (μm)	Slot opening ratio
0IR	base case	26	5	381	--	--	--	--
1IR	1	26	5	381	2	0.25	350	4.59 %
3IR	3	26	5	381	2	0.25	350	13.77%
5IR	5	26	5	381	2	0.25	350	22.95 %

5.5 **Flow Visualization System**

A high-speed CCD camera (Phantom v7.3) with a micro-lens was used for flow boiling visualization. At 800 x 600 resolutions, the camera has a maximum frequency of 6688 frames-per-second. To illuminate the microchannel while shooting at higher shutter speed, an external fiber optic light was employed. Data recorded by the flow visualization system was also used to analyze the bubble evolving process.

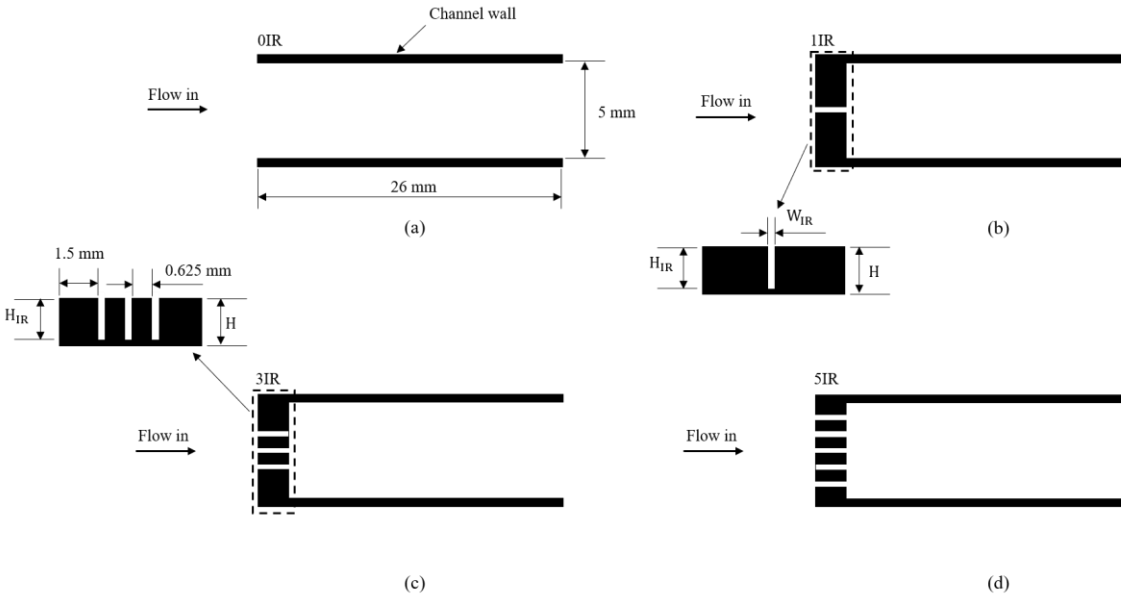

Figure 5.3 Schematic of the microchannel with IRs: (a) 0IR, (b) 1IR, (c) 3IR and (d) 5IR.

5.6 **Experimental Procedure and Data Acquisition**

The following experimental procedure was applied for each test, respectively. Once the test section was assembled, the entire test section, except the water supply tubes, was placed into a foam box to reduce convection and radiation heat losses. The desired constant flow rate for each test run was maintained using a gear pump. The heater power supply was maintained at the required voltage using a variac transformer.

A steady state was typically reached in 90-150 minutes for the test section. Steady state conditions were defined as an average temperature reading of the thermocouples, which remained constant over a fifteen-minute time interval. After the system had reached steady state, the thermocouple readings, the pressure transducer readings, water flow rate, and heating power were recorded for 500 data points each. The recordings were repeated three times for each test with a 5-minute interval between recordings. In addition, at each steady state, the flow boiling process was also recorded for 120 seconds using the high-

speed camera. The temperature and pressure from the thermocouples and pressure transducers were monitored and recorded using a NI Compact DAQ-9721 data acquisition system together with LabVIEW software.

For each test case with the 0IR, 1IR, 3IR, and 5IR IRs, the above procedure was repeated using the same flow rate and the heating power, until the CHF was reached for each the respective cases.

5.7 Results and Discussion

In this section, the experimental results regarding the effects of IRs on the CHF, HTC, and pressure drops (Δp) in the flow boiling microchannel are presented and discussed.

5.7.1 The Effect of IRs on the CHF

Figure 5.4, Figure 5.6, and Figure 5.7 show the effect of IRs on the CHF for three different mass fluxes of 32.68 kg/m^{2}s, 81.29 kg/m^{2}s and 144 kg/m^{2}s, respectively. For all test cases, the inlet water temperature was kept at 30 °C.

The flow boiling characteristics at a low mass flux of G = 32.68 kg/m^{2}s in the microchannel with IRs for cases 0IR, 1IR, 3IR, and 5IR are presented in Figure 5.4. The 5IR case exhibits the highest CHF, followed by the 3IR, 1IR, and 0IR cases. The corresponding CHF values are summarized in Table 5.2.

As shown in Figure 5.4 and Table 5.2, when G = 32.68 kg/m^{2}s, all test cases with IRs show improvement in the CHF of the flow boiling microchannel compared to the 0IR case. This was expected since the IRs function to raise the inlet pressure so that the reverse flow cannot easily extend into the inlet plenum. Thus, the pressure drop fluctuations can be reduced considerably, which leads to partially stabilized flow boiling in the microchannel and a higher CHF.

Table 5.2 The effect of IRs on the CHF at different mass fluxes

Mass flux (kg/m^2s)	CHF (W/cm^2) (data in the parenthesis: relative enhancement over the base case)			
	0IR	1IR	3IR	5IR
G = 32.68	24.95 (base)	28.39 (13.77%)	30.10 (20.62%)	38.06 (52.54%)
G = 81.29	58.87 (base)	59.90 (2.44%)	62.29 (6.53%)	74.53 (27.45%)
G = 144.0	95.52 (base)	113.88 (19.22%)	109.40 (14.53%)	96.12 (0.63%)

The 5IR, 3IR and 1IR cases have enhanced the CHF by 52.53%, 20.62% and 13.76%, respectively compared with the 0IR case. The smaller the slot opening ratio of the IRs, the higher the enhancement should be, in theory, because the pressure at the inlet of the slot openings should be higher to effectively prevent the flow reversal, and thus less severe boiling instabilities. However, this was not the case as illustrated in Figure 5.4, where the 5IR case, which has an opening ratio of 22.95%, shows much higher enhancement in CHF than that of the 3IR and 1IR cases, which have opening ratios of 13.77% and 4.59%, respectively.

This unexpected phenomenon can be explained as follows. For the 1IR case, as shown in Figure 5.5(a), the small opening ratio of 4.59%. physically blocks the bubble expansion into the inlet plenum. The small opening on the inlet restrictor acts as a slot nozzle, which forms continuous jets to drive the microchannel flow. However, as shown in Figure 5.5(a), two large flow circulation zones form in this configuration, where bubbles generated in those zones cannot be easily removed or condensed, causing this test device to reach the CHF much earlier, with only a 13.76% enhancement in the CHF.

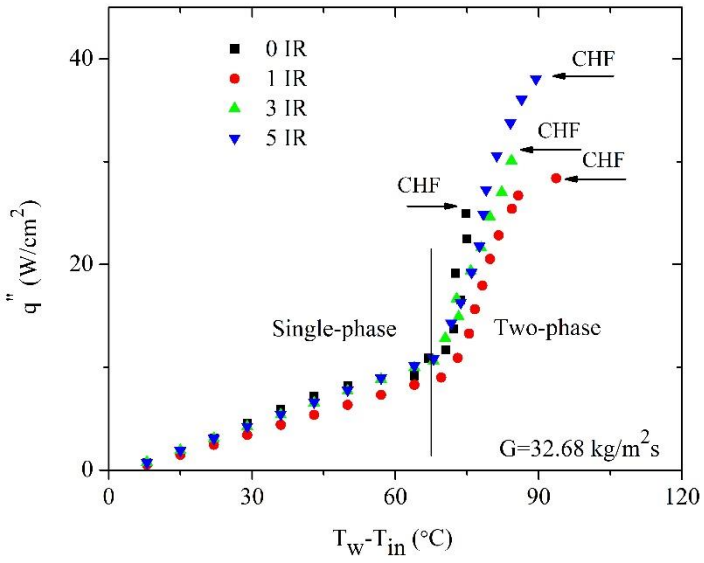

Figure 5.4 The effects of IRs on the CHFs at G = 32.68 kg/m^{2}s.

On the other hand, as shown in Figure 5.5(b), for the 5IR case, there are five jet streams induced into the microchannel by the openings. These evenly distributed jets considerably eliminate the recirculation zones, allowing any bubbles generated in the microchannel to be easily condensed and flushed out. As a result, this configuration leads to the highest CHF enhancement of 52.53%. The CHF enhancement of the 3IR case follows this trend where the value is larger than that of the 1IR case, but smaller than the 5IR case.

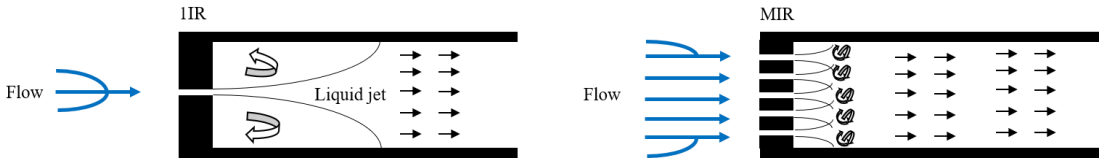

(a) (b)

Figure 5.5 Schematic for (a) 1IR and (b) 5IR cases.

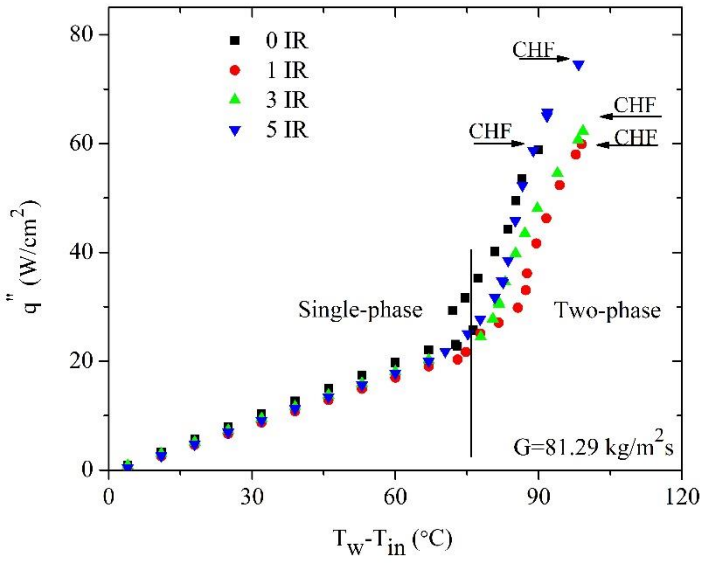

Figure 5.6 The effect of IRs on the CHFs at G = 81.29 kg/m^{2}s.

The flow boiling characteristics at a medium mass flux of G = 81.29 kg/m^{2}s, for the test cases with and without IRs, are depicted in Figure 5.6. All the test cases with IRs displayed an improvement in the CHF compared to the 0IR case. Similar to that of G = 32.68 kg/m^{2}s, the 5IR case shows the highest CHF, followed by the 3IR, 1IR, and 0IR cases. The enhancement in CHF for the 5IR, 3IR and 1IR cases were 27.46%, 6.53% and 2.44%, respectively. Figure 5.7 compares the effect of IRs on the CHFs at a higher mass flux of G = 144 kg/m^{2}s. Again, all the test cases with IRs improved the CHF over that of the base case. However, at higher mass flux, the 1IR case shows the highest CHF, with an enhancement of 19.22% comparing to 0IR case, followed by the 3IR case at 14.53%, and the 5IR case with 0.6%. To better understand the effect of IRs on the CHFs at different mass fluxes, the relative enhancements in CHF were further compared in Figure 5.8, where the y-axis denotes the ratio of CHF to the base case, as defined in Eq. (28).

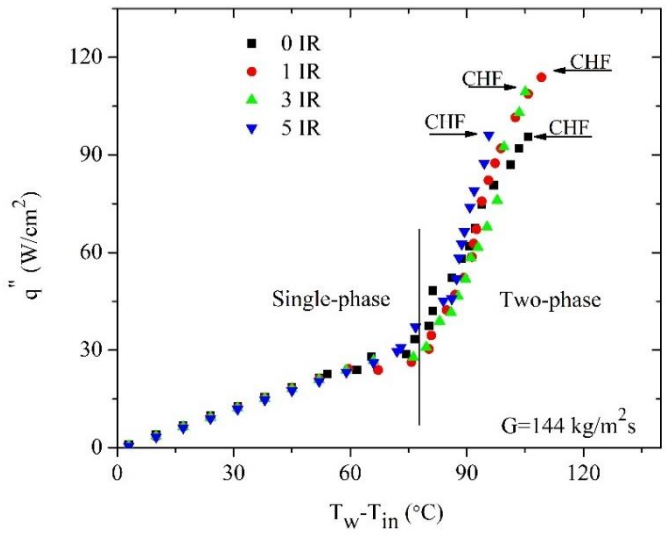

Figure 5.7 the effect of IRs on the CHFs at G = 144 kg/m^{2}s.

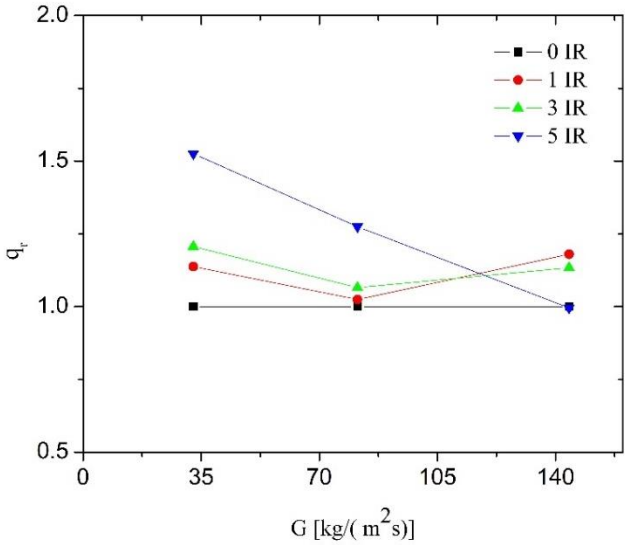

Figure 5.8 Comparison of the CHF enhancements at G = 32.68, 81.29, and 144 kg/m^{2}s.

As shown in Figure 5.8, the CHF performance of the 5IR case linearly decreases with the increase of mass flux. Likewise, CHF performance of the 1IR case first decreases as the mass flux changes from 32.68 to 81.29 kg/m^{2}s, and then increases as the mass flux changes from 81.29 to 144 kg/m^{2}s. The performance of the 3IR case was in-between that

of the 1IR and 5IR cases. The overall CHF performance shown in Figure 5.8 can be explained as follows. When the mass flux increases, the corresponding CHF also increases. As a result, the intensity of flow boiling oscillation increases accordingly. For example, when mass flux increased from G=32.68 kg/m^{2}s to 144 kg/m^{2}s for the 1IR, the corresponding CHF increased from 28.39 W/cm^2, to 59.90 W/cm^2 and to 113.88 W/cm^2, as shown in Table 5.2 for the 1IR case, respectively. This leads to a higher intensity of the flow boiling oscillations as both mass flux and heat flux increase. The multiple jet streams present in the 5IR case work best at lower mass flux to remove the bubbles effectively at the recirculation zones and diminishes as the oscillation becomes stronger. As mass flux and heat flux increase, the large opening ratio of the 5IR case becomes less and less effective.

On the contrary, the smallest opening ratio of the 1IR case becomes more and more effective at suppressing the flow instabilities as mass flux and heat flux increases. Also, as shown in Figure 5.8, the CHF performance for the 1IR case at G = 144 kg/m^{2}s shows the highest CHF enhancement. This occurs because the static pressure head at the inlet of 1IR becomes much higher than that of the 5IR case due to its smaller size, thus it physically blocks the bubbles from bursting into the inlet plenum and largely prevents flow reversal. As a result, the 1IR case achieved the highest CHF at the high mass flux. Further explanations are presented in Section 5.7.2 below. In summary, the CHF performances for the various test cases with IRs depend on the mass flux of the flow boiling microchannel, where multiple IRs provide the best CHF enhancement at low mass flux, and the 1IR case performs best at high mass flux.

5.7.2 Mechanism Analysis of IRs with Flow Visualization and Plots of Water Temperature Fluctuations

In this section, further analysis of the mechanism of multiple IRs on the flow boiling microchannel was performed, with the aid of flow visualizations and plots of water temperature fluctuations at the inlet plenum. Figure 5.9 illustrates the changes of the recirculation zones for the 1IR, 3IR and 5IR cases, respectively. These pictures are obtained from the videos recorded with the high-speed camera system, with the mass flux G=32.68 kg/m^{2}s, and with heat flux q'' around 13.0 W/cm^2.

As shown in Figure 5.9(a), for the 1IR case, large bubbles frequently appear and exist in the two large recirculation zones. This observation confirms the mechanism as illustrated in Figure 5.5(a). For the 3IR case, as shown in Figure 5.9(b), small bubbles frequently appear and continue to exist in the relatively smaller recirculation zones between the openings. For the 5IR case, the recirculating zones become even smaller due to the five slot openings and small bubbles recirculating in these zones are not obvious, as can be seen from Figure 5.9(c).

As mentioned earlier, the other mechanism of using IRs involves physically blocking the bubbles from bursting into the inlet plenum, thereby suppressing flow reversals. This is due to the IRs effectively isolating the upstream compressible volume (e.g., soft tubes, dissolved gas, and trapped air bubble, etc.) from the microchannel, thus increasing the stiffness of the system and suppressing the severe “pressure drop oscillations” type of flow boiling instabilities.

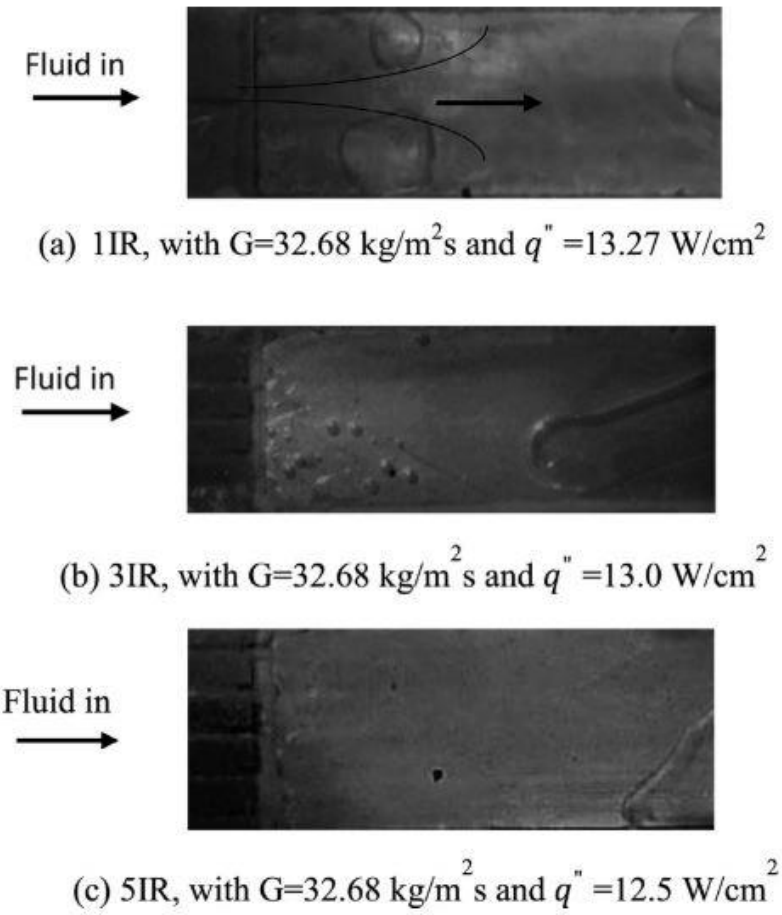

Figure 5.9 Comparison of recirculation zones for (a) 1IR, (b) 3IR and (c) 5IR, with G=32.68 kg/m^{2}s and q$''$ around 13.0 W/cm^2.

As Qu and Mudawar demonstrated in their pioneering work [63], because of the interactions between vapor generation in channels and compressible volume in the flow loop upstream of the heat sink, fairly periodic and large-amplitude flow oscillations will be present in the flow boiling microchannel heat sink. To prevent this type of oscillations, Qu and Mudawar [63] employed a throttling valve before the test section to increase the stiffness of the system. The multiple IRs investigated in this work operate similar to a throttling valve by isolating upstream compressible volumes and increasing the stiffness of

the system. Moreover, integrating multiple IRs directly in front of the microchannel is better than using a throttling valve, as the IRs further isolate the inlet plenum from the channel, thus any potential compressible volumes in the inlet plenum of the heat sink cannot interact with the vapor generation in the channel. As a result, the on-chip IRs can greatly reduce the footprint of the heat sink, compared to the use of throttling valves.

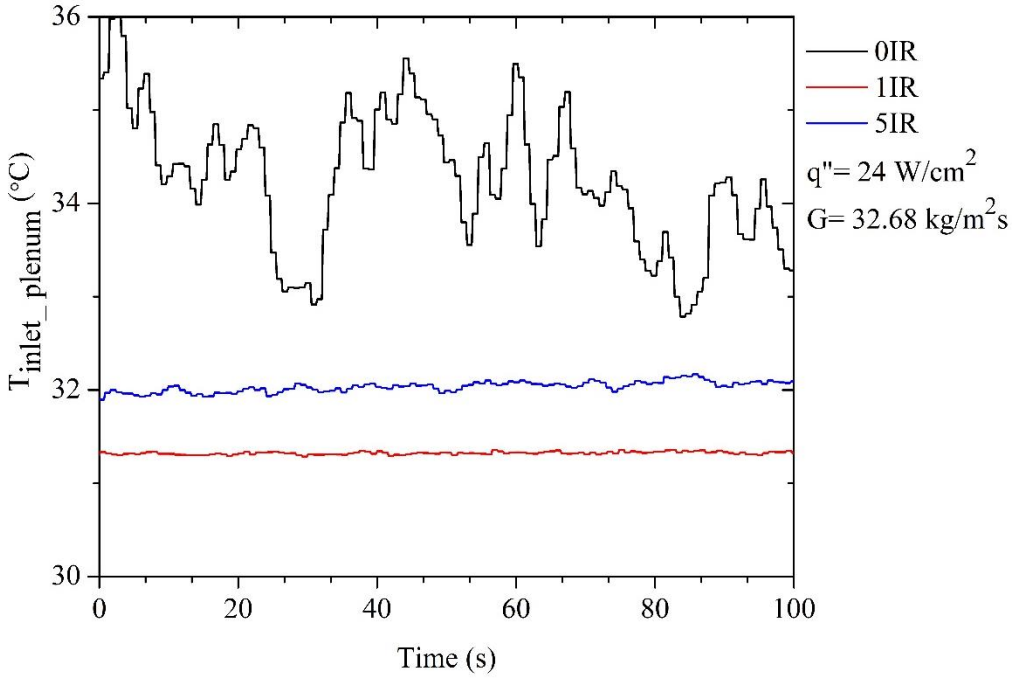

Figure 5.10 Comparison of temperature fluctuations at the inlet plenum for 0IR, 1IR, and 5IR cases, with G = 32.68 kg/m^{2}s and $q^{"}$ around 24.0 W/cm^2.

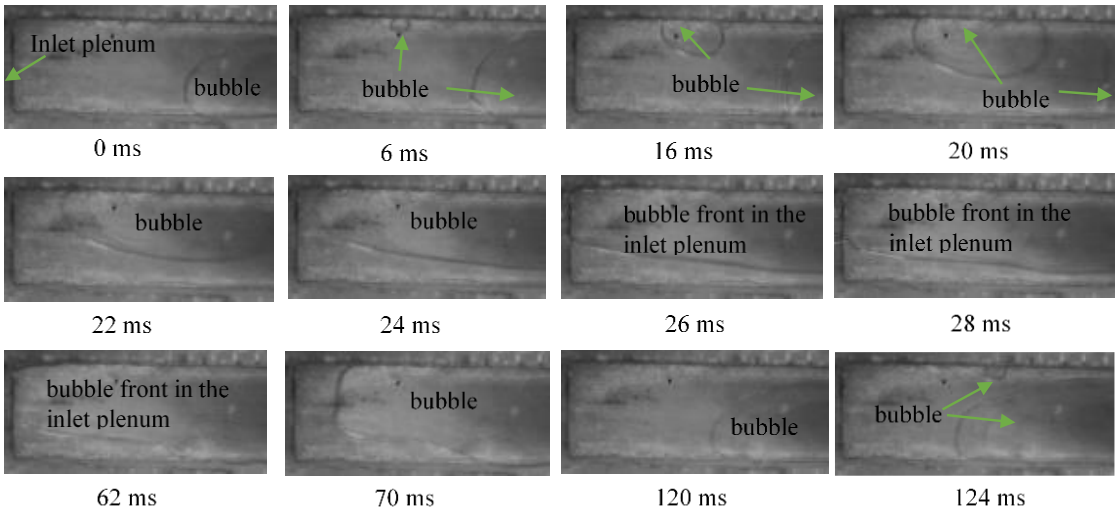

Figure 5.11 Bubble growth and expansion into the inlet plenum, with G = 32.68 kg/m^2 and $q^{"}$ around 22.5 W/cm^2.

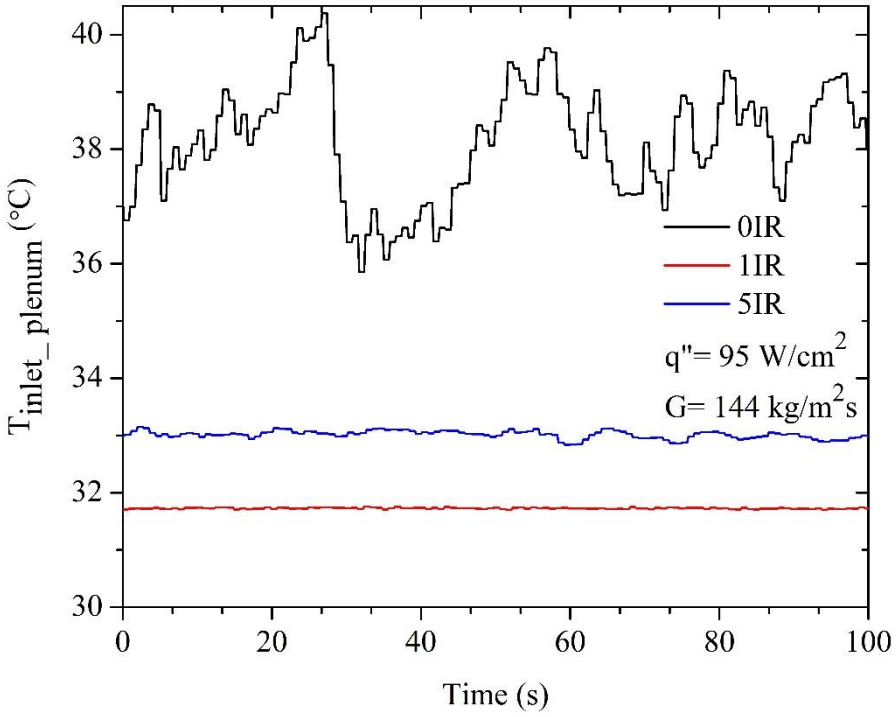

Figure 5.12 Comparison of temperature fluctuations at the inlet plenum for 0IR, 1IR, and 5IR cases, with G = 144 kg/m^{2}s and $q^{"}$ around 95.0 W/cm^2.

Figure 5.10 through Figure 5.12 demonstrate the effects of IRs on preventing back flows. As shown in Figure 5.10, under the same mass flux (G = 32.68 kg/m^2 s) and inlet water temperature (30 °C), and nearly the same heat flux q'' around 24.0 W/cm^2, the 0IR case exhibits fairly large temperature fluctuations compared to the 5IR and 1IR cases. The process of bubble growth and expansion into the inlet plenum is illustrated in Figure 5.11 for the 0IR case. Specifically, at t = 6 ms, a small bubble appears at the upper edge of the channel. From t = 6 ms, it quickly expands both upward and downward and in the transverse direction of the channel. At t = 24 ms, the bubble almost clogs the channel. From t = 26 ms to t = 62 ms, the elongated bubble further penetrated into the inlet plenum, and this process takes around 36 ms. From t = 70 ms to t = 120 ms, the bubble front reappears inside the channel. Finally, another cycle starts at t = 124 ms, which begins from a small bubble appearing at the upper edge of the channel.

It is noteworthy in Figure 5.10, that although the water temperature supplied to the test section is maintained at 30 °C, the average temperatures at the inlet plenum for the 0IR, 5IR and 1IR cases rise to 34 °C, 32 °C and 31.2 °C, respectively. This is caused by the mixing of the hot reverse flow with the inlet water in the inlet plenum. For the 0IR case, intense back flow causes large fluctuations, as well as large mixed temperature (i.e., rising by around 4 °C). For the 5IR case, due to the presence of the IRs, the back flow is largely suppressed, as evidenced from the much smaller fluctuations of the temperature at the inlet plenum. However, some back-flow penetrating through the opening of the 5 IRs causes the mixed temperature in the inlet plenum to rise by around 2 °C. For the 1IR case, the back flow is further suppressed compared to the 5IR case, with a rise of only 1.2 °C.

Figure 5.12 further illustrates the effect of IRs on suppressing the flow boiling instabilities under the flow rate of G = 144 kg/m^{2}s, with heat flux q'' around 95.0 W/cm^2. Similar to that shown in Figure 5.10, the 0IR case in Figure 5.12 also exhibits large temperature fluctuations in the inlet plenum, compared to 1IR and 5IR cases. Additionally, the values of the mixed water temperature for the 0IR, 1IR and 5IR cases rise approximately 8 °C, 1.8 °C and 3 °C, respectively, over the inlet water temperature of 30 °C. Compared with their respective cases in Figure 5.10, larger temperature increases also indicate the increase of flow instabilities.

Both Figure 5.10 and Figure 5.12 illustrate that IRs can effectively suppress the flow boiling instabilities. In terms of preventing back flow, the 1IR case is always better than the 5IR case. This is expected as 1IR case has the smallest opening, while the openings of the 5IR case result in an opening five times larger. However, it should be noted that the contributions on the CHF enhancement with respect to the two mechanisms, namely (i) multiple jet streams, and (ii) preventing back flow, are different depending on the mass flux in the flow boiling channel and the IR configurations. As has been discussed in Section 5.7.1 above, it is the compromise between these two distinct contributions that explains the superior CHF enhancement of the 5IR case at low mass flux versus the 1IR case performance at higher mass flux.

5.7.3 The Effect of IRs on HTC

The effects of the IRs on the heat transfer coefficients (HTC) of the microchannel heatsink are presented and discussed in this subsection. The average HTCs for test cases with and without IRs are plotted and compared in Figure 5.13, Figure 5.14, Figure 5.15,

for mass fluxes of 32.68, 81.29, and 144 kg/m^{2}s, respectively. Again, for all test cases, the inlet water temperature was kept at 30 °C.

Figure 5.13 depicts the change of the average HTC with increasing heat flux, for the 0IR, 1IR and 5IR cases, respectively, at constant mass flux of 32.68 kg/m^{2}s and inlet water temperature of 30 °C. The data for the 3IR case are omitted from the Figure 5.13, Figure 5.14, and Figure 5.15 to improve figure readability, and it should be noted that data for the 3IR case are always intermediate to the 1IR and 5IR cases.

As shown in Figure 5.13, when the heat flux is below 12 W/cm^2, microchannel flow is in the single-phase regime. In this region, the average HTCs are almost constant for all test cases with and without IRs. However, the IRs do slightly lower the average HTCs compared to the base case (i.e., 0IR). This is also observed in Figure 5.4 by comparing slopes in the single-phase region: the slope of the 0IR case is the largest, followed by the 5IR case and finally the 1IR case. This is because the recirculation zones introduced by the IRs unfavorably change the flow and heat transfer performance in the single-phase microchannel, especially for the 1IR case. For heat flux over 15 W/cm^2, flow in the microchannel is in the two-phase regime. Apparently, for the same heat flux, the 0IR case (i.e., without an IR) exhibits the highest average HTC, and all cases with IRs lower the HTC. With IRs, the HTC of the 5IR case is larger than that of the 1IR case. This is again because the recirculation zones introduced by the IRs unfavorably change the flow and heat transfer performance in the two-phase microchannel. At lower mass flux, the 5IR case, with diminished recirculation zones, performs better than the 1IR case.

When the mass flux is increased to 81.29 kg/m^{2}s as shown in Figure 5.14, the HTC performance in the single-phase region for cases with and without IRs are similar to that

shown in Figure 5.13, namely, the 0IR case performs best, followed by the 5IR and 1IR cases.

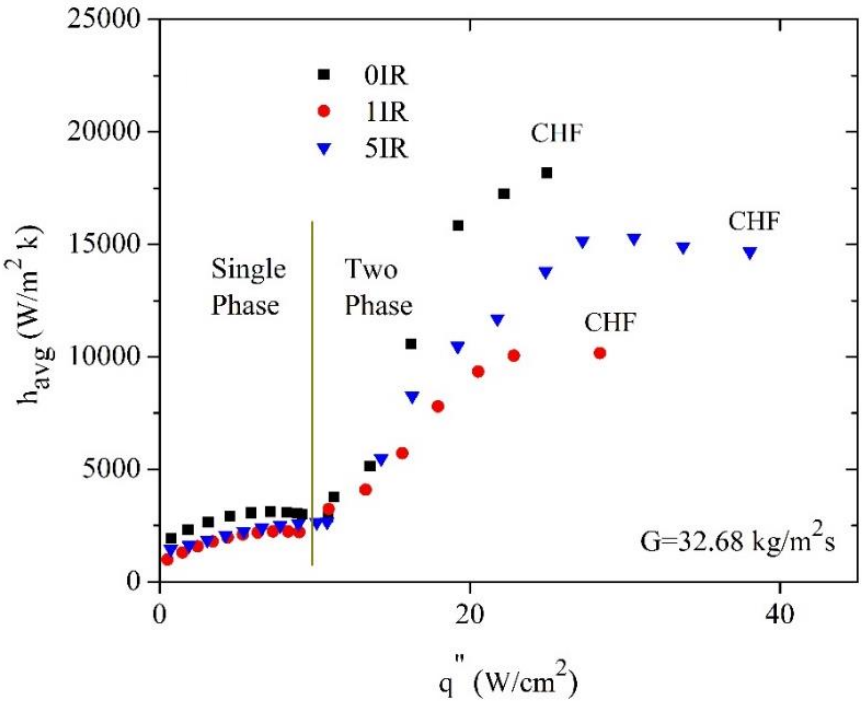

Figure 5.13 The effect of IRs on HTC at G = 32.68 kg/m^{2}s and T_{in} = 30 °C.

This can again be seen from the different slopes in the single-phase region in Figure 5.4. For the two-phase region, unlike the wide spread of HTCs in Figure 5.13, the HTCs for the 0IR, 1IR and 5IR cases are more similar. The HTCs of the 5IR case are almost overlapping with that of the 0IR case, and the HTCs of the 1IR case are slightly lower than that of the 5IR case, indicating that the unfavorable effects of IRs on two-phase HTCs are diminished with increased mass flux.

With further increase of mass flux to 144 kg/m^{2}s Figure 5.17, the HTCs for cases with IRs are almost the same as that of those without IRs in the single-phase region, as confirmed from the overlapped plots in the single-phase region in Figure 5.7, indicating

that IRs have negligible effects on the single-phase microchannel heat transfer performance. This is because the increased flow rates increase the inertia of the flow, leading to increased mixing of the single-phase flow in the recirculation zones.

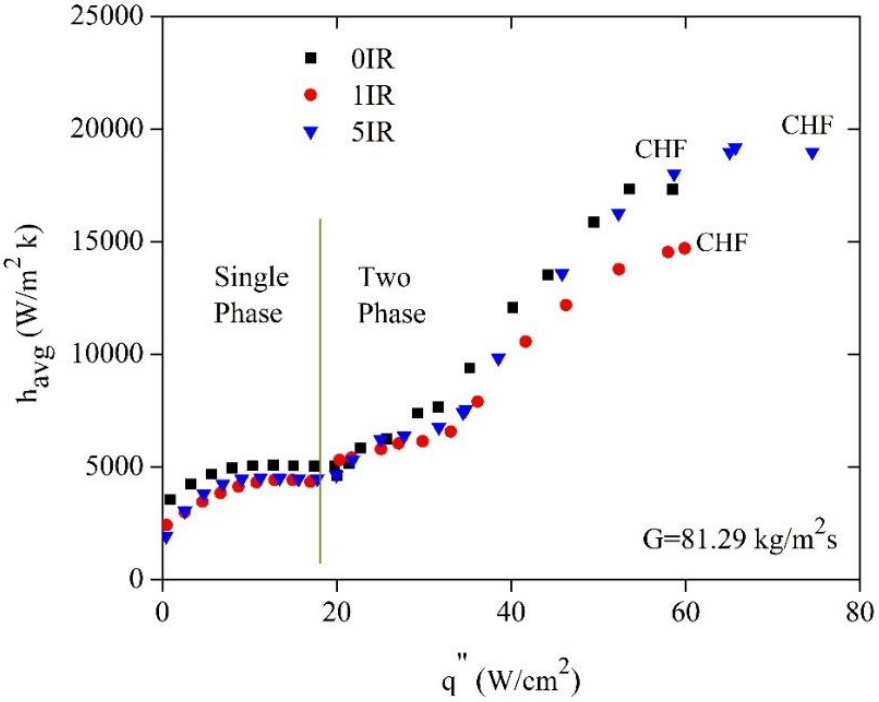

Figure 5.14 The effect of IRs on HTC at G = 81.29 kg/m^{2}s and T_{in} = 30 °C.

For the two-phase region, with heat flux between 30 and 80 W/cm^2, the HTC performance is similar with or without IRs, as data points for 5IR and 1IR cases overlap with that of the 0IR case; however, when the heat flux is over 80 W/cm^2, both the 1IR and 5IR cases show improved HTC over the 0IR case. This finding indicates that, when the microchannel heat sink operates at higher mass and heat flux, the IRs exhibit favorable effects on the flow boiling HTCs. The enhancement of HTCs (for heat flux over 80 W/cm^2) comes from the effects of flow instability suppression by the IRs.

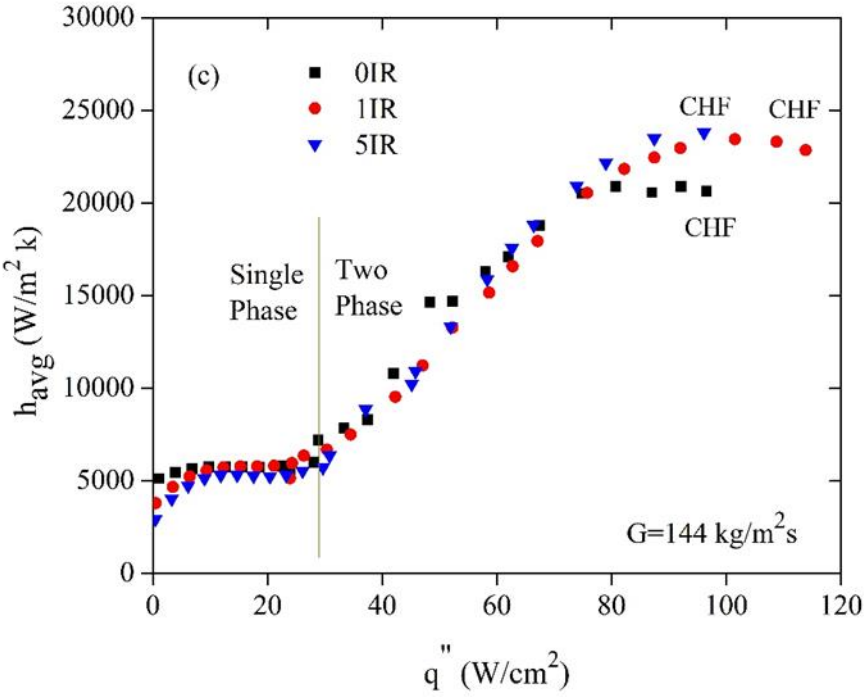

Figure 5.15 The effect of IRs on HTC at G =144 kg/m^{2}s and T_{in} = 30 °C.

5.7.4 The Effect of IRs on Pressure Drop

Employing IRs to suppress the flow boiling hydrodynamic instabilities in the microchannel will inevitably increase the pressure drop across the orifices and the microchannel heat sink. The magnitudes of the pressure drop increase need to be quantified, so that the pressure drop penalties associated with the gain of the CHFs and/or HTCs can be balanced accordingly.

The pressure drops for test cases with and without IRs are compared in Figure 5.16, Figure 5.17, and Figure 5.18 for the mass fluxes of 32.68, 81.29 and 144 kg/m^{2}s, respectively. Likewise, the inlet water temperature for all test cases was kept at 30 °C. The pressure drops across the IRs and the microchannel was computed using equations (29) and (30).

As shown in Figure 5.16 through Figure 5.18, for all three mass fluxes, the pressure drops in the 1IR case are significantly larger than that of other cases, followed by the 3IR, 5IR and 0IR cases, respectively. This is expected since the 1IR case has the smallest opening ratio of around 5%. Surprisingly, even though the 5IR case has an opening ratio of around 23%, the pressure drops for the 5IR case are very close to that of the 0IR case.

The pressure drops as a function of flow rate for cases with and without IRs were further compared in Figure 5.19. Here, the y-axis denotes the ratio of

$$M = \frac{[\Delta p_{mIR+ch}]_{q"=CHF}}{[\Delta p_{0IR}]_{q"=CHF}}, m = 1,3,5 \tag{32}$$

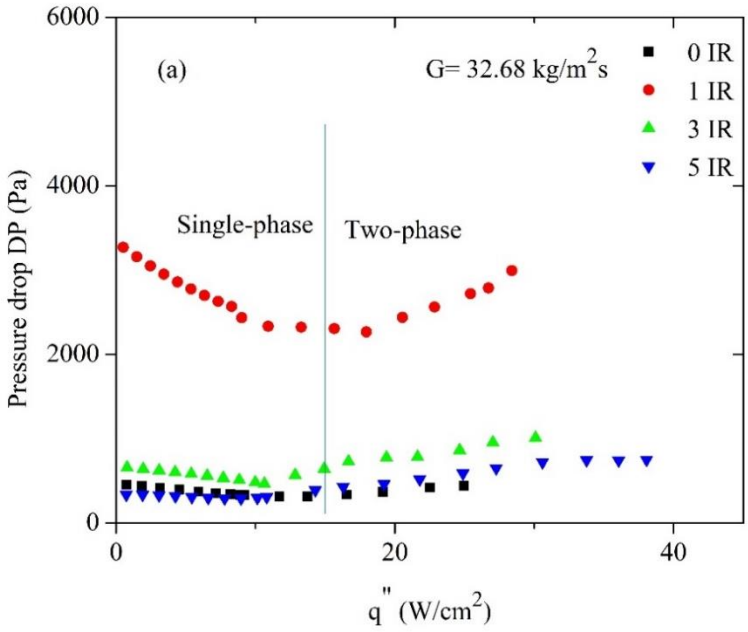

Figure 5.16 The effect of IRs on pressure drops at G = 32.68 kg/m^{2}s and T_{in} = 30 °C.

where the numerator $[\Delta p_{mIR+ch}]_{q"=CHF}$ denotes the pressure drop across both the IRs and the microchannel for the case of 1IR, 3IR and 5IR, respectively, at the CHF of the

respective case; and $[\Delta p_{0IR}]_{q"=CHF}$ denotes the pressure drop across the microchannel only for the 0IR case, at the corresponding CHF under the same flow rate. Thus, M is a measure of the pressure drop penalty, i.e., it denotes increase in pressure drop with IRs at CHF comparing to the base case without IR at CHF.

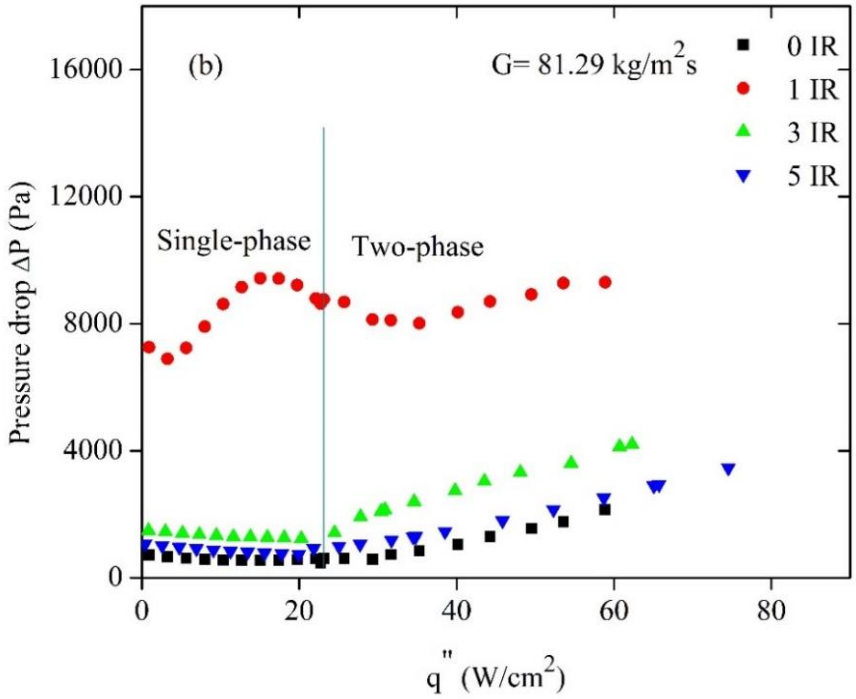

Figure 5.17 The effect of IRs on pressure drops at G = 81.29 kg/m^{2}s and T_{in} = 30 °C.

From Figure 5.19, the 1IR case shows a pressure drop increases by 5.79 times over the 0IR case, at the lower mass flux of G = 32.68 kg/m^{2}s, and to around 4.13 times as the mass flux increases to 81.29 kg/m^{2}s. Further increase the mass flux to 144 kg/m^{2}s, the pressure drop penalty for the 1IR case is increased to nearly five times over the corresponding 0IR case. Similar variations are observed for the pressure drops of the 3IR case as the mass flux increases Figure 5.19. However, pressure drop penalties are

comparatively much smaller than that of the 1IR case. The 5IR case shows the lowest pressure drop penalties, and the pressure drop ratio, M, decreases as the mass flux increases.

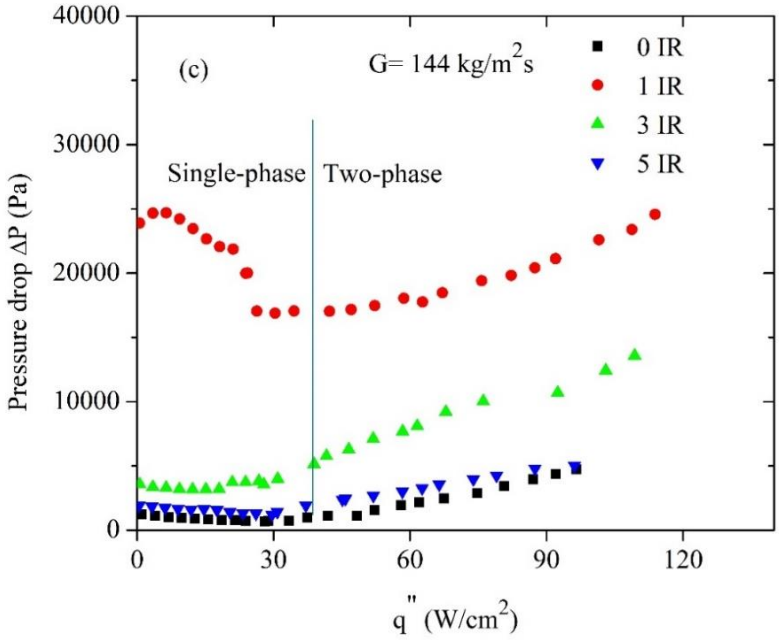

Figure 5.18 The effect of IRs on pressure drops at G =144 kg/m^{2}s and T_{in} = 30 °C.

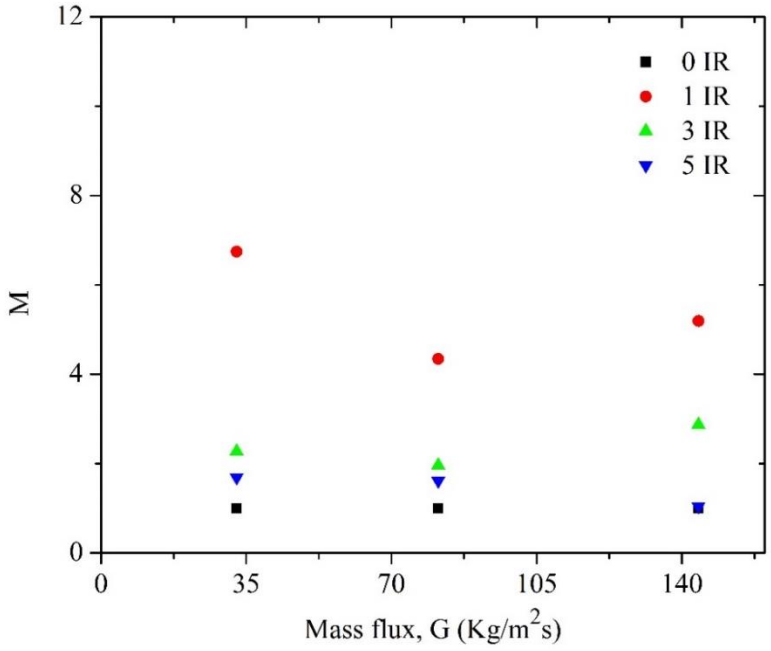

Figure 5.19 The effect of IRs on pressure drops at $q" = CHF$.

Further comparison of the results presented in Figure 5.8 and Figure 5.19 illustrate the gain versus the penalty for the various cases of microchannel with multiple IRs, namely,

$$\frac{q_r}{M} = \frac{gain\ of\ CHF\ enhenacment}{penalty\ of\ pressure\ drop\ increase\ at\ CHF} \tag{33}$$

where q_r and M were defined in Eqs. (28) and (32), respectively. Table 5.3 summarizes the gain over penalty matrix using the measure defined in Eq. (33).

Table 5.3 illustrates that at the lower mass flux of G = 32.68 kg/m^{2}s, the gain of 1.53x CHF enhancement for the 5IR case over the 0IR case (Figure 5.8) was accompanied by a penalty of 1.58x of pressure drop increase over the 0IR case Figure 5.19. The performance ratios listed in bold in Table 5.3 reveal that the 5IR case works the best of all IR cases at both the lower and intermediate mass fluxes. For the highest mass flux, the 3IR case gives the best performance of IR cases. As has been explained earlier, the optimum outcome is the result of combined effects from reduced the recirculation zones (larger blocking area to suppress flow oscillations) and reduced pressure drop penalties.

Table 5.3 Comparison of the gain of CHF enhancements and the penalty of pressure drop increases for the various cases with IRs

Mass flux (kg/m^{2}s)	$\frac{q_r}{M} = \frac{gain\ of\ CHF\ enhenacment}{penalty\ of\ pressure\ drop\ increase\ at\ CHF}$			
	0IR	1IR	3IR	5IR
G = 32.68	1.0 (base)	1.14/5.79	1.21/2.06	1.53/1.58
G = 81.29	1.0 (base)	1.02/4.13	1.07/1.89	1.28/1.57
G = 144.0	1.0 (base)	1.19/5.08	1.15/2.84	1.01/1.05

5.8 Effects of IR Area Ratio on CHF in Microchannels

The work presented in subsection 5.7 focused on enhancing CHF by using multiple inlet restrictors (MIRs) in the microchannel. The results showed that MIRs work beneficially at low mass flux, but MIRs are not a good option for CHF at increased mass flux. However, the 1IR design worked better for high mass fluxes. Therefore, in the following subsections, the study will focus on 1IR cases with different area ratios.

5.9 Configuration of the One IR with Different Area Ratios

Figure 5.20 displays a schematic of the configuration of a microchannel with one inlet restrictor (1IR). The dimensions of the microchannel and the IR are listed in Table 5.1. The 1IR is a rectangular block with one slot opening at the middle to allow water flow through. It is installed at the entrance of the microchannel during assembly. The restrictor block was made of polycarbonate plastic with a size of 2 mm (L_{IR}) x 5 mm (W) x 0.450 mm (H). The width (W_{IR}) of the slot openings can been changed to different sizes between 0.25 mm to 0.921 mm; and the depth of the opening, H_{IR}, is kept at 0.38mm. The ratio between the area of the slot opening to the cross-sectional area of the microchannel is denoted as area ratio (AR). The values of AR can be changed between 4.2% and 15.5% by changing the width of the opening. For comparison, a special case denoted as "0IR" is also included in Table 5.4 and Figure 5.20, corresponding to the design with microchannel only, i.e., without the inlet restrictor.

In total, six different ARs were selected for the parametric study, with values listed in Table 5.4.

Table 5.4 Dimensions of the microchannel with different inlet area ratio restrictors.

Device Description	G(kg/m^{2}s)	L (mm)	W (mm)	H (μm)	L_{IR} (mm)	W_{IR} (mm)	H_{IR} (μm)	Slot opening Ratio $AR = \left(\frac{A_{IR}}{A_{ch}}\right)$
Base case, 0IR	66, 147, 221.65	26	5	450	--	--	--	100%
IR		26	5	450	2	0.25	380	4.2 %
IR		26	5	450	2	0.39	380	6.58 %
IR		26	5	450	2	0.508	380	8.57 %
IR		26	5	450	2	0.635	380	9.32 %
IR		26	5	450	2	0.762	380	12.86 %
IR		26	5	450	2	0.921	380	15.5 %

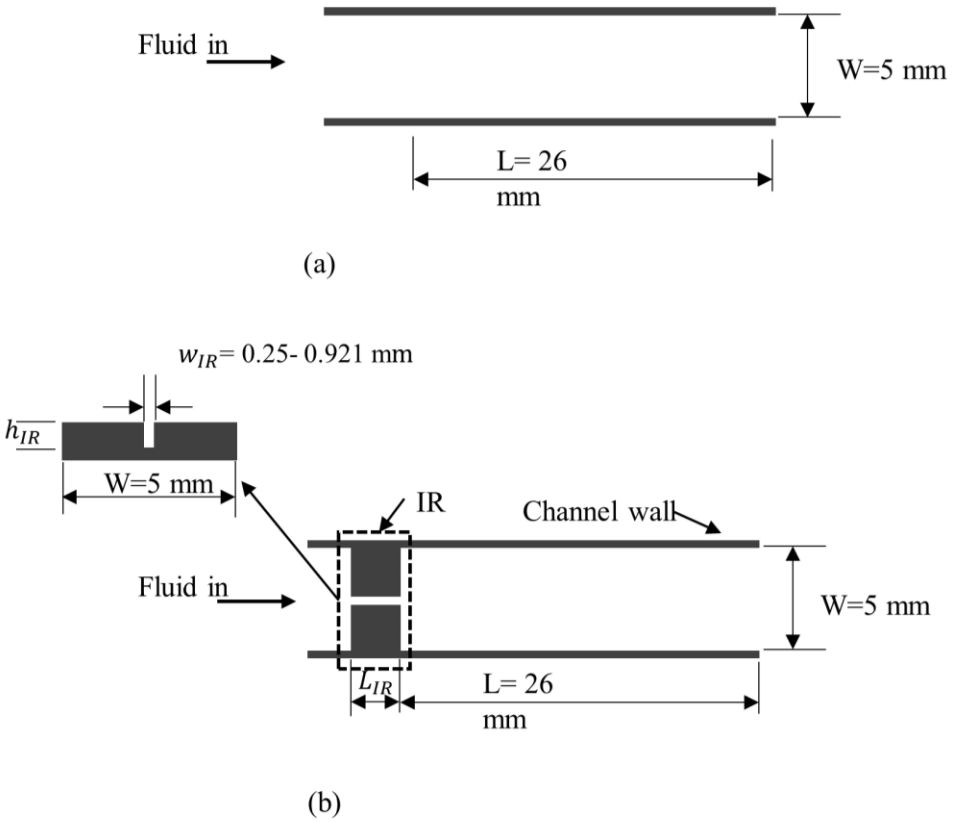

Figure 5.20 Schematic of the microchannel with IR: (a) 0IR and (b) 1IR.

5.10 **Results and Discussion**

In this section, the experimental results for the effects of the area ratios of one IR on the CHF, and pressure drops (Δp) in the flow boiling microchannel are presented and discussed.

5.10.1 The Effect of Area Ratio on the CHF

Figure 5.21 to Figure 5.23 show the boiling curves for the six different area ratios of the IRs at mass fluxes of 66 kg/m^{2}s, 147.76 kg/m^{2}s, and 221.65 kg/m^{2}s, respectively.

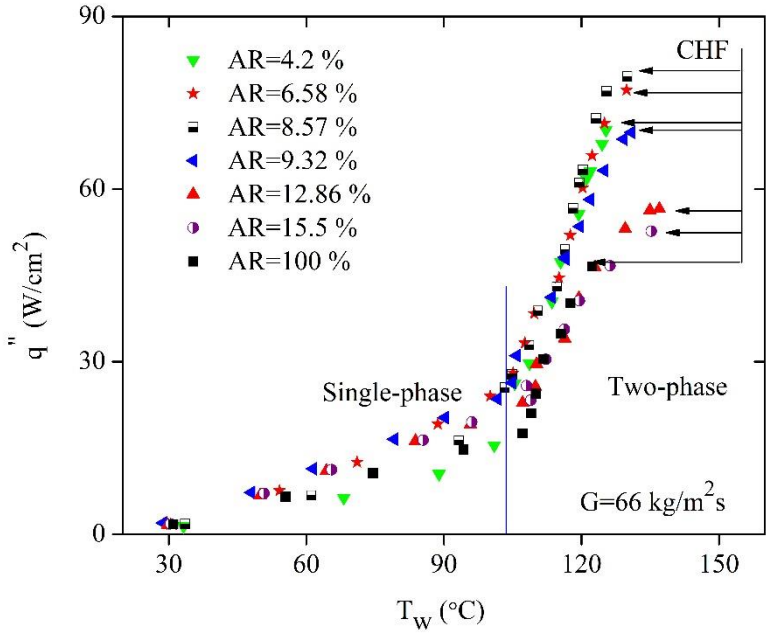

Figure 5.21 The effect of area ratio on the CHFs at G = 66 kg/m^{2}s.

In the single-phase region for each AR, the surface temperature of the heat sink increases almost linearly with heat flux. This is expected for single-phase heat transfer in microchannels. However, the effects of inlet ARs on the single-phase heat transfer performance vary with mass flux. Specifically, for the low mass flux of G = 66 kg/m^{2}s Figure 5.21 the configurations with AR = 9.32%, 12.86% and 15.5% show better performance than other configurations, as the slopes of the boiling curves in the single-

phase region for those three configurations are among the largest. In contrast, the configuration with AR = 4.2% shows the lowest heat transfer rate among all the configurations, including base configuration (i.e., AR= 100%). For the medium mass flux of G = 147.76 kg/m^{2}s (Figure 5.22), all the configurations exhibit nearly the same performance in the single-phase region. However, AR = 4.2% configuration still has one of the highest heat transfer rates among all the 1IR configurations. For the highest mass flux of G = 221.65 kg/m^{2}s (Figure 5.23), the single-phase heat transfer performances show large differences between the configurations. Specifically, the configurations with AR = 4.2%, 6.58% and 8.57% demonstrate higher performance than the configurations with AR = 9.32%, 12.86% and 15.5%, and the base configuration has the lowest single-phase heat transfer rate.

In the two-phase flow region, the slope of the boiling curve increases distinctly for each configuration (Figure 5.21 to Figure 5.23). However, in general, for all three mass fluxes, the configurations with AR = 4.2% and 6.58% exhibit the highest heat transfer rates, followed by the configurations with AR = 8.57%, 9.32%, 12.86% and 15.5%, with the base configuration exhibiting the lowest two-phase heat transfer rate. In other words, all six 1IR configurations improved the two-phase HTCs over the 0IR case. It can also be concluded that the smaller the area ratio is, the large the improvement of the two-phase HTC.

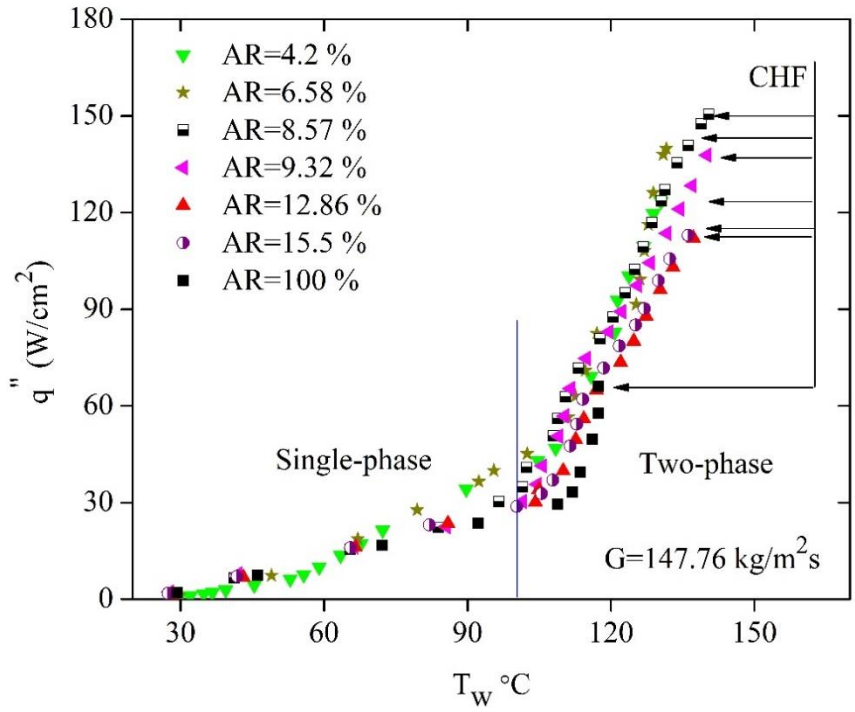

Figure 5.22 The effects of area ratio on the CHFs at G = 147.76 kg/m^{2}s.

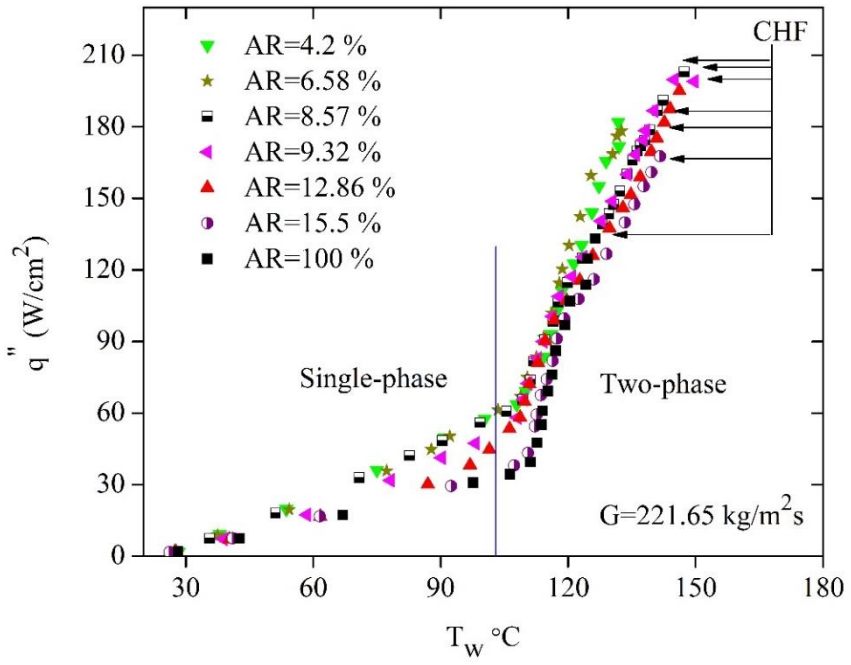

Figure 5.23 The effects of area ratio on the CHFs at G = 221.65 kg/m^{2}s.

In terms of CHF, all six 1IR configurations improved the flow boiling microchannel performance. Among them, the configuration with AR = 8.57% yields the highest CHF, and the configuration with AR = 15.4% has the lowest CHF, for all three mass fluxes. The second through fifth highest CHF depends on the mass flux. Specifically, for low mass flux of G = 66 kg/m^{2}s (Figure 5.21), the second highest CHF is for the configurations with AR = 6.58%, followed by the configurations with AR = 4.2% and 9.32%, respectively. The configuration with AR = 12.86% ranks fifth, with a CHF value slightly larger than that of the AR = 15.5% configuration. For the medium mass flux of G = 147.76 kg/m^{2}s (Figure 5.22), the configurations with AR = 6.58% and 9.32% rank second and third, respectively; followed by the configurations with AR = 4.2%. Again, the configurations with AR = 12.86% and 15.5% are among the lowest rank: their CHF values are almost the same but are much lower than others. For the largest mass flux of G = 221.65 kg/m^{2}s (Figure 5.23), the configurations with AR = 9.32% and 12.86% rank second and third, respectively, with nearly the same CHF as the highest CHF value. The configurations with AR = 4.2% and 6.58% rank fourth and fifth, and their CHF values are almost the same.

Based on the CHF performances, the configuration with AR = 8.57% is deemed as the optimum design. Figure 5.24 illustrates the onset nucleate boiling (ONB) under various mass fluxes for the optimum configuration with AR = 8.57%. As mass flux increases, the ONB delays to a higher surface temperature of the microchannel heat sink, as well as higher heat flux.

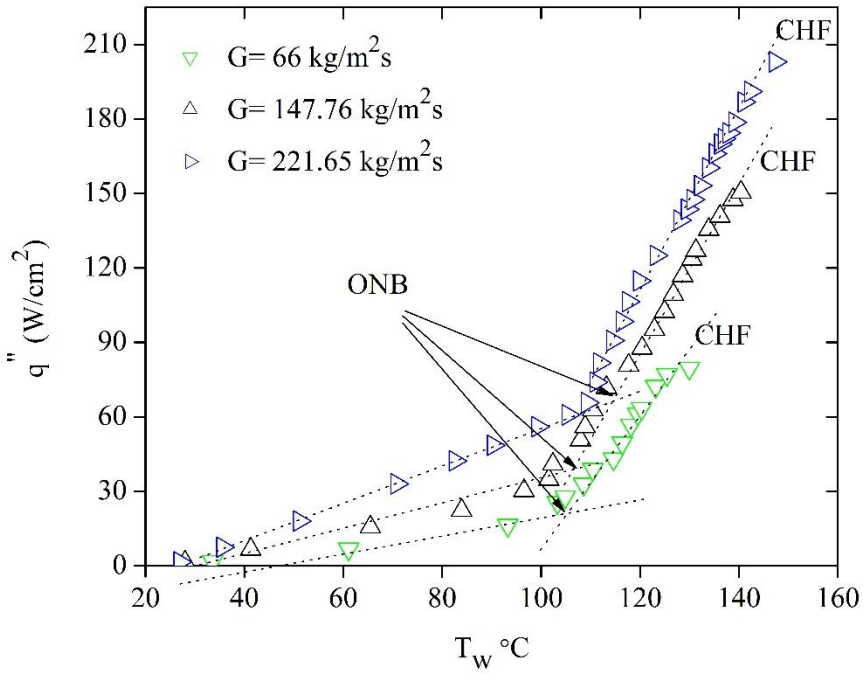

Figure 5.24 ONB at an optimum area ratio of 8.57 %.

5.10.2 Effect of Parametric Trends in CHF

Figure 5.25 shows the IR schematic designed to suppress or eliminate the instability in a flow boiling microchannel. The width of the IR can be changed to get a different area ratio. In convectional microchannels, there are many independent parameters that can strongly affect the CHF, such as mass flux, hydraulic diameter, length, width and height of the channel, exit pressure, fluid thermal physical properties [95], and latent heat [96][97]. In this study, we assume that the exit pressure, latent heat, length, width, and height of the channel are constant. Therefore, the CHF becomes a function of two independent parameters: mass flux and area ratio, as shown in Eq. (34)[96]:.

$$q''_{CHF} = f\,(G, AR) \tag{34}$$

Figure 5.26 shows the CHF as a function of mass flux. CHF is approximately linear with the increase of *G* for all ARs. The correlation can be described as,

$$q''_{CHF} \propto G^m \tag{35}$$

where m is a constant.

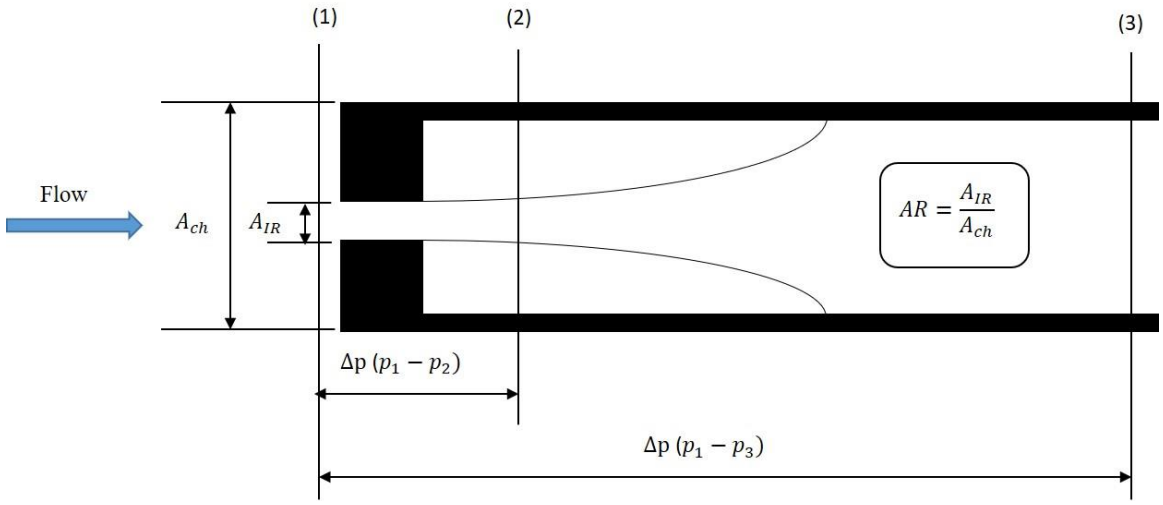

Figure 5.25 Fluid flow through the IR.

Figure 5.27 shows the effects of mass flux and area ratio on CHF, as defined in Eq. (34), with other parameters held constant. The CHF values are obtained from the previous tests for various ARs (4.2 %, 6.58%, 8.57%, 9.32%, 12.86 %, 15.5 %, and 100%), and different mass flux of 66 kg/m^{2}s, 147.76 kg/m^{2}s and 221.65 kg/m^{2}s. Figure 5.27 shows that the CHF peaks at AR = 8.57% for all three mass fluxes. Based on this finding, the optimum arear ratio is proposed to be in the range of 8-10%. The proposed range results from the uncertainties of the IR dimensions.

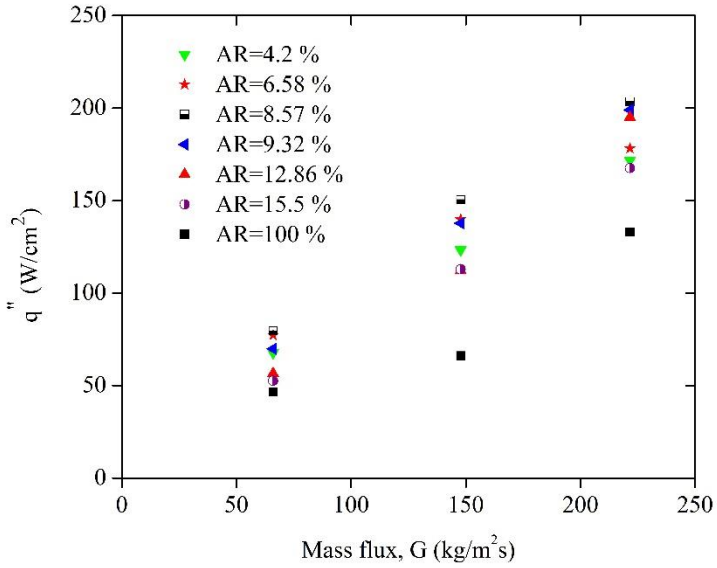

Figure 5.26 CHF as a function of mass flux.

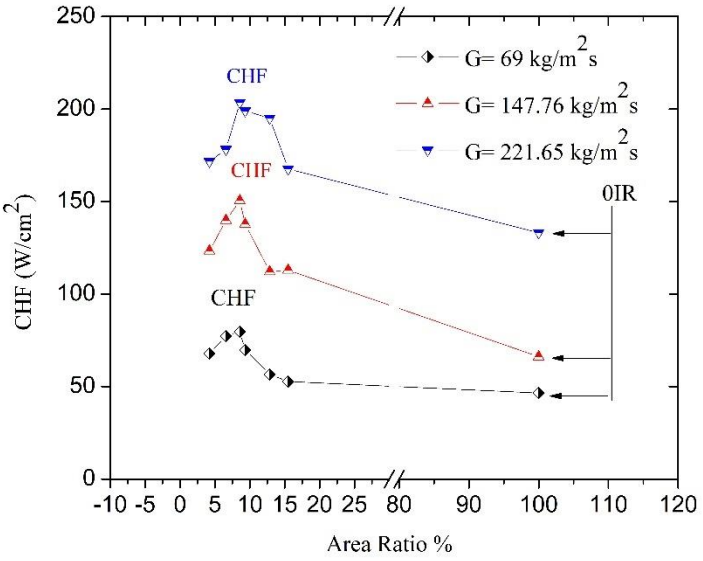

Figure 5.27 Comparison of the CHF enhancements at G =66, 147.76 and 221.65 kg/m^{2}s.

5.11 **Summary**

In this study, experimental investigations were performed to quantify the effects of different IR configurations on heat transfer performance and the effect of mass flux and IRs area ratio on CHF in a flow boiling microchannel heat sink. The main findings are summarized as follows:

(1) All test cases with IRs improved the flow boiling microchannel heat sinks CHF performance, compared to the base case without IRs. The improvements can be mainly attributed to the suppression of flow instabilities.

(2) For lower mass fluxes, cases with multiple-opening IRs (e.g., the 3IR and 5IR cases) generally performed better (e.g., higher CHF) than cases with the single-opening inlet restrictor (e.g., the 1IR case). Compared to the 0IR case, the 5IR, 3IR, and 1IR cases enhanced the CHFs by 52.54%, 20.62% and 13.78%, respectively. This is attributed to a reduced recirculation zone in multiple-opening IR configurations compared to the 1IR case.

(3) For higher mass flux at G= 144 kg/m^{2}s, cases with a higher blocking ratio (e.g., 95.41% for 1IR and 86.23% for 3IR) showed higher CHF than those with relatively smaller blocking ratio (e.g., 77.05% for 5IR). Comparing to the 0IR case, the 5IR, 3IR, and 1IR cases showed enhanced CHFs by 19.22%, 14.53%, and 0.6%, respectively. Performance improvements can be attributed to a reduction in reverse flow oscillations at high mass flux.

(4) IRs slightly reduced the single-phase microchannel HTC at low flow rates, but HTC reduction effects diminished as the flow rate increased.

(5) In addition, IRs generally decreased the two-phase microchannel HTC, and the cases with multiple IRs (e.g., 5IR and 3IR) had relatively higher HTC than that of the 1IR case. Importantly, it was revealed that at high mass flux and high heat flux (Figure 5.15), the IRs improved the HTC of the flow boiling microchannel.

(6) IRs with a higher blocking ratio (e.g., 95.41% for 1IR and 86.23% for 3IR) exhibited higher pressure drop penalties. For instance, compared to the 0IR case at G= 32.68 kg/m^{2}s, the 1IR, 3IR, and 5IR cases increased the pressure drop penalty by 5.79, 2.06, and 1.58 times, respectively. The ratio of gain to penalty (Table 5.3) reveals the optimum configuration of IRs at different mass flux. The optimum configuration depends on the operational parameters, including the mass flux and heat flux, of the microchannel heat sink. The optimum configuration is a compromise between the goals for maximizing the heat transfer performance (e.g., in terms of CHF enhancement) and minimizing the pressure drop penalties.

(7) It can be concluded that CHF is a strong function of mass flux (G) and area ratio (AR).

(8) Finally, the results suggest an optimal area ratio in the range between 8% -10% for all ranges of mass flux between G = 66 kg/m^{2}s to 221.65 kg/m^{2}s. The proposed range results from the uncertainties of the IR dimensions.

CHAPTER 6

EFFECTS OF KNURLED SURFACE ON FLOW BOILING IN A MICROCHANNEL HEAT SINK

This study seeks to quantify the effects of a knurled surface modification on the thermal performance in a flow boiling microchannel heat sink. Like the design described in CHAPTER 4 for the single-phase studies, the diamond-shaped knurling is fabricated on the bottom surface of the microchannel. Two test sections with different knurling heights were designed, fabricated, probed, and compared with the performance of a smooth surface two-phase microchannel heat sink. This chapter reports the analysis and discussion of results.

6.1 **Background**

Knurled surfaces have previously been shown to be effective for heat transfer coefficient enhancement in single-phase microchannels. This study extends the application of knurled surface modification to two-phase microchannel heat sinks. The aim of this study is to experimentally investigate the instability and heat transfer performance in the microchannel heat sink by introducing diamond-shaped knurling with two different roughness heights. The modified knurling designs are then compared with the performance of a smooth surface (0IR) microchannel heat sink. It is expected that the design of the modified surfaces will increase the bubble nucleate sites and thus change the characteristics

of the flow boiling microchannel. Specifically, the effects of two roughness heights on the CHF and pressure drops in the flow boiling microchannel are quantified.

6.2 **Configuration of Knurled Surface Microchannel**

The diamond-shaped knurling surface modification on the top surface of the channel copper block is illustrated in Figure 6.1. Details of the diamond pattern are found in CHAPTER 4. Prior to knurling, the top surface of the copper block was polished using sandpaper sheets with grits of 400, 600, 800, and 1500. The block was then rinsed with ethanol, acetone, and de-ionized water sequentially, followed by a drying process under a nitrogen stream [84]. Next, a knurling tool was used in a modified lathe machine to implement the designed knurling pattern. The heights of the diamond-shaped knurling were 0.25 mm (R-1) and 0.17 mm (R-2). The knurling pitch for each roughness was 1 mm, and the angle of corrugation for each diamond was 45 degrees.

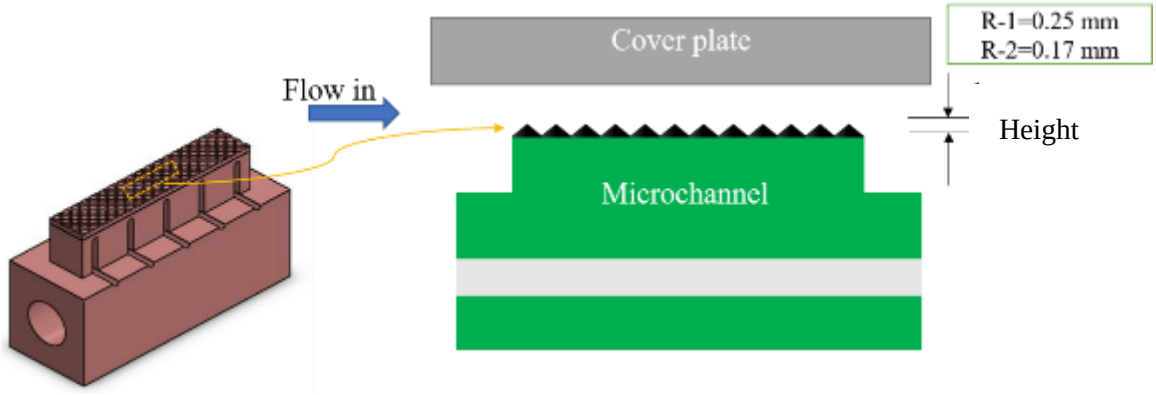

Figure 6.1 A diagram of the knurled microchannel heat sink with the substrate.

6.3 **Results and Discussion**

In this section, the experimental results for the effects of the knurling surface roughness on the CHF and pressure drops (Δp) in the flow boiling microchannel are presented and examined.

6.3.1 Boiling Curve and Influence of Knurling Surface on Heat Transfer Performance

Figure 6.2 to Figure 6.4 illustrate the effect of knurling on boiling curves at mass fluxes G = 66.48 kg/m^{2}s, 172.87 kg/m^{2}s, and 286 kg/m^{2}s, respectively. Each figure contains boiling curves corresponding to the three roughness configurations investigated: R-1, R-2, and the base case (0IR), which are plotted on the same graph for comparison. The results show that the heat transfer performance increases with increasing knurling surface height at all observed mass fluxes. Both the R-1 and R-2 cases exhibited better performance than the base case. Compared to the 0IR case at max flux of 66.48 kg/m^{2}s and wall temperatures of 107.5 ℃ and 113.5 ℃, R-1 enhanced the effective heat flux by 72.84% and 81.06%, respectively, and R-2 enhanced the effective heat flux by 33.89% and 34.62%, respectively. In contrast, at mass flux increased to 172.87 kg/m^{2}s and wall temperatures of 115.6 ℃ and 120.27 ℃, R-1 enhanced the effective heat flux by 65.17% and 38.38%, respectively, and R-2 improved the effective heat flux by 11.58% and 4.81%, respectively.

As shown in Figure 6.2 and Figure 6.3, both the R-1 and R-2 cases change the onset of nucleate boiling from that of the base case. The Onset of Nucleate Boiling (ONB), is defined as the location where the bubble appears on the heated surface [98]. An earlier occurrence of ONB for the rougher surface (R-1) is due to the existence of higher nucleation sites [54].

Figure 6.5 compares the flow boiling curve for mass flux G = 66.48 kg/m^{2}s and G = 286 kg/m^{2}s for the same R-1 case. It shows the effect of different mass flux on the ONB incipient. The wall temperature, as well as the effective heat flux for ONB increases as the mass flux increases. Moreover, the bubble dynamics are also changed when the mass flux increases. As discussed above, the nucleation site density increases with mass flux increase. Furthermore, the bubble mean diameter decreases, while the mass flow rate increases due to the reduction in the bubble growth time [54][98]. It was determined that the heat transfer for the high roughness (R-1) case is much larger than that for the low roughness (R-2) case due to the breakup and regeneration of the boundary layer and the mixing of hot and cold water in between two roughness.

The flow visualization shown in Figure 6.6 compares the bubble dynamics for the R-1 and R-2 cases under the same test conditions. For the R-1 case, the rougher surface demonstrates large active nucleation sites, which lead to higher bubble density. The flow boiling characteristics at a mass flux of G = 286 kg/m^{2}s, for the test cases with the R-1 and R-2 roughness surfaces are presented in Figure 6.4. The R-1 case has greater heat transfer performance than that of the R-2 case. Compared to the R-2 case, the enhancement of effective heat flux for the R-1 case was 87.22% and 34.65% at wall temperatures of 115.21 °C and 118.65 °C, respectively. The same mechanism discussed above also explains why the thermal performance of R-1 is better than that of R-2.

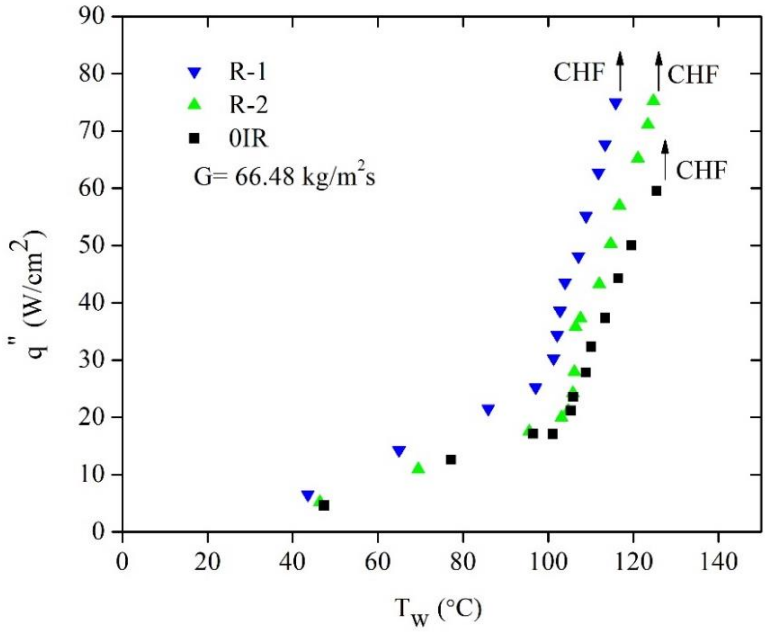

Figure 6.2 Comparison of boiling curves of microchannels for 0IR, R-1, and R-2 at G = 66.48 kg/m2s.

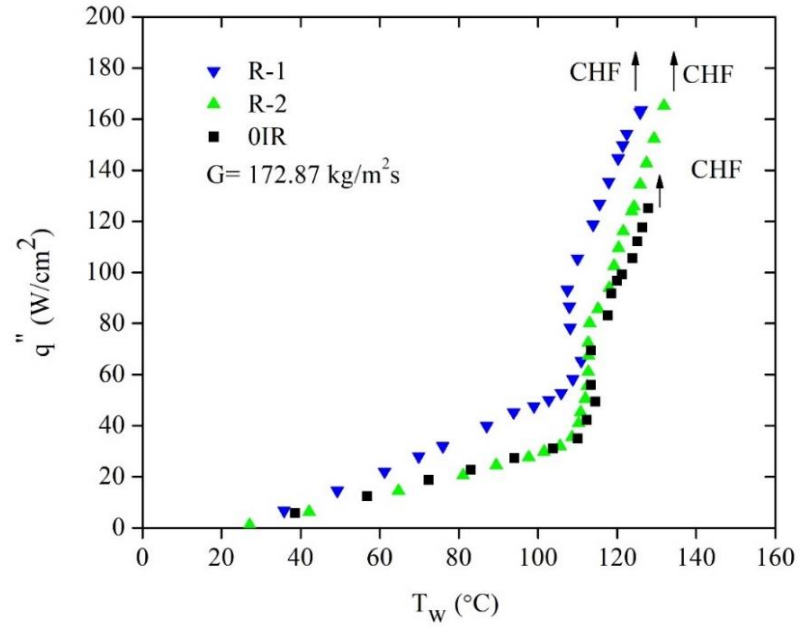

Figure 6.3 Comparison of boiling curves of microchannels for 0IR, R-1, and R-2 at G = 172.87 kg/m^{2}s.

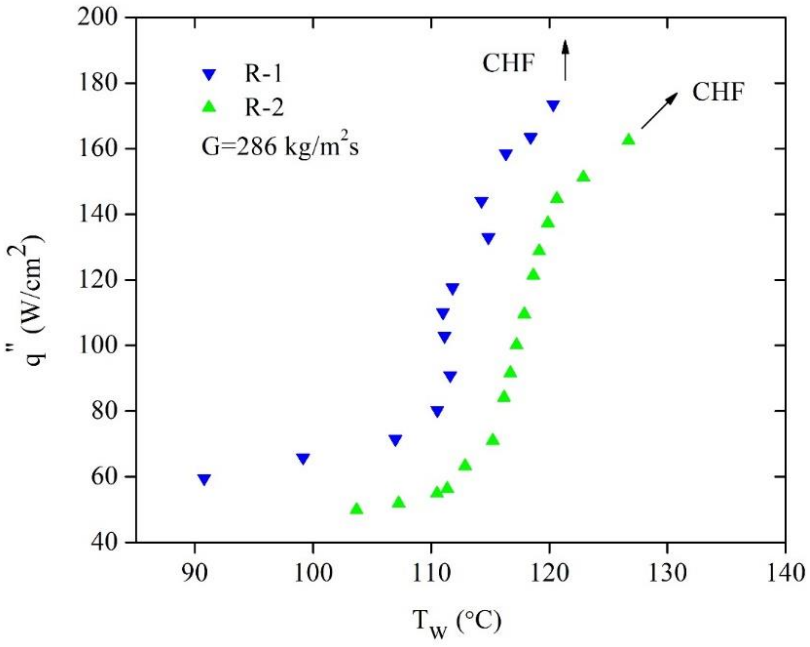

Figure 6.4 Comparison of boiling curves of microchannels for R-1, and R-2 at G = 286 kg/m^{2}s.

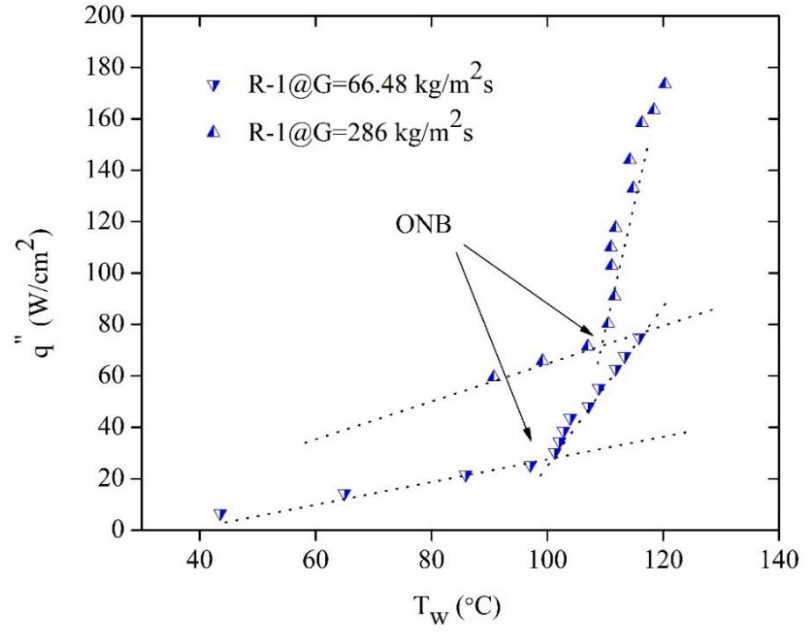

Figure 6.5 Average wall temperature for R-1 at G = 66.48 kg/m^{2}s and G = 286 kg/m^{2}s.

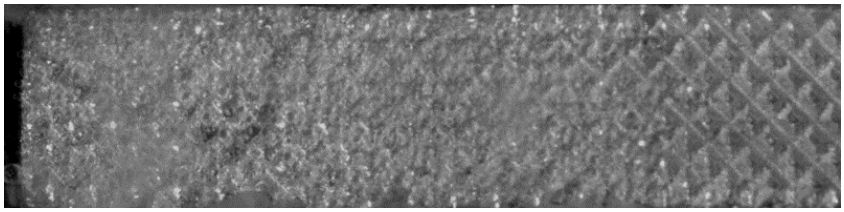

(a) q" = 60 W/cm^2

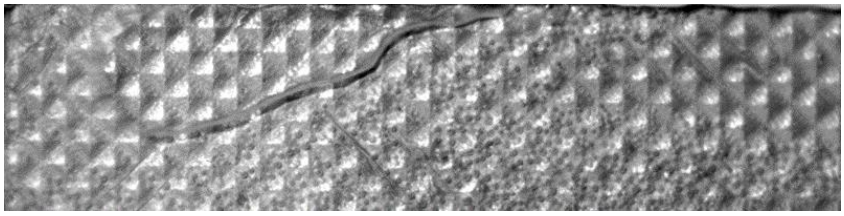

(b) q" = 60 W/cm^2

Figure 6.6 Flow visualization of boiling process at heat fluxes for , G = 172.87 kg/m^{2}s at, (a) R-1 = 0.25 mm, (b) R-2 = 0.17 mm.

6.4 **The Effects of Knurling on the CHF**

Figure 6.7 shows that, compared to the 0IR base case with surface roughness of 0.0 mm [55], the CHF for both the R-1 and R-2 cases are all improved at mass flux G = 66.48 kg/m^{2}s and 172.87 kg/m^{2}s. Specifically, at G = 172.87 kg/m^{2}s, the improvements of the CHF for the roughened surfaces are around 30% higher than the CHF for the smooth surface. Therefore, the knurled surfaces have substantially improved the CHF performance of the flow boiling microchannel. Note that in Figure 6.7, the data points corresponding to G = 286 kg/m^{2}s were not included in the plot, because for the higher mass flux G = 286 kg/m^{2}s), the CHF was not achieved due to the limitation of power supply in the experiments.

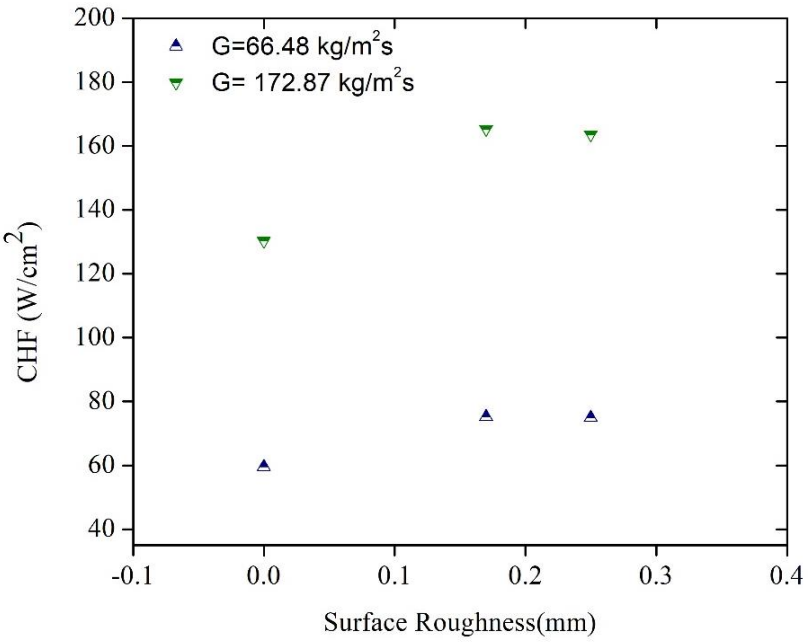

Figure 6.7 CHF versus surface roughness for G = 6648 kg/m^{2}s and 172.87 kg/m^{2}s.

6.5 **Pressure Drops**

Next, the effect of pressure drops as a function of surface roughness were investigated. Figure 6.8, Figure 6.9, and Figure 6.10 show the pressure drop curves for the two knurling roughness surfaces (R-1 and R-2) at three different mass fluxes of 66.48 kg/m^{2}s, 172.87 kg/m^{2}s and 285 kg/m^{2}s, respectively, compared with a smooth 0IR surface. The pressure drop was computed using the measured pressure drop between the upstream and downstream plenums, subtracting the various losses from sudden contractions and expansions. The pressure drop for both rough microchannels (i.e. R-1 and R-2) was not significant in comparsion to the base case. Also, the pressure drop was independent of mass flux and heat flux until the boiling started. Pressure drop gradually increased after reaching

the ONB. The increase in heat flux can be attributed to changing the velocity of vapor bubble and as heat flux increase the shape of bubble will be increased as well.

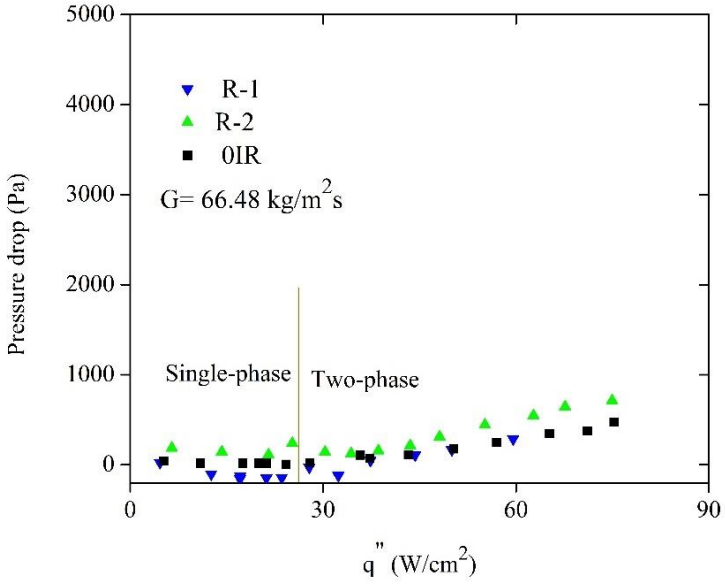

Figure 6.8 The effect of knurling surface on pressure drops at G = 66.48 kg/m^{2}s and T_{in} = 23 °C.

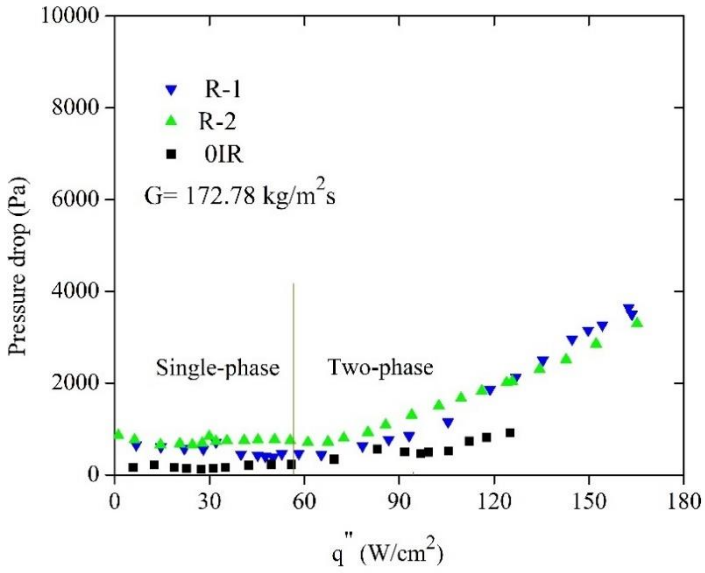

Figure 6.9 The effect of knurling surface on pressure drops at G = 172.87 kg/m^{2}s and T_{in} = 23 °C.

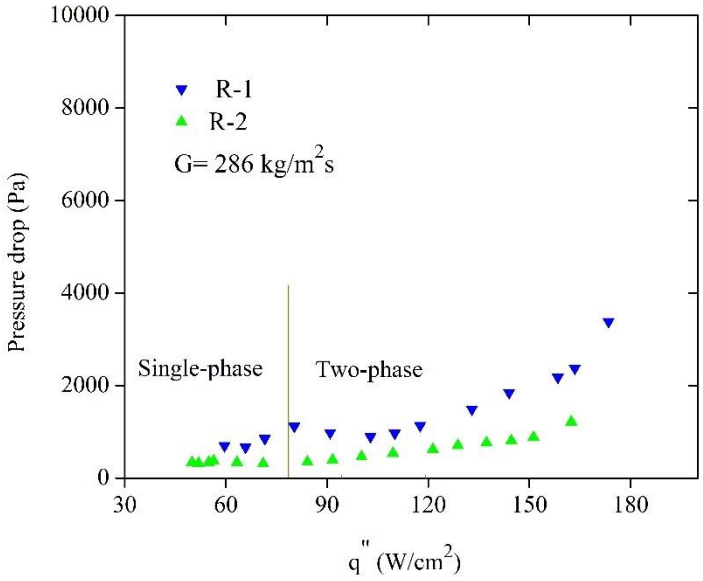

Figure 6.10 The effect of knurling surface on pressure drops at G = 286 kg/m^{2}s and T_{in} = 23 °C.

6.6 **Fluctuation of Wall Temperature and Inlet Pressure**

The effects of diamond-shaped knurling on the inlet pressure fluctuations and the local wall surface temperature fluctuations (measured at the thermocouples T5 location) are depicted in Figure 6.11 and Figure 6.12, at mass flux G = 172.87 kg/m^{2}s and at four values of heat fluxes, respectively. The two diamond-shaped knurling configurations, i.e., R-1 and R-2, were tested and compared with the base case. The standard deviation, (σ) was computed to indicate the deviation of the measured amplitudes from their mean value, which is given by the following equations.

$$\sigma\,(T) = \sqrt{\frac{\sum_{n=1}^{n}(T_n - \bar{T}_n)^2}{n}} \tag{36}$$

$$\sigma\,(P_{in}) = \sqrt{\frac{\sum_{n=1}^{n}(P_{in,n} - \bar{P}_{in,n})^2}{n}} \tag{37}$$

where *n* is the number of data collected at a specific heat flux under a given mass flux condition. The diamond-shaped knurling at higher roughness (R-1) sustained much lower wall temperature and inlet pressure drop fluctuations than that of the 0IR case for all four tested heat fluxes. The R-1 case displayed the lowest fluctuation for inlet pressure and wall temperature, followed by the R-2 case, and then the base case (0IR). Compared to 0IR case, the standard deviations of wall temperature are reduced approximately by 91.3–58.6% and 78.7–20.2% for R-1 and R-2, respectively. The standard deviations for inlet pressure are reduced approximately by 2–59% for R-1 and 2–35% for R-2, for the heat flux between 42 W/cm^2 and 91 W/cm^2, respectively. The reduction in temperature and inlet pressure fluctuations, for both R-1 and R-2 cases, may be due to the roughed surfaces increase the nucleation sites; thus, smaller bubbles were generated at the same mass and heat flux, leading to smaller flow boiling instability. Whereas the base case (0IR) has a large fluctuation in wall temperature and pressure drop because there are relative less nucleation sites on the smooth surface, under the same mass and heat flux, less bubble were generated and they experience quick growth, expansion and flushing process [54]. In conclusion, diamond-shaped knurling surfaces produce more stable bubble nucleation sites than the smooth surface, thus avoiding large amplitude of fluctuations.

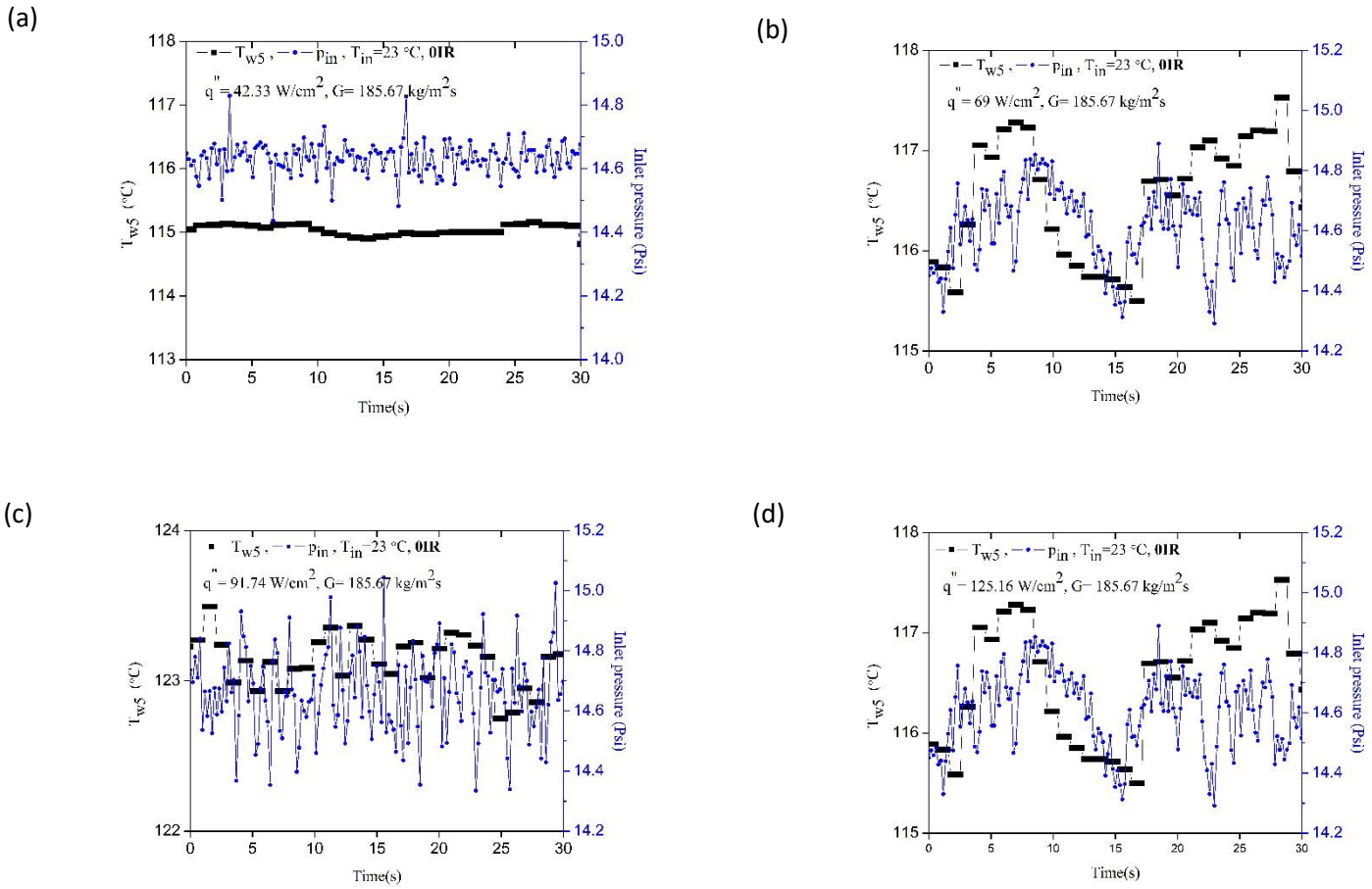

Figure 6.11 Fluctuations of local thermocouple readings (at T5), and inlet pressure for the 0IR design at G = 185.67 kg/m^{2}s and (a) q" = 42.33 W/cm^2 (b) q" = 69 W/cm^2 (c) q" = 91.74 W/cm^2 and (d) q" = 125.16 W/cm^2.

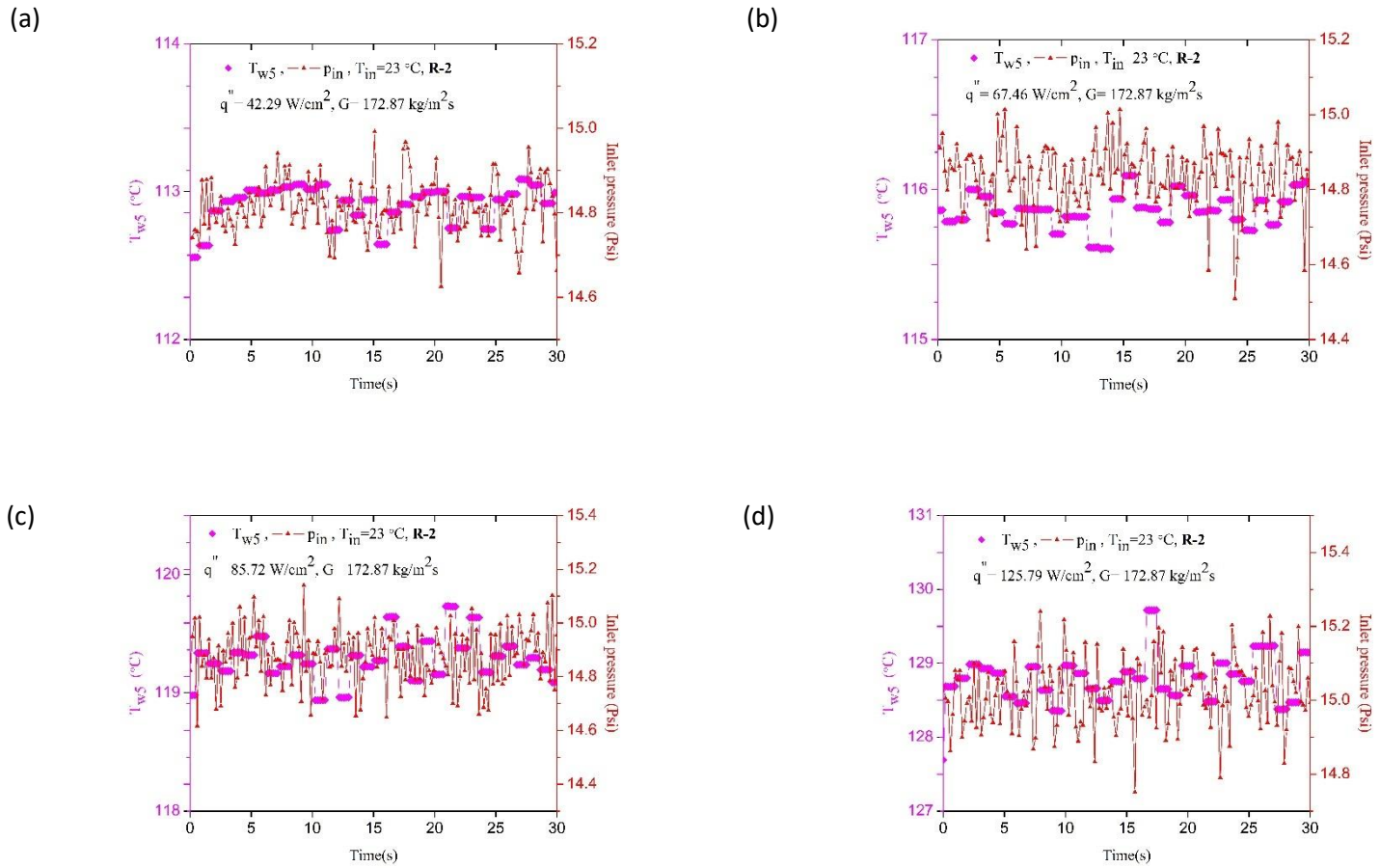

Figure 6.12 Fluctuations of local thermocouple readings (at T5), and inlet pressure for the R-2 design at G = 172.87 kg/m^{2}s and (a) q" = 42.29 W/cm^2 (b) q" = 67.46 W/cm^2 (c) q" = 85.72 W/cm^2 and (d) q" = 125.79 W/cm^2.

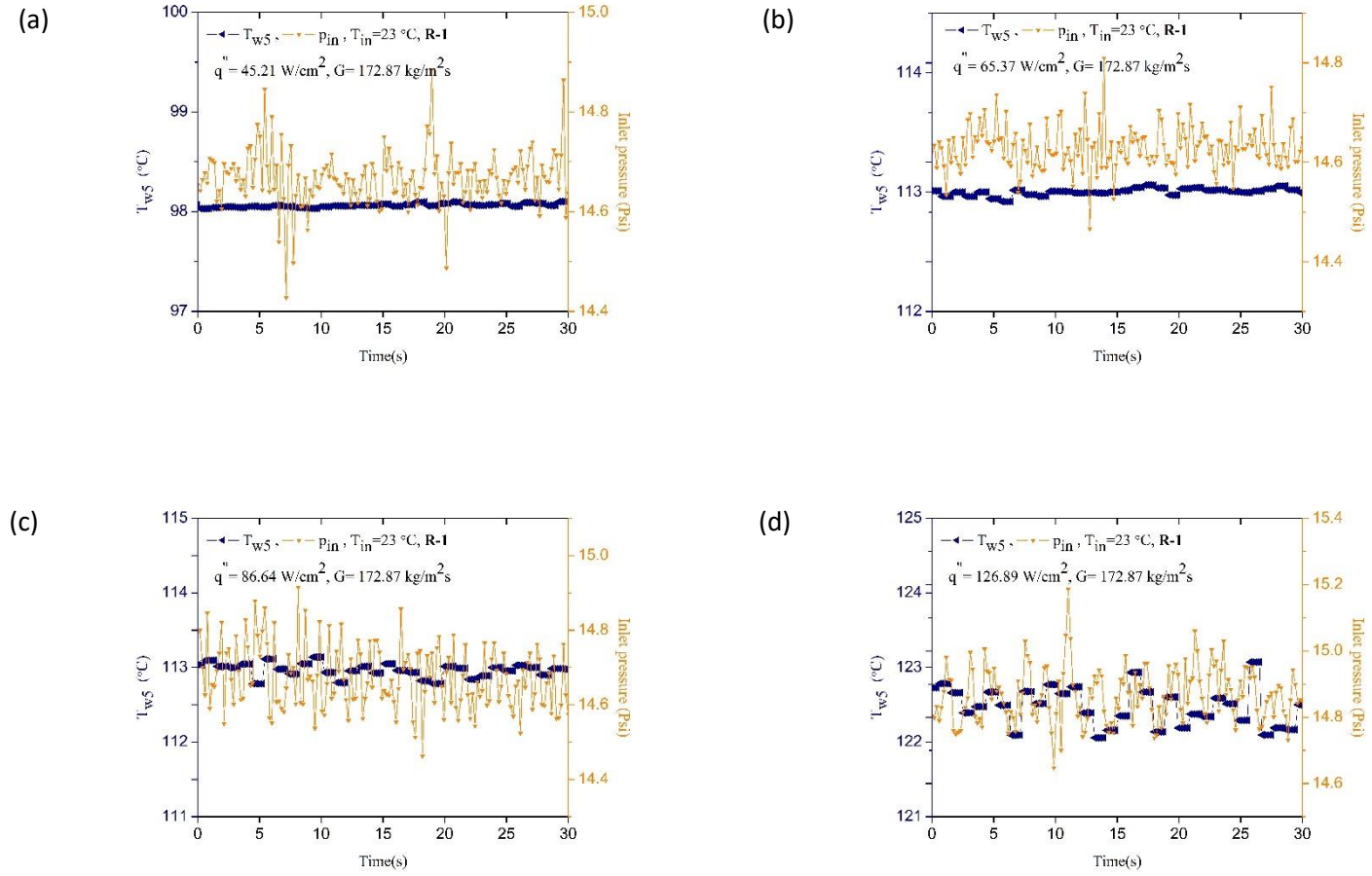

Figure 6.13 Fluctuations of local thermocouple readings (at T5), and inlet pressure for the R-1 design at G = 172.87 kg/m^{2}s and (a) q" = 45.21 W/cm^2 (b) q" = 63.37 W/cm^2 (c) q" = 86.64 W/cm^2 and (d) q" = 126.89 W/cm^2.

6.7 **Summary**

The effect of knurled surfaces on the heat transfer performance, critical heat flux, and pressure drops in the flow boiling microchannel heat sink were studied experimentally. Two different knurling heights (denoted as R-1 and R-2) on the bottom surface of the microchannel heat sink were investigated. The effects of the knurled surfaces on the microchannel wall temperature and inlet pressure fluctuations were also analyzed. It was concluded that the roughed surfaces for both the R-1 and R-2 cases do not significantly influence the pressure drops, compared to the base case. Also, the pressure drop is independent of mass flux and heat flux until the boiling started, and pressure drop across the microchannel increases slightly with the roughness of R-1 and R-2 at highest mass flux ($G = 285.9\ kg/m^2\ s$). Both roughed surfaces (R-1 and R-2) improve the critical heat flux in comparison to that of the smooth case. Specifically, around 30% improvement in CHF is achieved for the R-1 case at $G = 172.87\ kg/m^2s$. In addition, both R-1 and R-2 enhanced the heat transfer coefficient compared to the base case. A maximum heat transfer enhancement of 81.06% was achieved for the R-1 case. The fluctuations of wall temperature and inlet pressure were relatively stable for the R-1 case as compared to the R-2 case and base case. In conclusion, diamond-shaped knurling (especially the more roughed R-1 case) can effectively enhance flow boiling microchannel heat transfer performance in both the heat transfer coefficient, as well as the CHF.

CHAPTER 7

INVESTIGATION OF THE COMBINED EFFECTS OF IR AND KNURLING SURFACE ON THE HEAT TRANSFER AND CHF IN MICROCHANNEL HEAT SINKS

In this chapter, the two effective techniques that have been used to mitigate flow boiling instability in the previous discussions, namely, IR as discussed in CHAPTER 5 and the knurling surface modification as discussed in CHAPTER 6, were used together to further improve the heat transfer performance inside the flow boiling microchannel heat sinks. Specifically, the investigation targets to further understand how the combination of the two technologies affects heat transfer rate and CHF in the microchannel two-phase flow. The optimal design values for the IR obtained in CHAPTER 5, together with the optimal design for the knurling surface obtained in CHAPTER 6, are used together in the IR-knurling hybrid microchannel heat sink design. Experimental results for this hybrid design are reported and analyzed in the following sections.

7.1 Configuration of IR-Knurling Hybrid Microchannel

Figure 7.1 shows a schematic of the configuration of the microchannel with an IR and knurled rough surface. The dimensions of the microchannel and the IRs, and the flow conditions are listed in Table 7.1. The design of the IR is a rectangular block with a slot opening on the middle of it and is installed at the entrance of the microchannel. It is the same as that for the 1IR design (with an area ratio of 8.57%), as described in Section 5.9.

Similarly, the design of the knurled surface is the same that for the R-1 design as presented in Section 6.2, namely, the height of the diamond-shaped knurling is 0.25mm (R-1), the pitch is 1 mm, and the angle of corrugation for each diamond is 45°.

Table 7.1 Dimensions of the microchannel with IR and knurled rough surface, and the mass flow rates used in the experiments.

Device Description	G (kg/m^2s)	L (mm)	W (mm)	H (μm)	L_{IR} (mm)	W_{IR} (mm)	H_{IR} (μm)	Slot opening Ratio $AR = \left(\frac{A_{IR}}{A_{ch}}\right)$
Base case(R-1)	66.48 172.87 286.0	26	5	250	--	--	--	--
IR		26	5	250	2	0.508	381	8.57 %

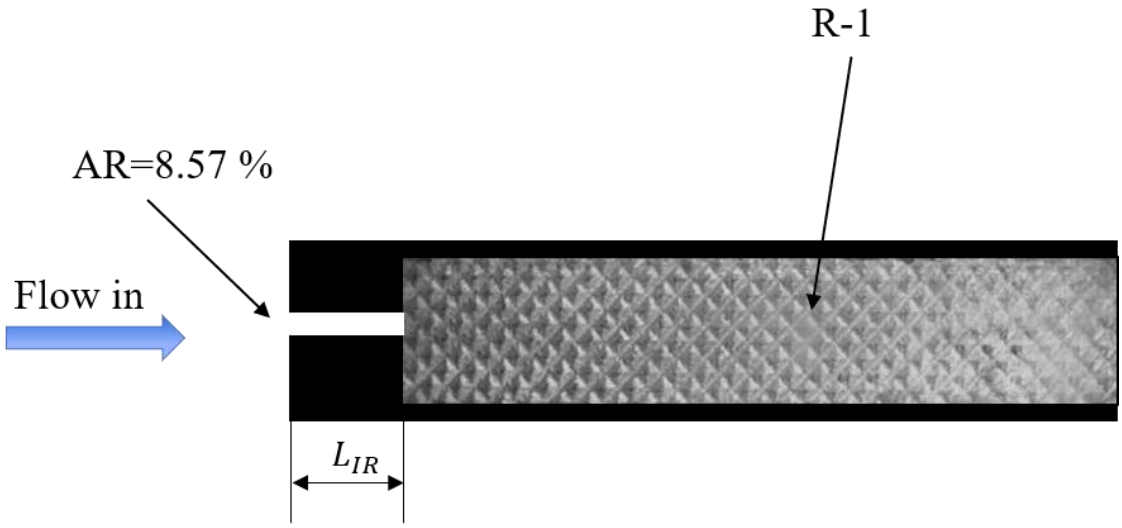

Figure 7.1 Schematic of the microchannel with the combination of IR and knurled rough surface.

7.2 Results and Discussion

In this section, the experimental results for the CHF and pressure drop (Δp) in the flow boiling microchannel enhanced with both the IR and knurling surface are presented and discussed.

7.2.1 Effects of the Hybrid IR&R-1 Design on the CHF

Figure 7.2 to Figure 7.4 show the effects of the hybrid IR&R-1 design on the CHF, for three different mass fluxes of G = 66.48, 172.87, and 286 kg/m^2, respectively. For all test cases, the inlet water temperature was kept at 23 °C.

The flow boiling characteristics at a low mass flux of G = 66.48 kg/m^{2}s in the microchannel with the IR&R-1 configuration is presented in Figure 7.2, and is compared with that for the R-1 case (i.e., with knurling but without the IR) and the base case (the 0IR case: without IR and knurling). It is found that the IR&R-1 case exhibits the highest CHF, followed by R-1 and 0IR cases, respectively. As shown in Figure 7.2, when G = 66.48 kg/m^{2}s, the IR&R-1 case has improved the CHF of the flow boiling microchannel compared to the 0IR and R-1 cases. Compared to the R-1 case, the IR&R-1 design has enhanced the CHF by 10%; and compared to the 0IR case, the IR&R-1 design has enhanced the CHF by around 38.36%. This is as expected because of the combined effects: (i) the IR increases the inlet pressure to the microchannel so that the reverse flow cannot easily extend into the inlet plenum. Thus, the pressure drop fluctuations can be reduced considerably, which leads to partially stabilized flow boiling in the microchannel and higher CHF. (ii) Additionally, the knurled rough surface increases the nucleation sites of the flow boiling microchannel, which benefits the bubble growth, expansion, and explosion process in the microchannel, as discussed in CHAPTER 6.

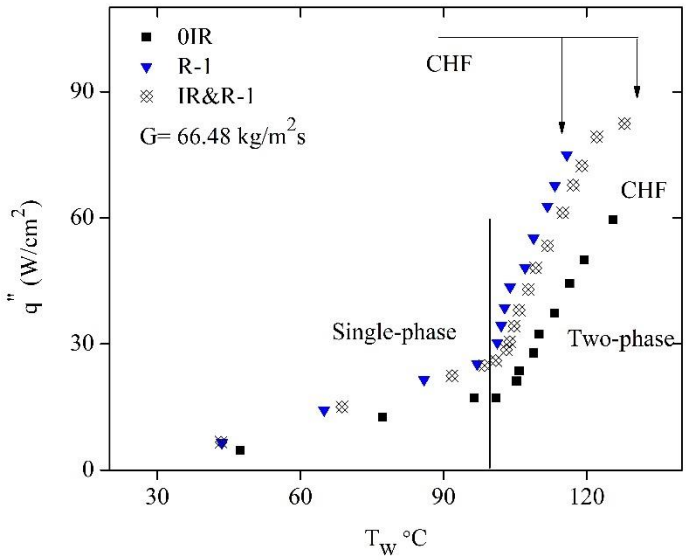

Figure 7.2 The effect of IR&R-1 on the CHFs at G = 66.48 kg/m^{2}s.

The flow boiling characteristics at the mass flux of G = 172.87 kg/m^{2}s and G=286 kg/m^{2}s for the test cases IR&R-1, R-1 and 0IR, are depicted and compared in Figure 7.3 and Figure 7.4, respectively. For both mass fluxes, the results show that the CHFs for the IR&R-1 case are higher than that for the 0IR case but are almost the same as the CHF of the R-1 case. In other word, for higher mass fluxes, the CHF for the hybrid design does not seem to be improved over the R-1 design. Specifically, for the mass flux of G = 66.48 kg/m^{2}s, in comparison with the 0IR case, both the IR&R-1 and R-1 cases show enhancements in the CHF, which are around 26% and 30%, respectively. For the mass flux of G = 286 kg/m^{2}s as shown in Figure 7.4, for, in comparison with the R-1 case, Again, the CHF for IR&R-1 case is almost the same as that of the R-1 case. The no enhancements in CHF for higher mass fluxes for the IR&R-1 design, as shown in both Figure 7.3 and Figure 7.4, are not as expected. The hybrid IR&R-1 design, namely, adding an IR at the entrance to the R-1 design, should also improve the microchannel flow stability and the CHF for

higher mass fluxes. Because of the complexity of the flow boiling phenomena in the IR&R-1 configuration, the ineffectiveness in improving the CHF for higher mass flux needs to be further investigated.

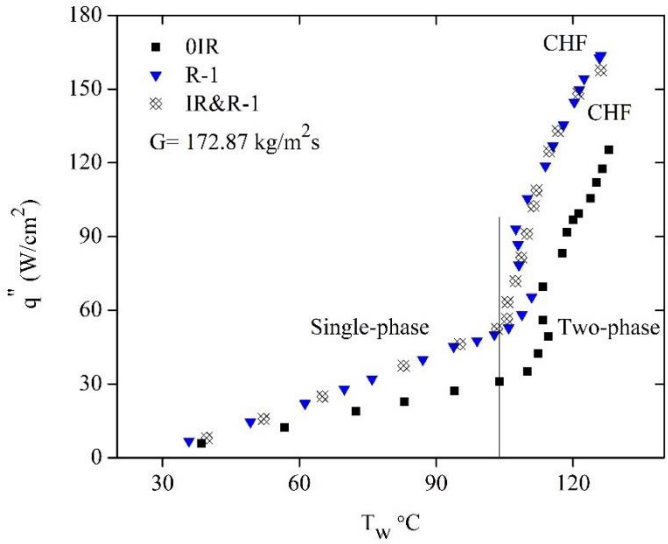

Figure 7.3 The effect of IR&R-1 on the CHFs at G = 172.87 kg/m^{2}s.

7.3 **Pressure Drops**

Figure 7.5, Figure 7.6, and Figure 7.7 show the pressure drop curves for the IR&R-1 design, and comparisons with the R-1 and 0IR cases, for two different mass fluxes kept at 66.48 kg/m^{2}s and 172.87 kg/m^{2}s, respectively. The pressure drops for IR&R-1 are significantly higher than the corresponding R-1 and 0IR cases. The results also indicate that pressure drops for IR&R-1 depend on mass fluxes and heat fluxes, in both the single-phase and two-phase microchannel flow regimes. The significant increase of pressure drops for the IR&R-1 design can be attributed to the IR component, which inevitably increases the overall pressure drop across the IR&R-1 design. Obviously, as shown in Figure 7.7, for the IR&R-1 design, and compared with the R-1 for mass fluxes of 286

kg/m^{2}s, the pressure drops for the IR&R-1 design case are significantly larger than those of R-1. This is expected since the IR is functioned to raise the inlet pressure so that the reverse flow cannot easily extend into the inlet plenum.

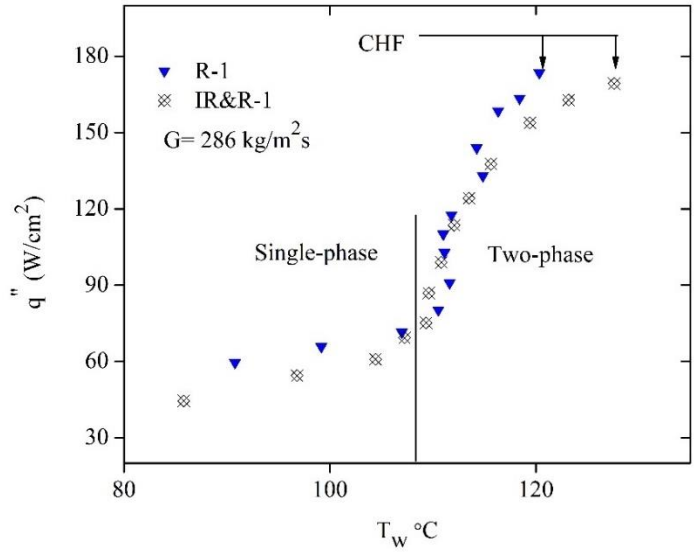

Figure 7.4 The effect of IR&R-1 on the CHFs at G = 286 kg/m^{2}s.

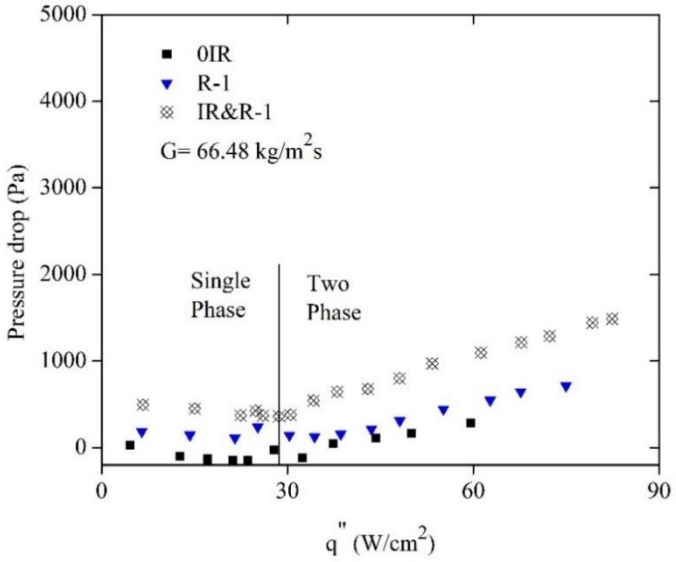

Figure 7.5 The effect of IR&R-1 on pressure drops at G = 66.48 kg/m^{2}s and T_{in} = 23 °C.

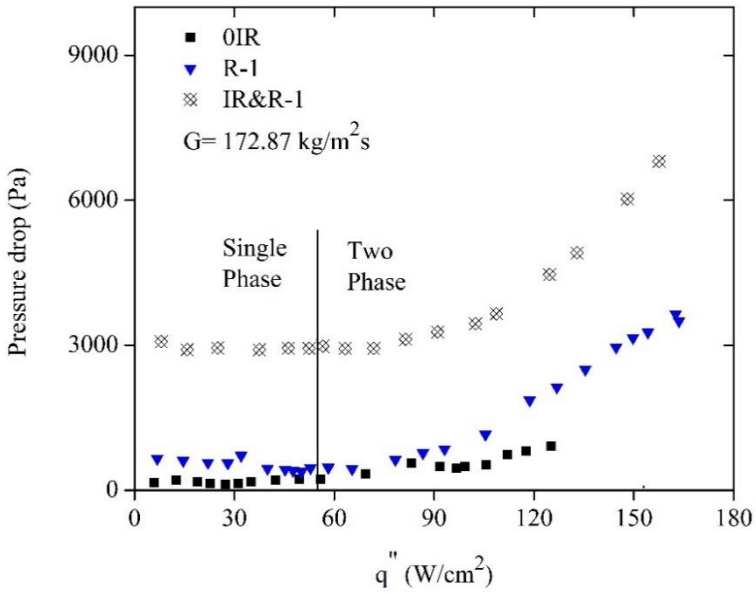

Figure 7.6 The effect of IR&R-1 on pressure drops at G = 172.87 kg/m^{2}s and T_{in} = 23 °C.

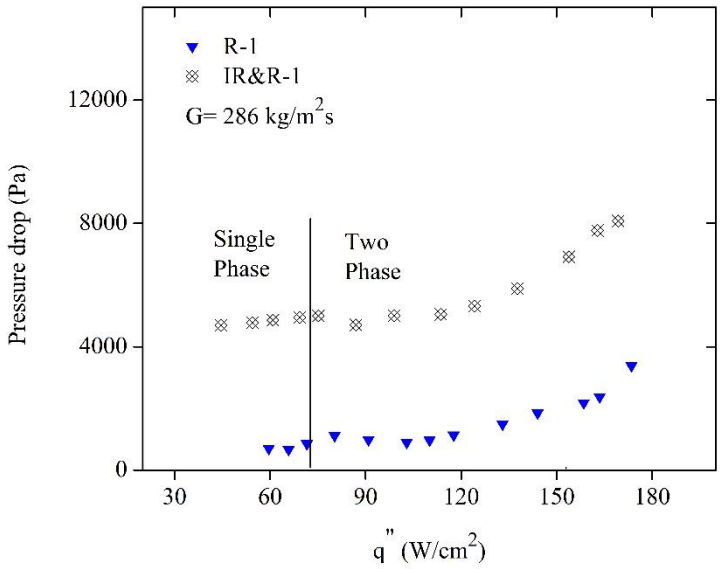

Figure 7.7 The effect of IR&R-1 on pressure drops at G = 286 kg/m^{2}s and T_{in} = 23 °C

7.4 **The Fluctuation of Wall Temperature and Inlet Pressure**

Figure 7.8 shows the effects of the IR&R-1 design on the inlet pressure fluctuations and the local wall surface temperature fluctuations (at where the thermocouple T5 located, i.e., 24 mm from the inlet of the channel), at mass flux G = 172.87 kg/m^2 s and at three different values of heat fluxes, respectively. It can be observed that the IR&R-1 sustains lower inlet pressure fluctuations in comparison to the corresponding R-1 case and 0IR case, as shown in Figure 7.9 and Figure 7.10, respectively. Specifically, the inlet pressure fluctuations for the IR&R-1 case are decreased approximately by 61%and 42%, compared with the corresponding 0IR case for the heat flux at around 63 W/cm^{2}and 125 W/cm^2, respectively. The standard deviation (σ) of the wall temperature fluctuations is reduced approximately by 84% at low heat flux 63 W/cm^2; however, it is increased approximately by 68% at heat flux 125 W/cm^2.

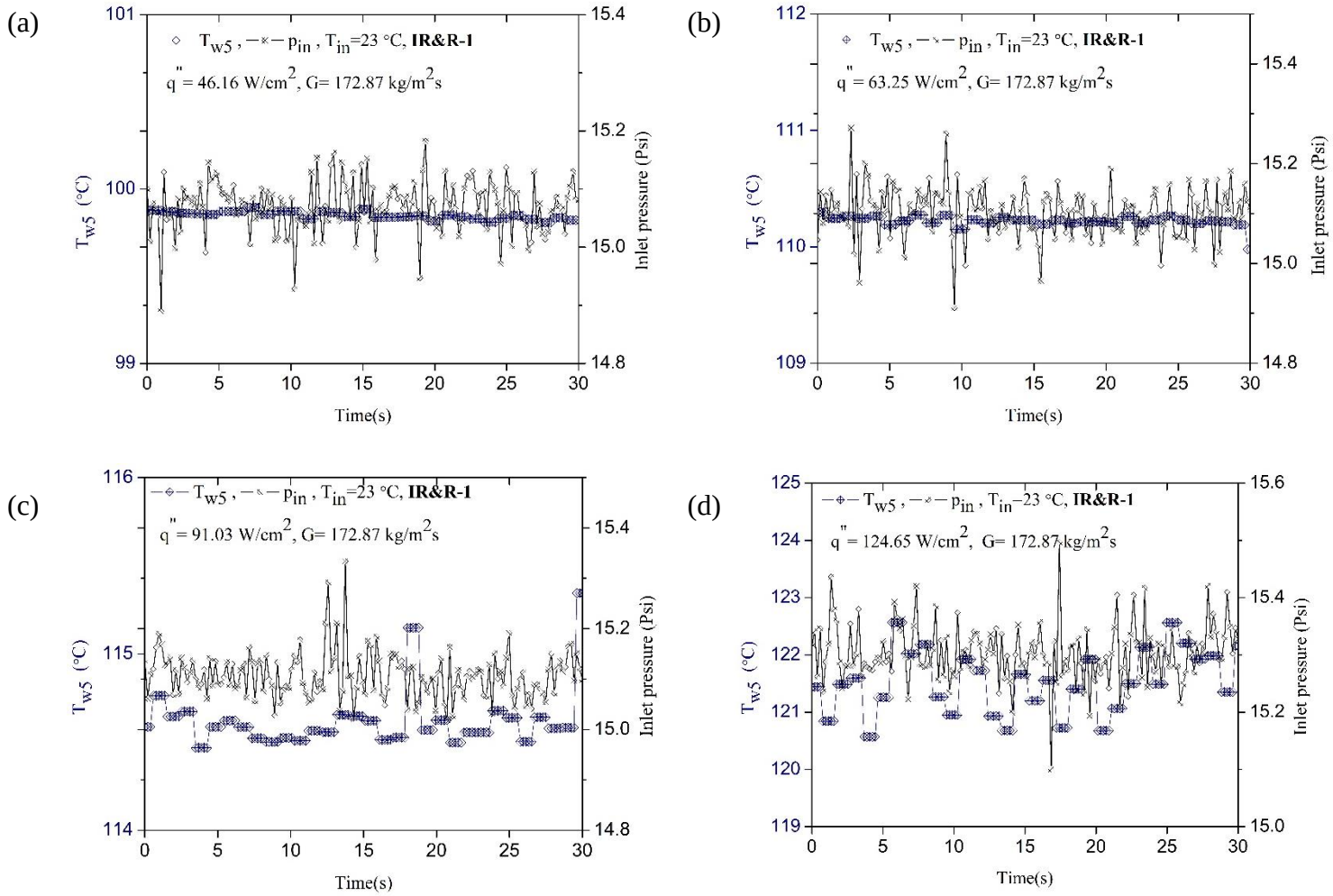

Figure 7.8 Fluctuations of local thermocouple readings (at T5), and inlet pressure for the IR&R-1 design at G = 172.87 kg/m^{2}s and (a) q" = 46.16 W/cm^2 (b) q" = 63.25 W/cm^2 (c) q" = 91.03 W/cm^2 and (d) q" = 124.65 W/cm^2.

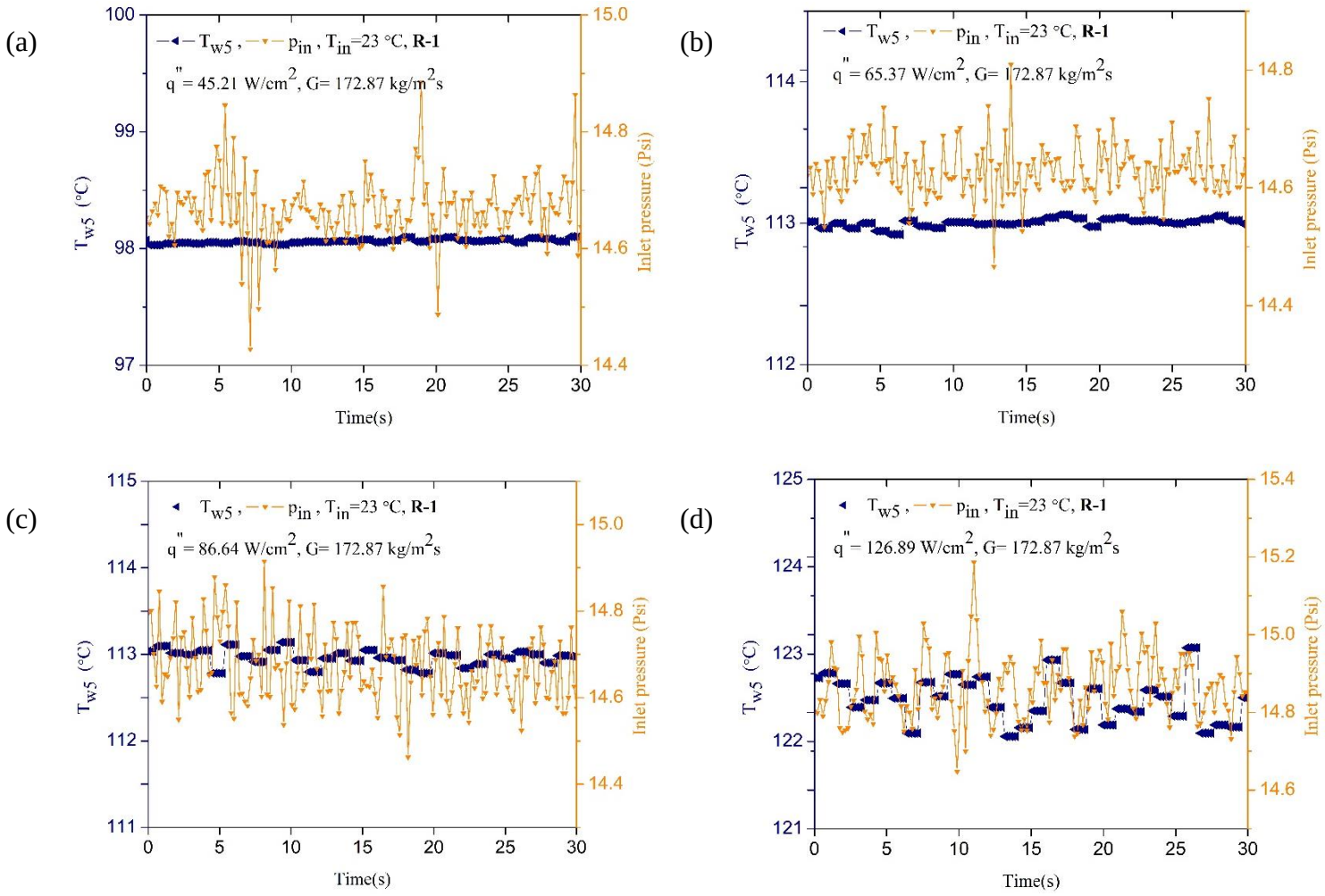

Figure 7.9 Fluctuations of local thermocouple readings (at T5), and inlet pressure for the R-1 design at G = 172.87 kg/m^{2}s and (a) q" = 45.21 W/cm^2 (b) q" = 65.37 W/cm^2 (c) q" = 86.64 W/cm^2 and (d) q" = 126.89 W/cm^2.

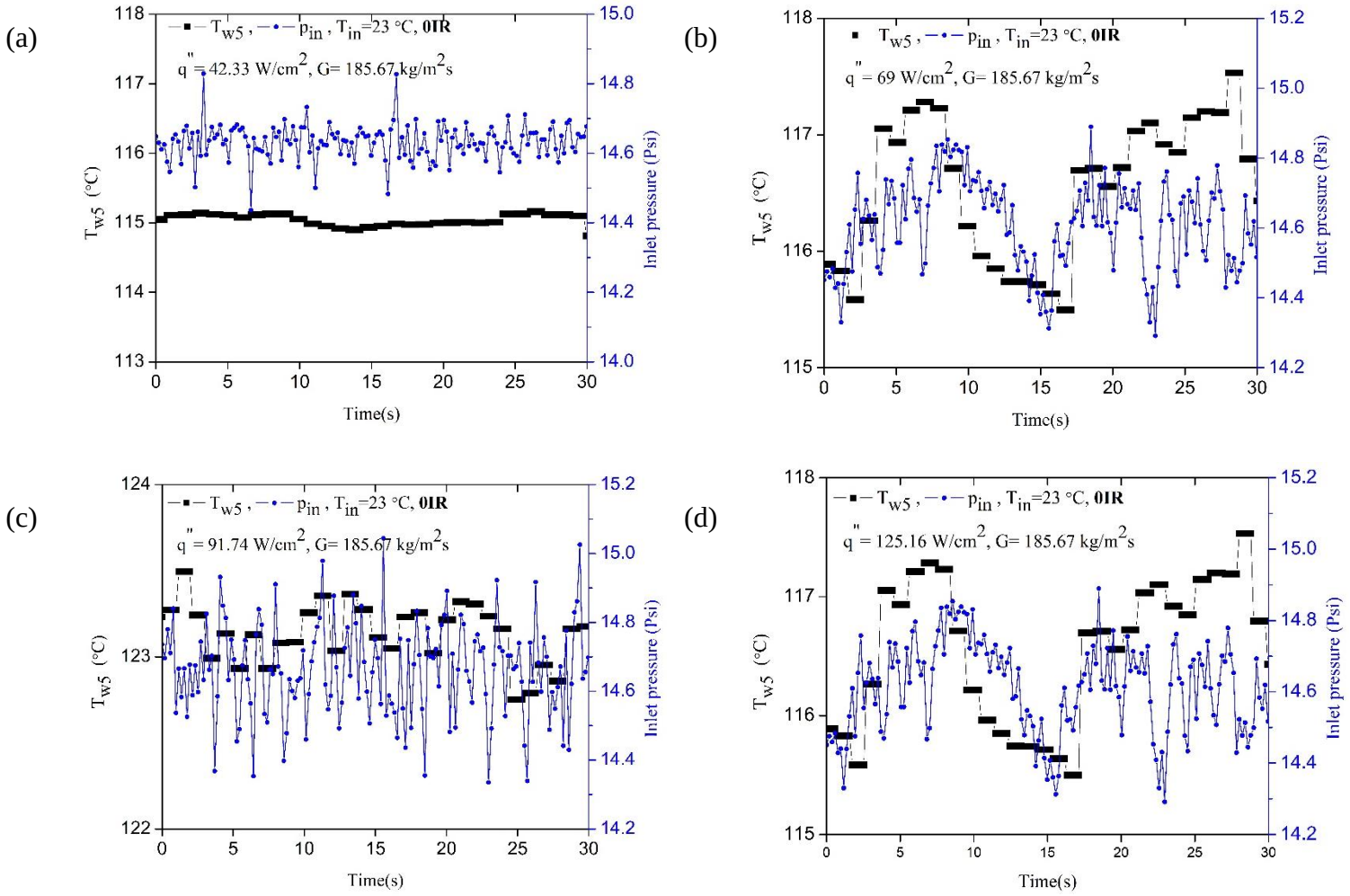

Figure 7.10 Fluctuations of local thermocouple readings (at T5) and inlet pressure for the 0IR design at G = 185.67 kg/m^{2}s and (a) q" = 42.33 W/cm^2 (b) q" = 69 W/cm^2 (c) q" = 91.74 W/cm^2 and (d) q" = 125.16 W/cm^2.

7.5 **Statistical Analysis Coefficient of Variation (CV)**

CV is a statistic representation for the ratio of the standard deviation (σ) to the mean (μ) expressed as a percentage:

$$CV = \frac{\sigma}{\mu} X100\ \% \tag{38}$$

Essentially, it measures the relative dispersion. For example, of two sets of data, each set of data has its value for the mean and the standard deviation, then the value of CV determines which data set is the most dispersed. Figure 7.11 compares the CV values of the pressure oscillations for the 0IR, R-1, R-2, and IR&R-1 cases, at the mass flux of 172.87 kg/m^{2}s and four different heat fluxes, respectively. The respective CV value for each set of the pressure oscillation data is computed using Eq. (38). The results show that the hybrid design (IR&R-1) demonstrates the least variation case than all other three cases, namely, 0IR, R-1, and R-2. Figure 7.12 compares the CV for R-2, R-1, and IR&R-1 at a higher mass flux of G= 186 kg/m^{2}s, and it shows that the IR&R-1 case is more stable for high mass flux than the other two cases (i.e., R-1 and R-2) due to the addition of the IR component at the inlet of the microchannel. Since CV is a measure of reliability, it can be concluded that the lower the CV is, the more reliable system would be.

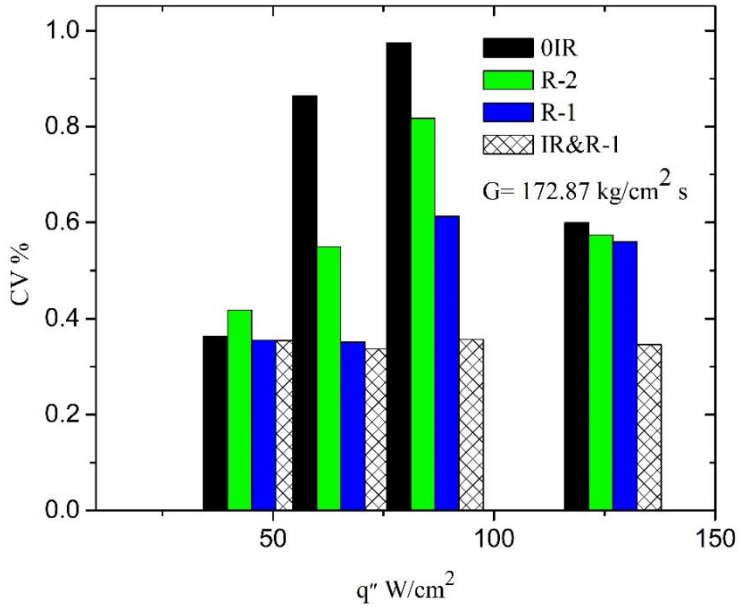

Figure 7.11 Comparing coefficient of variation for 0IR, R-2, R-1, and IR&R-1 at G = 172.87 kg/m^{2}s.

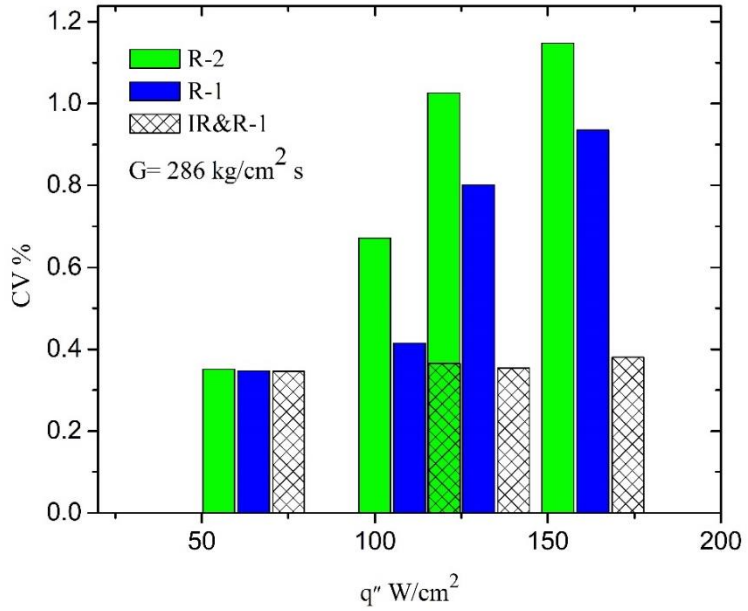

Figure 7.12 Comparing coefficient of variation for R-2, R-1, and IR&R-1 at G = 186 kg/m^{2}s.

7.6 **Summary**

In this study, experimental investigations were performed to quantify the effect of combination IR and roughness surface (IR&R-1) on the heat transfer performance and pressure drop in a flow boiling microchannel heat sink. The main findings are summarized as follows:

(1) For the lowest mass flux, the hybrid design (IR&R-1) improved the CHF performance of the flow boiling microchannel heat sink, compared to both the base case (0IR) and the R-1 case. Specifically, the IR&R-1 case enhanced the CHF by 38.36% over that of 0IR case. The improvement can be mainly attributed to the suppression of flow instabilities by the IR and the knurled roughness surface.

(2) For higher mass flux values at G = 172.78 kg/m^{2}s and G = 286 kg/m^{2}s, IR&R-1 case enhanced the CHF over the corresponding 0IR case. However, it did not show any significant enhancement in CHF, in comparison with the corresponding R-1 case.

(3) The boiling curves for the IR&R-1 and R-1 cases were mostly overlapped in both the single- and two-phase regimes, which indicated that adding an IR to the R-1 case does not enhance the HTC. However, both the IR&R-1 and R-1 cases showed improved HTCs over the base case (0IR), in both the single- and two-phase regimes.

(4) The combination of IR&R-1 with an optimum area opening ratio chosen from section 5.10 always exhibited higher pressure drop penalties.

(5) It was observed that the IR&R-1 sustains a lower inlet pressure variation drop than the 0IR case.

(6) IR&R-1 case had the lowest fluctuation of inlet pressure, e.g., compared with the 0IR case, the amplitude of fluctuations was approximately reduced by 61% to 42% for heat flux between 63 W/cm^2 and 125 W/cm^2.

(7) The standard deviation (σ) of wall temperature fluctuation was reduced approximately by 84% at the low heat flux of 63 W/cm^2, whereas it increased approximately by 68% for the high heat flux of 125 W/cm^2, in comparison with that of the corresponding base case.

(8) Finally, the hybrid design (IR&R-1) demonstrated the least variation of pressure oscillation than that of the 0IR, R-1, and R-2, cases.

CHAPTER 8

CONCLUSIONS AND FUTURE WORK

In advanced power electronics, single-phase and two-phase microchannel heat sinks have shown considerable promise for removing large amounts of heat from small areas. The two-phase microchannel heat sink is considered to be one of the most efficient heat dissipaters since it can handle very high heat flux at a small footprint and needs much less coolant flow rates. However, two-phase microchannels suffer from flow instability issues, which cause significant oscillations in flow rate, temperature, and pressure, as well as deteriorated HTC, and early occurrence of heat flux. Moreover, the ever-increasing high-heat-flux cooling requirements have pushed the single-phase microchannels to their limit. Hence, further enhancement of their HTC is needed.

In this context, this dissertation describes an empirical investigation in to heat transfer enhancement of both the single- and two-phase microchannel heat sinks in relation to the ever-increasing cooling demands for advanced power electronics. In the single-phase regime, to passively enhance the microchannel heat transfer performance, two micro-scale surface modification technologies, namely, knurling and sandblasting, were applied on the bottom surface of the microchannel heat sink, and their effects on the thermohydraulic performance were evaluated. In the two-phase regime too, two techniques to suppress the flow boiling instabilities and to increase the CHF of two-phase flow in microchannels, were investigated. The first technique was the use IRs at the inlet of microchannels to suppress the flow boiling instability and increase the CHF and the second technique was the

modification of the surface roughness of the boiling microchannel also to increase the CHF. Finally, the combined design of the IRs with the knurling surface modification was investigated as a technique to further improve the heat transfer performance in the two-phase microchannels. The research findings and suggestions for future work are as follows.

8.1 Enhancement of the Single-Phase Microchannel Heat Transfer Performance

The two surface modification techniques, knurling and sandblasting, which are conventionally used in macro duct flow, were experimentally investigated for the first time to improve the single-phase microchannel heat transfer performance. It was found that micro-knurled surface modification is a very effective approach in improving single-phase microchannel heat transfer. For the test range, the largest enhancement of HTC achieved was around 255% compared with the smoothed microchannel. However, this thermal improvement was accompanied by a higher pressure drop penalty. The highest pressure drop for the R-1 case was around 360% (and 99% for the R-2 case) compared with the BS case for Reynolds number at 500. For micro-sandblasting, the results showed that the FS bottom surface of the microchannel only slightly improved the heat transfer performance. However, the modified surface with HSEP enhanced the heat transfer performance substantially. Furthermore, the HSEP microchannel heat sink increased the pressure drop by around 10.87% for Re in the range from 85 to 650, whereas the FS microchannel heat sink increased the pressure drop by around 9% for Re between 450 and 650.

8.2 Suppression of Flow Instabilities and Improvment of CHF

For two-phase microchannels, this study experimentally investigated the effects of various configurations of IRs on the thermal/hydraulic performance of flow boiling in a single rectangular microchannel with an aspect ratio of 13.12, and a hydraulic diameter of the 708 μm. The experiments were carried out for the microchannel with three designs of

IRs: one-slot opening (1IR), three-slot openings (3IR), and five-slot openings (5IR), for mass fluxes of 32.68, 81.29, and 144 kg/m^{2}s, respectively. The results show that all test cases with IRs improved the CHF performance of the flow boiling microchannel heat sink, where the 5IR case worked best at low mass flux, and the 3IR case worked best at high mass flux. The results also illustrate that the IRs reduced the HTC at low mass flux but improved the HTC at high mass flux and heat flux. The IRs always exhibited higher pressure drop penalties. Furthermore, all the test cases with IRs improved the flow boiling microchannel heat sink's CHF performance, compared to the base case without IRs. The improvements were mainly attributed to the suppression of the flow instabilities by the IRs. Moreover, for lower mass flow rates at G= 32.68 kg/m^{2}s, cases with multiple-opening IRs (e.g., the 3IR and 5IR cases) generally performed better (e.g., higher CHF) than cases with a single-opening IR (e.g., the 1IR case). Compared to the 0IR case, the 5IR, 3IR, and 1IR cases demonstrated enhanced CHFs at 52.54%, 20.62%, and 13.78%, respectively. This was mainly because multiple-opening IRs reduce the recirculation zones created by the single IR. For higher mass flux at G= 144 kg/m^{2}s, cases with a higher blocking ratio (e.g., 95.41% for 1IR and 86.23% for 3IR) showed higher CHF than those with relatively smaller blocking ratio (e.g., 77.05% for 5IR). Compared to the 0IR case, the 5IR, 3IR, and 1IR cases had enhanced CHFs at 19.22%, 14.53%, and 0.6%, respectively. This was mainly because the higher blocking ratio's contribution becomes dominant in preventing the reverse flow oscillations at high mass flux. The IRs slightly reduced the single-phase microchannel HTC at low flow rates, but the reduction of HTC diminished as the flow rate increased. In addition, IRs generally decreased the two-phase microchannel HTC, and the cases with multiple IRs (e.g., 5IR and 3IR) had relatively higher HTC than that of the 1IR

case. Also, the reduction of HTC diminished as mass flux increased. Importantly, it was revealed that at high mass flux and high heat flux, as shown in Figure 5.15, the IRs improved the HTC of the flow boiling microchannel. IRs with a higher blocking ratio (e.g., 95.41% for 1IR and 86.23% for 3IR) always exhibited higher pressure drop penalties. For instance, compared to the 0IR case at G = 32.68 kg/m^{2}s, the 1IR, 3IR, and 5IR cases increased the pressure drop penalty by 5.79, 2.06, and 1.58 times, respectively. The matrix of gain versus penalty, as shown in Table 5.3, reveals the optimal configuration of IRs at different mass fluxes. The optimal configuration depends on the operational parameters, including the mass flux and heat flux of the microchannel heat sink. The optimal configuration is a compromise between the goals for maximizing the heat transfer performance (e.g., in terms of CHF enhancement) and minimizing the pressure drop penalties. It can be concluded that CHF is a strong function of mass flux (G) and area ratio (AR). Importantly, this study reveals the optimal design criteria for microchannels with IRs, which depends on the operational parameters (e.g., mass flux and heat flux) of the two-phase microchannel heat sink. Furthermore, a parameter study of the area ratio of IRs with openings of 4.2 %, 6.58%, 8.57%, 9.32%, 12.86 %, 15.5 % on the two-phase microchannel heat transfer was also performed. The results demonstrated that the area ratio of 8.57 % is the optimal value for all the ranges of mass fluxes. Finally, the results indicated that to improve the performance of the flow boiling microchannel heat sink, the area ratio can be kept in the range between 8% -10% and it is the optimal design for all ranges of mass fluxes between G = 66 kg/m^{2}s to G = 221.65 kg/m^{2}s. Based on this finding, the optimal area ratio can be proposed in the range between 8% -10%. The reason for the proposed range is the uncertainties stemming from the dimensions of the microchannel surface and the IR. It can

be concluded that CHF is a strong function of both the mass flux and the area ratio of the IR.

The knurled surface technique was also used to study its effects on the thermal performance in flow boiling microchannels. Diamond-shaped knurling was fabricated on the bottom surface of the microchannel, with two different knurling heights. The results show that the knurling did not have a significant influence on the pressure drop, and it did not have a large impact on the CHF under the conditions investigated. It can be concluded that the roughened surfaces for both the R-1 and R-2 cases do not have much influence on the pressure drops, as compared to the base case. Also, the pressure drop was independent of the mass flux and heat flux until the boiling started, and the pressure drop across the microchannel increased slightly with the roughness of R-1 and R-2 at the highest mass flux ($G = 286\ kg/m^2\ s$). Also, both the roughened surfaces (R-1 and R-2) improved the CHF in comparison to that of the smooth surface case. Specifically, around 30% improvement in CHF was achieved for the R-1 case at $G = 172.87\ kg/m^2s$. In addition, both the roughened surfaces (R-1 and R-2) enhanced HTC compared to the base case. A maximum of 81.06 % heat transfer enhancement is achieved for the R-1 case. The fluctuation of wall temperature and inlet pressure was relatively stable for the R-1 case as compared to the R-2 case and the base case. It can be concluded that diamond-shaped knurling (especially the more roughened R-1 case) can effectively enhance flow boiling microchannel heat transfer performance in both the HTC, as well as the CHF.

Moreover, the optimal design of the IRs was achieved when it was combined with knurling to further enhance the heat transfer performance of two-phase microchannels. For the lowest mass flux, the hybrid design (IR&R-1) improved the CHF performance of the

flow boiling microchannel heat sink, compared to both the base case 0IR, and the R-1 case. Specifically, the IR&R-1 case enhanced the CHF by 38.36% over that of the 0IR case. The improvement was mainly attributed to the suppression of flow instabilities by the IR and the knurled roughened surface. For higher mass flux at G = 172.78 kg/m^{2}s and G = 286 kg/m^{2}s, the IR&R-1 case enhanced the CHF over the corresponding 0IR case. However, it does not have any significant enhancement in the CHF, in comparison with the corresponding R-1 case. The boiling curves for the IR&R-1 and R-1 cases are mostly overlapped in both the single- and two-phase regimes, which indicate that adding an IR to the R-1 case does not enhance the HTC. However, both the IR&R-1 and R-1 cases improved the HTCs over the base case (0IR), in both the single- and two-phase regimes. The combination of IR&R-1 with an optimum area opening ratio chosen from Section 5.10 always exhibited higher pressure drop penalties. It was observed that the IR&R-1 sustains a lower inlet pressure variation drop than the 0IR case. It was found that the IR&R-1 case had the lowest fluctuation for inlet pressure, e.g., compared with the 0IR case, the amplitude of fluctuations was approximately reduced by 61% to 42% for heat flux between 63 W/cm^2 and125 W/cm^2. The standard deviation (σ) of wall temperature fluctuation was reduced approximately by 84% at a lower heat flux of 63 W/cm^2, whereas it was increased approximately by 68% for the high heat flux of 125 W/cm^2, in comparison with that of the corresponding base case. The hybrid design (IR&R-1) had the least variation of the pressure oscillation than that of the 0IR, R-1, and R-2, cases.

8.3 **Suggestions for Future Work**

(1) Test enhanced surfaces with different working fluids (such as refrigerant R-123, and R134a) for single-phase and two-phase systems.

(2) Test enhanced surfaces with different heights of knurling for single-phase and two-phase microchannel flow.

(3) Test enhanced surfaces with different inlet temperatures for both single-phase and two-phase microchannel flow.

(4) Experimentally investigate the effects of varying lengths of the IRs on the thermohydraulic performances of flow boiling in rectangular microchannels.

REFERENCES

[1] D. B. Tuckerman and R. F. W. Pease, “High-Performance Heat Sinking for VLSI,” no. 5, pp. 126–129, 1981.

[2] M. B. Bowers and I. Mudawar, “High flux boiling in low flow rate, low pressure drop mini-channel and micro-channel heat sinks,” *Int. J. Heat Mass Transf.*, vol. 37, no. 2, pp. 321–332, 1994.

[3] M. A. Ebadian and C. X. Lin, “A Review of High-Heat-Flux Heat Removal Technologies,” *J. Heat Transfer*, vol. 133, no. 11, p. 110801, 2011.

[4] J. F. Tullius, R. Vajtai, and Y. Bayazitoglu, “A review of cooling in microchannels,” *Heat Transf. Eng.*, vol. 32, no. 7–8, pp. 527–541, 2011.

[5] I. Mudawar, “Two-Phase Micro-Channel Heat Sinks: Theory, Applications and Limitations,” *ASME/JSME 2011 8th Therm. Eng. Jt. Conf.*, vol. 133, no. December, pp. T40001-T40001-37, 2011.

[6] A. P. Roday and M. K. Jensen, “A review of the critical heat flux condition in mini-and microchannels,” *J. Mech. Sci. Technol.*, vol. 23, no. 9, pp. 2529–2547, 2009.

[7] A. R. Vard, P. Moallem, and A. R. N. Nilchi, “Texture-based parametric active contour for target detection and tracking,” *Int. J. Imaging Syst. Technol.*, vol. 19, no. 3, pp. 179–186, 2009.

[8] M. B. Bowers and I. Mudawar, “High flux boiling in low flow rate, low pressure drop mini-channel and micro-channel heat sinks,” *Int. J. Heat Mass Transf.*, vol. 37, no. 2, pp. 321–332, 1994.

[9] I. Mudawar, “Assessment of High-Heat-Flux Thermal,” vol. 24, no. 2, pp. 122–141, 2001.

[10] W. Li, *Enhance Flow Boiling In Microchannels By Regulating Two-Phase Transport Patterns*. 2018.

[11] E. Galvis, “Galvis_Elmer.pdf,” 2012.

[12] G. E. Moore, “Cramming more components onto integrated circuits (Reprint),” *IEEE Solid-State Circuits Newsl.*, vol. 20, no. 3, pp. 33–35, 2006.

[13] A. S. Salman, T. C. Paul, and J. A. Khan, “the Effects of Coverage Area on the Spray Cooling Heat Transfer Performance,” pp. 1345–1353, 2018.

[14] N.M. Abdulrazzaq, Azzam S. Salman, N.Anumbe, Amitav.T, S. K. Oudah, Jamil Khan1 " The effect of chamber pressure on the thermal performance of new refrigerant R513A during spray cooling " HT2019- 3628," p. 3628.

[15] A. Tikadar, S. K. Oudah, T. C. Paul, A. S. Salman, A. K. M. M. Morshed, and J. A. Khan, "Parametric study on thermal and hydraulic characteristics of inter-connected parallel and counter flow mini-channel heat sink," *Appl. Therm. Eng.*, vol. 153, no. January, pp. 15–28, 2019.

[16] N. M. Abdulrazzaq, N. Anumbe, and J. Khan, "Experimental investigation of the performance of refrigerant R134a working in a spray cooling," *Proc. Therm. Fluids Eng. Summer Conf.*, vol. 2018-March, no. March, pp. 1355–1368, 2018.

[17] S. Ndao, Y. Peles, and M. K. Jensen, "Effects of pin fin shape and configuration on the single-phase heat transfer characteristics of jet impingement on micro pin fins," *Int. J. Heat Mass Transf.*, vol. 70, pp. 856–863, 2014.

[18] Z. Shahmoradi, N. Etesami, and M. Nasr Esfahany, "Pool boiling characteristics of nanofluid on flat plate based on heater surface analysis," *Int. Commun. Heat Mass Transf.*, vol. 47, pp. 113–120, 2013.

[19] X. C. Tong, *Advanced Materials for Thermal Management of Electronic Packaging*. New York Heidelberg Dordrecht London: Springer, 2011.

[20] A. Tikadar, S. K. Oudah, N. M. Abdulrazzaq, T. C. Paul, and J. A. Khan, "Experimental study of forced convection heat transfer and flow friction of a water-cooled inter-connected mini-channel heat sink," *ASME Int. Mech. Eng. Congr. Expo. Proc.*, vol. 8, pp. 1–8, 2019.

[21] S. Commons, "Experimental and Numerical Analysis of Enhanced Micro-Channel Cooling Using Micro-Synthetic Jets," 2011.

[22] R. Fang, W. Jiang, and J. A. Khan, "THE EFFECTS OF A CROSS-FLOW SYNTHETIC JET ON SINGLE-PHASE MICROCHANNEL HEAT TRANSFER," vol. 19, no. 4, pp. 343–358, 2012.

[23] R. Fang and J. A. Khan, "Active Heat Transfer Enhancement in Single-Phase Microchannels by Using Synthetic Jets," vol. 5, no. March 2013, pp. 1–8, 2017.

[24] R. Fang and J. A. Khan, "Suppression of Two-Phase Flow Instabilities in Parallel Microchannels by Using Synthetic Jets," vol. 135, no. November 2013, pp. 1–13, 2017.

[25] Z. Wu and B. Sundén, "On further enhancement of single-phase and flow boiling heat transfer in micro/minichannels," *Renew. Sustain. Energy Rev.*, vol. 40, pp. 11–27, 2014.

[26] S. Saha, J. Khan, and T. Farouk, "Numerical study of evaporation assisted hybrid cooling for thermal powerplant application," *Appl. Therm. Eng.*, vol. 166, no. November 2019, p. 114677, 2020.

[27] A. Tikadar *et al.*, “Numerical investigation of heat transfer and pressure drop in nuclear fuel rod with three-dimensional surface roughness,” *Int. J. Heat Mass Transf.*, vol. 126, pp. 493–507, 2018.

[28] M. I. Hasan, A. A. Rageb, M. Yaghoubi, and H. Homayoni, “Influence of channel geometry on the performance of a counter flow microchannel heat exchanger,” *Int. J. Therm. Sci.*, vol. 48, no. 8, pp. 1607–1618, 2009.

[29] A. S. Salman, N. M. Abdulrazzaq, A. Tikadar, S. K. Oudah, and J. A. Khan, “Parametric study of heat transfer characteristics of enhanced surfaces in a spray cooling system: An experimental investigation,” *Appl. Therm. Eng.*, vol. 183, no. August 2020, p. 115824, 2021.

[30] M. Mirzaei and M. Dehghan, “Investigation of flow and heat transfer of nanofluid in microchannel with variable property approach,” pp. 1803–1811, 2013.

[31] A. Tikadar, “Scholar Commons Enhancing Thermal-Hydraulic Performance of Parallel and Counter Flow Mini-Channel Heat Sinks Utilizing Secondary Flow : A Numerical and Experimental Study,” 2019.

[32] A. Tikadar, A. K. M. M. Morshed, S. K. Oudah, T. C. Paul, A. S. Salman, and J. A. Khan, “Effect of inter-connector on thermo-hydraulic characteristics of parallel and counter flow mini-channel heat sink,” *ASME Int. Mech. Eng. Congr. Expo. Proc.*, vol. 8B-2018, pp. 1–9, 2018.

[33] K. Narrein, S. Sivasankaran, and P. Ganesan, “Numerical investigation of two-phase laminar pulsating nanofluid flow in a helical microchannel,” *Numer. Heat Transf. Part A Appl.*, vol. 69, no. 8, pp. 921–930, 2016.

[34] G. Xia, L. Chai, H. Wang, M. Zhou, and Z. Cui, “Optimum thermal design of microchannel heat sink with triangular reentrant cavities,” *Appl. Therm. Eng.*, vol. 31, no. 6–7, pp. 1208–1219, 2011.

[35] N. Azwadi *et al.*, “An overview of passive techniques for heat transfer augmentation in microchannel heat sink,” vol. 88, no. September, pp. 74–83, 2017.

[36] M. Dehghan, M. Daneshipour, M. S. Valipour, R. Rafee, and S. Saedodin, “Enhancing heat transfer in microchannel heat sinks using converging flow passages,” *Energy Convers. Manag.*, vol. 92, pp. 244–250, 2015.

[37] Z. Y. Ghale, M. Haghshenasfard, and M. N. Esfahany, “Investigation of nano fl uids heat transfer in a ribbed microchannel heat sink using single-phase and multiphase CFD models ☆,” *Int. Commun. Heat Mass Transf.*, vol. 68, pp. 122–129, 2015.

[38] H. A. Mohammed, P. Gunnasegaran, and N. H. Shuaib, “Numerical simulation of heat transfer enhancement in wavy microchannel heat sink ☆,” *Int. Commun. Heat Mass Transf.*, vol. 38, no. 1, pp. 63–68, 2011.

[39] S. P. Jang and S. U. S. Choi, “Cooling performance of a microchannel heat sink with nanofluids,” vol. 26, pp. 2457–2463, 2006.

[40] A. K. M. M. Morshed, F. Yang, M. Y. Ali, J. A. Khan, and C. Li, “Enhanced fl ow boiling in a microchannel with integration of nanowires,” *Appl. Therm. Eng.*, vol. 32, pp. 68–75, 2012.

[41] M. Transfer, “Thermohydraulic Charcteristics of A Single-Phase Microchannel Heat sink Coated with Nanowires,” vol. 033003, 2011.

[42] C. R. Dietz and Y. K. Joshi, “Single-Phase Forced Convection in Microchannels with Carbon Nanotubes for Electronics Cooling Applications,” vol. 7265, no. May, 2017.

[43] J. L. Xu, Y. H. Gan, D. C. Zhang, and X. H. Li, “Microscale heat transfer enhancement using thermal boundary layer redeveloping concept,” *Int. J. Heat Mass Transf.*, vol. 48, no. 9, pp. 1662–1674, 2005.

[44] X. J. Wei, Y. K. Joshi, and P. M. Ligrani, “Numerical simulation of laminar flow and heat transfer inside a microchannel with one dimpled surface,” *J. Electron. Packag. Trans. ASME*, vol. 129, no. 1, pp. 63–70, 2007.

[45] A. Tikadar, T. C. Paul, S. K. Oudah, N. M. Abdulrazzaq, A. S. Salman, and J. A. Khan, “Enhancing thermal-hydraulic performance of counter fl ow mini-channel heat sinks utilizing secondary fl ow : Numerical study with experimental validation,” *Int. Commun. Heat Mass Transf.*, vol. 111, p. 104447, 2020.

[46] K. Afb, “Report Loan Copy : Return a Review of Confined Administration,” *Security*, no. July 1971, 2018.

[47] F. Yang, X. Dai, C. J. Kuo, Y. Peles, J. Khan, and C. Li, “Enhanced flow boiling in microchannels by self-sustained high frequency two-phase oscillations,” *Int. J. Heat Mass Transf.*, vol. 58, no. 1–2, pp. 402–412, 2013.

[48] S. G. Kandlikar, “History, Advances, and Challenges in Liquid Flow and Flow Boiling Heat Transfer in Microchannels: A Critical Review,” *J. Heat Transfer*, vol. 134, no. 3, p. 034001, 2012.

[49] A. Mukherjee and S. G. Kandlikar, “The effect of inlet constriction on bubble growth during flow boiling in microchannels,” *International Journal of Heat and Mass Transfer*, vol. 52, no. 21–22. pp. 5204–5212, 2009.

[50] A. Kaya, M. R. Özdemir, M. Keskinöz, and A. Koşar, “The effects of inlet restriction and tube size on boiling instabilities and detection of resulting premature critical heat flux in microtubes using data analysis,” *Appl. Therm. Eng.*, vol. 65, no. 1–2, pp. 575–587, 2014.

[51] C.-J. Kuo and Y. Peles, “Flow Boiling Instabilities in Microchannels and Means for Mitigation by Reentrant Cavities,” *J. Heat Transfer*, vol. 130, no. 7, p. 072402, 2008.

[52] K. Balasubramanian, P. S. Lee, L. W. Jin, S. K. Chou, C. J. Teo, and S. Gao, "Experimental investigations of flow boiling heat transfer and pressure drop in straight and expanding microchannels - A comparative study," *Int. J. Therm. Sci.*, vol. 50, no. 12, pp. 2413–2421, 2011.

[53] M. P. David, J. Miler, J. E. Steinbrenner, Y. Yang, M. Touzelbaev, and K. E. Goodson, "Hydraulic and thermal characteristics of a vapor venting two-phase microchannel heat exchanger," *Int. J. Heat Mass Transf.*, vol. 54, no. 25–26, pp. 5504–5516, 2011.

[54] T. Alam, P. S. Lee, and C. R. Yap, "Effects of surface roughness on flow boiling in silicon microgap heat sinks," *Int. J. Heat Mass Transf.*, vol. 64, pp. 28–41, 2013.

[55] B. J. Jones and S. V. Garimella, "Surface Roughness Effects on Flow Boiling in Microchannels," *ASME 2009 InterPACK Conf. Vol. 2*, vol. 1, no. December 2009, pp. 409–418, 2009.

[56] J. A. Khan, A. M. Morshed, and R. Fang, "Towards Ultra-Compact High Heat Flux Microchannel Heat Sink," *Procedia Eng.*, vol. 90, pp. 11–24, 2014.

[57] R. Fang and J. A. Khan, "Suppression of Two-Phase Flow Instabilities in Parallel Microchannels by Using Synthetic," *J. Therm. Sci. Eng. Appl.*, vol. 5, no. 1, p. 011006, 2013.

[58] Y. K. Prajapati, M. Pathak, and M. Kaleem Khan, "A comparative study of flow boiling heat transfer in three different configurations of microchannels," *Int. J. Heat Mass Transf.*, vol. 85, pp. 711–722, 2015.

[59] S. Zhang, Y. Tang, W. Yuan, J. Zeng, and Y. Xie, "A comparative study of flow boiling performance in the interconnected microchannel net and rectangular microchannels," *Int. J. Heat Mass Transf.*, vol. 98, pp. 814–823, 2016.

[60] A. E. Bergles, J. H. Lienhard, G. E. Kendall, and P. Griffith, "Boiling and evaporation in small diameter channels," *Heat Transf. Eng.*, vol. 24, no. 1, pp. 18–40, 2003.

[61] A. E. Bergles and S. G. Kandlikar, "On the Nature of Critical Heat Flux in Microchannels," *J. Heat Transfer*, vol. 127, no. 1, p. 101, 2005.

[62] A. Koşar, C.-J. Kuo, and Y. Peles, "Suppression of Boiling Flow Oscillations in Parallel Microchannels by Inlet Restrictors," *J. Heat Transfer*, vol. 128, no. 3, p. 251, 2006.

[63] W. Qu and I. Mudawar, "Measurement and prediction of pressure drop in two-phase micro-channel heat sinks," *Int. J. Heat Mass Transf.*, vol. 46, no. 15, pp. 2737–2753, 2003.

[64] C. T. Lu and C. Pan, “Stabilization of flow boiling in microchannel heat sinks with a diverging cross-section design,” *J. Micromechanics Microengineering*, vol. 18, no. 7, 2008.

[65] Y. K. Prajapati and P. Bhandari, “Flow boiling instabilities in microchannels and their promising solutions – A review,” *Exp. Therm. Fluid Sci.*, vol. 88, no. April, pp. 576–593, 2017.

[66] G. Wang, P. Cheng, and A. E. Bergles, “Effects of inlet/outlet configurations on flow boiling instability in parallel microchannels,” *Int. J. Heat Mass Transf.*, vol. 51, no. 9–10, pp. 2267–2281, 2008.

[67] H. L. Wang, H. C. Wu, S. Kong Wang, T. C. Hung, and R. J. Yang, “A study of mini-channel thermal module design for achieving high stability and high capability in electronic cooling,” *Appl. Therm. Eng.*, vol. 51, no. 1–2, pp. 1144–1153, 2013.

[68] Y. Yan and R. B. Thorpe, “Flow regime transitions due to cavitation in the flow through an orifice,” *Int. J. Multiph. Flow*, vol. 16, no. 6, pp. 1023–1045, 1990.

[69] C. Mishra and Y. Peles, “Cavitation in flow through a micro-orifice inside a silicon microchannel,” *Phys. Fluids*, vol. 17, no. 1, 2005.

[70] C. Mishra and Y. Peles, “Size scale effects on cavitating flows through microorifices entrenched in rectangular microchannels,” *J. Microelectromechanical Syst.*, vol. 14, no. 5, pp. 987–999, 2005.

[71] C. Mishra and Y. Peles, “Flow visualization of cavitating flows through a rectangular slot micro-orifice ingrained in a microchannel,” *Phys. Fluids*, vol. 17, no. 11, pp. 1–14, 2005.

[72] S. G. Kandlikar, W. K. Kuan, D. A. Willistein, and J. Borrelli, “Stabilization of Flow Boiling in Microchannels Using Pressure Drop Elements and Fabricated Nucleation Sites,” *Journal of Heat Transfer*, vol. 128, no. 4. p. 389, 2006.

[73] B. Schneider *et al.*, “Cavitation Enhanced Heat Transfer in Microchannels,” *J. Heat Transfer*, vol. 128, no. 12, p. 1293, 2006.

[74] A. Koşar, C.-J. Kuo, and Y. Peles, “Suppression of Boiling Flow Oscillations in Parallel Microchannels by Inlet Restrictors,” *J. Heat Transfer*, vol. 128, no. 3, p. 251, 2006.

[75] C. T. Lu and C. Pan, “Stabilization of flow boiling in microchannel heat sinks with a diverging cross-section design,” *J. Micromechanics Microengineering*, vol. 18, no. 7, 2008.

[76] C. T. Lu and C. Pan, “Convective boiling in a parallel microchannel heat sink with a diverging cross section and artificial nucleation sites,” *Exp. Therm. Fluid Sci.*, vol. 35, no. 5, pp. 810–815, 2011.

[77] X. Dai, F. Yang, R. Fang, T. Yemame, J. A. Khan, and C. Li, “Enhanced single- and two-phase transport phenomena using flow separation in a microgap with copper woven mesh coatings,” *Appl. Therm. Eng.*, vol. 54, no. 1, pp. 281–288, 2013.

[78] Y. Li, G. Xia, Y. Jia, Y. Cheng, and J. Wang, “Experimental investigation of flow boiling performance in microchannels with and without triangular cavities – A comparative study,” *Int. J. Heat Mass Transf.*, vol. 108, pp. 1511–1526, 2017.

[79] F. Yang, X. Dai, C. J. Kuo, Y. Peles, J. Khan, and C. Li, “Enhanced flow boiling in microchannels by self-sustained high frequency two-phase oscillations,” *Int. J. Heat Mass Transf.*, vol. 58, no. 1–2, pp. 402–412, 2013.

[80] A. Koşar, C. J. Kuo, and Y. Peles, “Boiling heat transfer in rectangular microchannels with reentrant cavities,” *Int. J. Heat Mass Transf.*, vol. 48, no. 23–24, pp. 4867–4886, 2005.

[81] A. Mukherjee and S. G. Kandlikar, “The effect of inlet constriction on bubble growth during flow boiling in microchannels,” *Int. J. Heat Mass Transf.*, vol. 52, no. 21–22, pp. 5204–5212, 2009.

[82] S. K. Oudah, R. Fang, A. Tikadar, A. S. Salman, and J. A. Khan, “An experimental investigation of the effect of multiple inlet restrictors on the heat transfer and pressure drop in a flow boiling microchannel heat sink,” *Int. J. Heat Mass Transf.*, vol. 153, p. 119582, 2020.

[83] E. Rahim and A. Bar-Cohen, “Thermal characteristics of a chip-scale two-phase microgap cooler,” *Heat Transf. Eng.*, vol. 36, no. 5, pp. 511–520, 2015.

[84] P. Wang, R. Dawas, M. Alwazzan, W. Chang, J. Khan, and C. Li, “Sweating-boosted air cooling using nanoscale CuO wick structures International Journal of Heat and Mass Transfer Sweating-boosted air cooling using nanoscale CuO wick structures,” *Int. J. Heat Mass Transf.*, vol. 111, no. December 2018, pp. 817–826, 2017.

[85] “J. P. Holman, Experimental methods for engineers, Eighth. New York McGraw Hill, 2012.pdf.” .

[86] M. S. B. Shah, R. K_, “Laminar convective heat transfer in ducts,” *Handb. single-phase Convect. heat Transf.*, vol. 3, p. 1987, 1987.

[87] S. K Oudah, R. Fang, A. Tikadar, K. Egab, Chen Li, J. Khan “The effects of hybrid sandblasting patterns on the heat transfer performance in a single-phase microchannel heat sink,” in *ASME 2017 International Mechanical Engineering Congress and Exposition*, 2017, vol. 8, p. V008T10A024.

[88] R.K. Shah, A.L. London, Advances in Heat Transfer: “Laminar Flow Forced Convection in Ducts, A Source Book for Compact Heat Exchanger Analytical Data. Academic Press, 1978.,’” p. 2014, 2014.

[89] S. K. Oudah, A. Tikadar, R. Fang, K. Egab, and J. A. Khan, “Thermohydraulic Characteristics of a Knurled Microchannel Heat Sink in Single Phase Regime,” pp. 1425–1436, 2018.

[90] W. Qu and A. Siu-Ho, “Experimental study of saturated flow boiling heat transfer in an array of staggered micro-pin-fins,” *Int. J. Heat Mass Transf.*, vol. 52, no. 7–8, pp. 1853–1863, 2009.

[91] D. Deng, Y. Tang, D. Liang, H. He, and S. Yang, “Flow boiling characteristics in porous heat sink with reentrant microchannels,” *Int. J. Heat Mass Transf.*, vol. 70, pp. 463–477, 2014.

[92] W. Qu and I. Mudawar, “Experimental and numerical study of pressure drop and heat transfer in a single-phase micro-channel heat sink,” vol. 45, pp. 2549–2565, 2002.

[93] K. Egab *et al.*, “Enhancing filmwise and dropwise condensation using a hybrid wettability contrast mechanism: Circular patterns,” *Int. J. Heat Mass Transf.*, vol. 154, p. 119640, 2020.

[94] P. Lee and S. V Garimella, “Thermally developing flow and heat transfer in rectangular microchannels of different aspect ratios,” vol. 49, pp. 3060–3067, 2006.

[95] C. J. Kuo and Y. Peles, “Pressure effects on flow boiling instabilities in parallel microchannels,” *Int. J. Heat Mass Transf.*, vol. 52, no. 1–2, pp. 271–280, 2009.

[96] C.-J. Kuo and Y. Peles, “Critical Heat Flux of Water at Subatmospheric Pressures in Microchannels,” *J. Heat Transfer*, vol. 130, no. 7, p. 072403, 2008.

[97] Z. Y. Bao, D. F. Fletcher, and B. S. Haynes, “Flow boiling heat transfer of Freon R11 and HCFC123 in narrow passages,” *Int. J. Heat Mass Transf.*, vol. 43, no. 18, pp. 3347–3358, 2000.

[98] O. S. Al-Yahia and D. Jo, “Onset of Nucleate Boiling for subcooled flow through a one-side heated narrow rectangular channel,” *Ann. Nucl. Energy*, vol. 109, pp. 30–40, 2017.